Summer 8-2014

Fundamental Investigations of Clay/Polymer Nanocomposites and Applications in Co-Extruded Microlayered Systems

Jeremy John Decker
University of Southern Mississippi

The University of Southern Mississippi

FUNDAMENTAL INVESTIGATIONS OF CLAY/POLYMER NANOCOMPOSITES AND APPLICATIONS IN CO-EXTRUDED MICROLAYERED SYSTEMS

by

Jeremy John Decker

Abstract of a Dissertation
Submitted to the Graduate School
of The University of Southern Mississippi
in Partial Fulfillment of the Requirements
for the Degree of Doctor of Philosophy

August 2014

ABSTRACT

FUNDAMENTAL INVESTIGATIONS OF CLAY/POLYMER NANOCOMPOSITES AND APPLICATIONS IN CO-EXTRUDED MICROLAYERED SYSTEMS

by Jeremy John Decker

August 2014

The second and fourth generations of hydroxylated dendritic polyesters (HBP2, HBP4) were combined with unmodified sodium montmorillonite clay (Na^+MMT) in water to generate a broad range of polymer clay nanocomposites from 0 to 100% wt/wt Na^+MMT. X-ray diffraction (XRD) and transmission electron microscopy (TEM) were used to investigate intercalation states of the clay galleries. It was shown that interlayer spacings were independent of generation number and changed over the composition range from 0.5 nm to 3.5 nm in 0.5 nm increments that corresponded to a flattened HBP conformation within the clay tactoids.

The HBP4/Na^+MMT systems were investigated to study the vitrified Rigid Amorphous Fraction (RAF) induced by the clay surfaces. Differential Scanning Calorimetry (DSC) showed changes in heat capacity, ΔC_p, at T_g, that decreased with clay content, until completely suppressed at 80 wt% Na^+MMT due to confinement. RAF was quantified from these changes in heat capacity and verified by the analysis of orthopositronium lifetime temperature scans utilizing positron annihilation lifetime spectroscopy (PALS): verifying the glassy nature of the RAF at elevated temperatures. Mathematical relationships allowed for correlation of the interlayer spacings with ΔC_p.

RAF formation correlated to intercalated HBP4, and external surfaces of the clay tactoids.

The interdiffusion of a polymer pair in microlayers was exploited to increase the concentration of nanoclay particles. When microlayers of a nanocomposite composed of organically modified montmorillonite ($M_2(HT)_2$) inside maleic anhydride grafted linear low-density polyethylene (LLDPE-g-MA) and low-density polyethylene (LDPE) were taken into the melt, the greater mobility of the linear LLDPE-g-MA chains compared to the branched LDPE chains caused shrinkage of the nanocomposite microlayers, concentrating the $M_2(HT)_2$ contained within. Analysis of the clay morphology within these layers demonstrated an increase in clay particle lengths and aspect ratios, which was attributed to the growth of skewed aggregates during concentration. The melt induced clay concentration and increased clay particle dimensions caused significant decreases in the permeability of the nanocomposite microlayers and reduced the overall permeability of the multilayered films. Morphology and transport behavior of these microlayered films were compared to a series of bulk nanocomposites using a second LLDPE-g-MA containing $M_2(HT)_2$ with varying clay content.

The University of Southern Mississippi

FUNDAMENTAL INVESTIGATIONS OF CLAY/POLYMER NANOCOMPOSITES AND APPLICATIONS IN CO-EXTRUDED MICROLAYERED SYSTEMS

by

Jeremy John Decker

A Dissertation
Submitted to the Graduate School
of The University of Southern Mississippi
in Partial Fulfillment of the Requirements
for the Degree of Doctor of Philosophy

Approved:

Dr. Sergei Nazarenko _____
Director

Dr. Robson Storey _____

Dr. Willam Jarrett _____

Dr. Robert Lochhead _____

Dr. Jeffrey Wiggins _____

Dr. Maureen Ryan _____
Dean of the Graduate School

August 2014

ACKNOWLEDGMENTS

I am grateful to my advisor, Dr. Sergei Nazarenko, for the opportunity to work on projects that covered a broad array of techniques and applications. His expertise in structure-property relationships and transport phenomenon were instrumental in the completion of the work detailed herein. I also express gratitude to Dr. Anne Hiltner, who sadly passed away during my graduate career. Her hard work and dedication to fundamental science allowed for many people to work on new and exciting research. Both she and Dr. Eric Baer allowed me to work onsite with their research group many times, providing valuable collaborative experience. Dr. Sergei Chvalun was also instrumental to my research, as he greatly increased my understanding of X-ray diffraction techniques and interpretation. Dr. Kenneth Curry was probably the best instructor in instrumental techniques I have ever had, and without his patience and guidance, I would never have achieved the level of expertise I now possess with transmission electron microscopy. I would like to thank the graduate students at Case Western Reserve University who worked with me to facilitate my CLiPS research. In particular, these names bear mention: Michael Ponting, Chuanyar Lai, and Shannon Armstrong. I would also like to express gratitude for instrumental and equipment support, as well as technical assistance to Dr. James Rawlins, Dr. Jeffrey Wiggins, Dr. Robert Moore, and their respective staff and graduate students over the course of my research. Without their assistance, many things would have been impossible. The same applies to my committee members, Dr. Robson Storey, Dr. Robert Lochhead, and Dr. William Jarrett, who each provided critical support during my graduate career.

Primary financial support of this research was from to the Materials Research Science and Engineering Center (MRSEC), DMR 0213883 and the Center for Layered Polymeric Systems Center (CLiPS), DMR 0423914.

TABLE OF CONTENTS

LIST OF TABLES

Table

LIST OF SCHEMES

Scheme

LIST OF ILLUSTRATIONS

Figure

CHAPTER I

RESEARCH BACKGROUND

Nanocomposites Overview

In recent years polymer/layered silicate nanocomposites (PLSN) have attracted great interest because they can possess superior properties as compared to virgin polymers or conventional composite materials. Improvements include, but are not limited to, physical, thermal, gas barrier, and flammability properties [1-3]. Thus, these systems are of considerable interest both from a fundamental perspective and in terms of practical applications [1-17]. The introduction of multiple substrates into a polymer matrix creates unique model systems for investigating the structure and dynamics of polymers under confinement [18-22].

The intercalation of polymers with modified layered silicates was observed many years ago [24,25]. However, PLSN have gained considerable attention in recent years because of two primary findings. First, the Toyota research group demonstrated that with very small amounts of layered silicate, improvement of the thermal and mechanical properties of Nylon-6 could be obtained [26]. In addition, Vaia et al. demonstrated that nanocomposites could be generated by the direct melt-mixing of polymers with layered clays [27]. The potential to melt mix nanocomposites increased their industrial viability because continuous melt extrusion methods have long been employed in polymer processing. Due to the marked property improvements obtained with only small amounts of relatively low cost additives, the practical interest in nanocomposites increased.

Layered silicate clays are often used in nanocomposite materials. Typical layered silicates used in PLSN belong to the same general family of 2:1 layered or

phyllosilicates. Their crystal structure consists of layers made up of two tetrahedrally coordinated silicon atoms fused to an octahedral sheet of aluminum or magnesium hydroxide. Isomorphic substitution within the layers (for example, Al^{3+} replaced by Mg^{2+}) generates negative in the octahedral layers that generates a negative total charge for the clay layer itself. The average silicate surface charge is designated as the cation exchange capacity (CEC) and is typically expressed as milliequivalents/100 gram. These layer charges are counterbalanced by alkali and alkaline earth cations situated inside the galleries, which consist of stacks of the ~1nm thick clay layers with lateral dimensions that can vary from 30 nm to many microns. The ultimate size of the clay layers is dependent upon the individual layered silicate and where it is mined or synthesized. Examples of typical layered silicates employed in nanocomposites are montmorillonite (MMT), saponite, and hectorite.

Layered silicates most typically employed in nanocomposites may potentially disperse into individual layers and have surface chemistries that can be modified through ion exchange reactions with organic or inorganic cations. These charge properties of the silicate layers and the alkali counterions are both intimately related to the processing and final properties of nanocomposites since dispersal of the layers increases the available clay surface area and is dependent upon the interactions of the silicate with the surrounding polymer matrix. Favorable interactions between the silicate surfaces and the polymer can lead to nanoscale dispersion of the clay layers. Good dispersion combined with the extremely thin dimension of the silicate layers leads to exceptionally high surface areas at relatively low clay loadings. The large interfacial areas between the clay layers and the polymer matrix cause nanocomposites to exhibit unique properties not

exhibited by conventional composites incorporating macroscale fillers [28]. Unmodified layered silicates possessing Na^+ or K^+ ions are readily hydrated by water due to their inherent hydrophilicity. However, these layered silicates are only naturally miscible with hydrophilic polymers, such as poly(ethylene oxide) (PEO) or poly(vinyl alcohol) (PVA) [29,30]. To increase compatibility with hydrophobic polymers, the surfaces must be modified so that they are more organophilic. This is generally accomplished by exchanging the sodium or potassium ions with quaternary alkylammonium or alkylphosphonium cationic surfactants. These reduce the surface energy of the clay sheets, and increase compatibility with the polymer matrix. Incorporation of the polymer between the clay sheets results in increased interlayer spacings. Surface modification of the clay layers can also be employed to create functional groups that can react with, or initiate the polymerization of polymers [31,32].

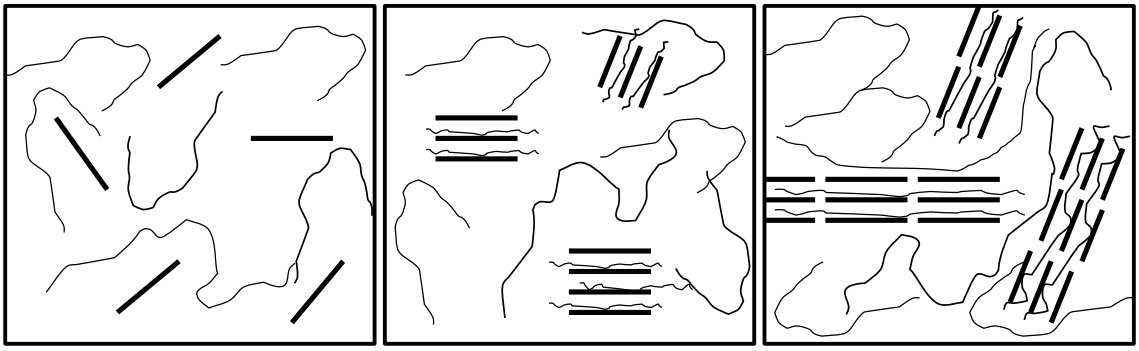

Figure 1. Basic 2:1 phyllosilicate nanocomposite morphologies.

Favorable interfacial interactions between the polymer matrix and layered silicates lead to three primary types of PLSN as illustrated in Figure 1. Intercalated nanocomposites occur due to the insertion of polymer into the regularly ordered silicate layers. These ordered intercalated structures possess crystallographic dimensions. These

intercalated clay stacks can also flocculate, due to hydroxylated edge-to-edge interactions between intercalated clay stacks. Exfoliated nanocomposites occur when the individual clay layers are separated in the polymer matrix and are possessed of no long range order. Typically, exfoliated nanocomposites occur at much lower clay loadings than intercalated nanocomposites. A commonly observed, but less typically mentioned morphology is a type of intercalation, where the clay layers are not stacked in a parallel fashion, and this is referred to as a disordered-intercalated state. In addition, the clay and polymer interactions may be so poor that complete phase separation occurs, resulting in a distribution of unintercalated clay stacks within the polymer matrix.

A wide variety of techniques have been employed for the characterization of polymer/layered silicate nanocomposites. Typical morphological techniques include wide angle X-ray diffraction (WAXD), transmission electronic microscopy (TEM), atomic force microscopy (AFM), and small-angle X-ray scattering (SAXS). Among them, X-ray (XRD) diffraction techniques and TEM prove most effective for determining the morphology of the clays in terms of interlayer spacings and clay ordering. X-ray powder diffraction in reflection geometry is used to characterize the structure of PLSN, as it provides a bulk representation of clay ordering without the influence of structural orientation. The position and intensity of the (00l) basal reflections are used to characterize the interlayer spacings of intercalated nanocomposites. However, factors such as layer disorder and low clay volume fractions will contribute to a broadening and weakening of the basal reflections seen by XRD, which serves to complicate analysis in the low clay content regimes [33]. For this reason, transmission electron microscopy (TEM) is frequently used to accompany XRD data, as it gives a direct picture of the

nanocomposite morphology at high magnification. However, unlike XRD, TEM is not a bulk technique, and great care must be taken to represent the bulk morphology as accurately as possible. This generally entails the use of multiple images, at various degrees of magnification, and some type of statistical analysis of the observed morphology. In general, TEM reveals that nanocomposites possess a mixture of morphologies or morphologies that are in an intermediate state, such as the disordered-intercalated clay morphology.

Preparative methods for nanocomposites are divided into three main groups according to starting materials and processing techniques. Intercalation of a polymer from solution can be accomplished when the polymer is soluble in solvent and the silicate layers can be swelled or delaminated in the same solvent. Upon mixing of the polymer and clay dispersions, the polymer chains may intercalate between the clay layers, displacing adsorbed solvent and upon solvent evaporation, generate nanocomposite structures. The intercalation of the polymer into the layered silicate galleries by solution methodology is generally considered to be entropically driven by desorption of the solvent molecules, which compensates for the reduced entropy caused by the confinement of the polymer chains [34]. In situ intercalative polymerizations are similar in that the layered silicates are swollen by the liquid monomer or a solution thereof, which allows for monomer intercalation and polymerization within the clay galleries. Lastly, and most valuable from a commercial perspective, is melt intercalation. This involves the direct annealing of the polymer and layered silicate above the melting temperature of the polymer and frequently involves applied shear. A major advantage of this type of processing is that it avoids the use of solvents, the removal of which can be a

time consuming and, therefore, expensive process. Melt intercalation is considered to be primarily driven by energetic factors since the entropic gains of clay separation are largely offset by the confinement of the polymer chains. [7,35]

Gas Permeation in Polymer Nanocomposites

The high surface areas of the silicate layers can have a very pronounced impact on the gas barrier properties of nanocomposite systems, relative to the virgin polymer. Oxygen is the most widely investigated permeant gas in polymeric materials [36,37]. It is generally considered an undesirable contaminant since it oxidizes materials over time, which is detrimental to foodstuff and other degradable materials. The permeability, *P*, is a measure of the steady-state flux and is dependant upon two factors: the diffusivity (*D*) and solubility (*S*) as given from the relationship $P = DS$. The diffusivity, *D*, is a kinetic term related to the transport of gas molecules across a membrane. The solubility, *S*, is a thermodynamic term, dependent upon the interactions between the penetrant molecule and the polymer matrix.

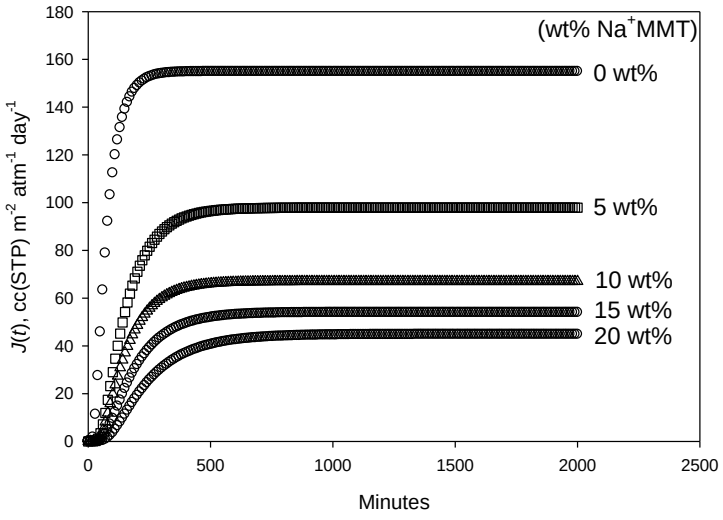

Figure 2. Experimental $J(t)$ data for nanocomposites containing sodium montmorillonite clay (Na^+MMT).

To obtain *P*, *D*, and *S*, one measures the oxygen flux $J(t)$ under controlled temperature and humidity conditions. The flux is treated according to the formula to obtain the permeability

$$J = \frac{P\Delta p}{l} \tag{1}$$

where J is the flux, l the film thickness, Δp the pressure driving force, and P the permeability. A common device to measure permeability of polymeric films is a MOCON. This is a commercially available instrument that measures oxygen flux across a film based upon partial pressure driving forces. Nitrogen gas is first used to purge all residual oxygen from sample films. Oxygen is then introduced on the test side of the film. Both sides of the tested film are kept at 1 atm pressure. The partial pressure driving force of the 1 atm oxygen induces the diffusion of oxygen across the film. A sensor on the testing side quantifies the permeant oxygen gas. Experimental flux data generated by this method is shown in Figure 2. The steady-state flux corresponds to the plateau regions shown in Figure 2 and allows for the determination of *P* as previously detailed. To determine *D* the flux curve is fit to the solution of Fick's second law:

$$\frac{dc}{dt} = D\frac{d^2c}{dx^2} \tag{2}$$

where the boundary conditions are that $c(x = 0,t) = Sp$ and $c(x = l,t) = 0$, with initial condition $c(x, t = 0) = 0$. This yields

$$J(t) = \frac{Pp}{l}\left[- \sum_{n=1}^{\infty} (-1)^n \exp(- D\pi^2 n^2 t / l^2)\right] \tag{3}$$

A least square, two-parameter fit is performed according to Equation 3 to determine *D*.

Solubility can then be determined from $P = DS$. It is critical to properly degass the sample for this determination. It is also critical that film thicknesses be accurately determined, as this is a common source of error in gas permeability measurements.

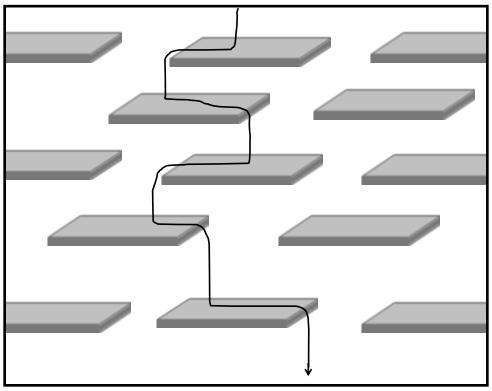

Figure 3. Barrier to permeation imposed by high aspect ratio filler particles in polymer matrix.

Nanocomposites, especially well dispersed polymer layered silicate nanocomposites, introduce high aspect ratio particles into the polymer matrix. In the case of clays, which the entirety of this dissertation focuses upon, well dispersed clay layers means that a large surface area of gas impermeable filler is introduced into the polymer matrix. This creates an impediment to gas diffusion through the membrane by altering the diffusion path of the penetrant molecules, as illustrated in Figure 3. A number of gas diffusion models have been proposed, and a significant number are listed in Table 1. These diffusion models are derived based upon parallel platelets aligned parallel to the surface of the film. When high aspect ratios are achieved with nanoclays dispersed in the polymer matrix, theory predicts significant decreases in permeability, and this is also seen in practice. Among the changes in materials properties often targeted with PLSN

materials, gas barrier rates very highly, as large improvements can potentially be generated with very small quantities of filler material.

Table 1

Models for Predicting Barrier Properties of Platelet Filled Nanocomposites

Model	Filler Type	Formula*	Reference
Nielsen	Ribbon[a]	$(P_0/P)(1-\varphi) = (1+\alpha\varphi)$	[38]
Cussler (*regular array*)	Ribbon[a]	$(P_0/P) = 1+ (\alpha^2\varphi^2)/(1-\varphi)$	[39]
Cussler (*random array*)	Ribbon[a]	$(P_0/P)(1-\varphi) = (1+2\alpha\varphi/3)^2$	[39]
Gusev and Lusti	Disk[b]	$(P_0/P)(1-\varphi) = \exp[(2\alpha\varphi/3.47)^{0.71}]$	[40]
Cussler (polydisperse flakes) (*discrete distribution*)	Ribbon[a]	$(P_0/P)(1-\varphi) = [1+(2\varphi\Sigma_i n_i R_i^2)/(3a\Sigma_i n_i R_i)]^2$ n_i = number of flakes of size category i R_i = ½ particle width a = particle thickness	[39]
Cussler (polydisperse flakes) (*continuous distribution*)	Ribbon[a]	$(P_0/P)(1-\varphi) = [1+2\varphi(R^2+\sigma^2)/(3aR)]^2$ where R = number average ½ particle width σ = standard deviation of ½ particle width a = particle thickness	[39]

[a] For ribbons, length is infinite, ½ particle width is (R), thickness is (a), aspect ratio is $\alpha = R/a$.

[b] For disks, ½ diameter r and thickness t, aspect ratio is $\alpha = r/t$.

[*] φ is volume fraction of filler, P is permeability of composite, P_0 is permeability of pure polymer.

Rigid Amorphous Fraction in Polymers

The concept of the rigid amorphous fraction (RAF) was introduced to explain the vivid deviation from one-to-one correspondence between crystallinity and the observed change in heat capacity, ΔC_p , in the glass transition, T_g, interval for semicrystalline polymers [41]. In the simplest terms, the RAF represents the fraction of amorphous phase that does not contribute to the change in heat capacity. It is believed that this phase is due to immobilization of the polymer chains by interfaces and has been investigated in semicrystalline polymers for many years, where the interfaces form due to polymerization crystallization [41-45].

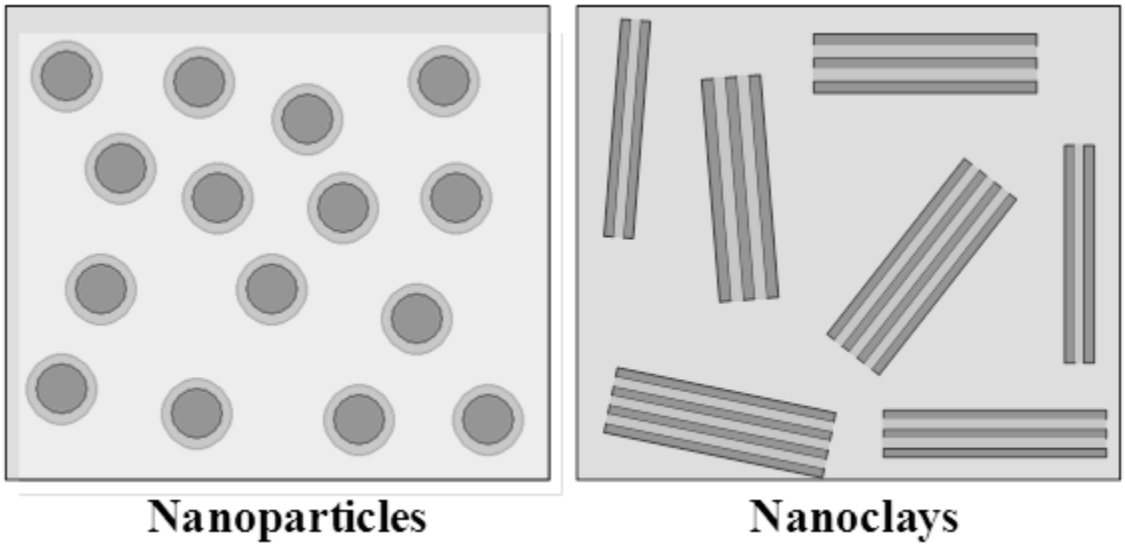

Figure 4. Rigid Amorphous Fraction (RAF) surrounding nanoparticles and nanoclays in a polymer matrix.

More recently, there have been investigations into the formation of the rigid amorphous phase in nanocomposite systems where it has been demonstrated that inorganic fillers can also contribute to the immobilization of the amorphous polymer. [45-48]. In these papers the rigid amorphous fraction was attributed to the interfacial

interactions of the inorganic fillers with the polymer matrices. Currently, there is no evidence that the rigid amorphous fraction undergoes devitrification in these systems since the inorganic particles utilized do not melt within the thermal stability range of the polymers. This means that the interactions between the polymer and inorganic substrate are maintained at elevated temperatures and prevent the devitrification of the immobilized fraction [45]. Indeed this was recently demonstrated in a nanocomposites study of the dynamics of an amorphous hyperbranched polyesteramide intercalated in Na^{+}MMT layers, which was investigated by quasi elastic-neutron scattering. In this study, it was observed that the polymer chains confined within the clay galleries exhibited behavior similar to that of the bulk polymer below the glass transition temperature, but above this T_g, the HBP dynamics were frozen due to the clay nanoconfinement, which was supported by observed decreases in ΔC_p at T_g with clay content [49].

Positron Annhiliation Lifetime Spectroscopy of Polymers

Positron annihilation lifetime spectroscopy (PALS) is a useful technique used to probe structural disorder in polymers [51]. In particular, quantitative comparisons have been established between the characteristic parameters, of intensity, I_3, and lifetime ,τ_3, of the orthopositronium (o-Ps) annihilation component of PALS and the fractional free volume f_v of amorphous polymers, as computed by statistical mechanical theory [51,52]. The o-Ps formation probability, I_3, and is a measure of the density of free volume holes. The o-Ps lifetime, τ_3, can be related to the hole radius R and hence to the hole volume $v_f = (4\pi/3)R^3$. Thus, $f_v = CI_3v_f$, where C is a constant which must be established for each polymer. Approaches also exist to correlate the o-Ps lifetimes with fractional free volume

without the use of I_3 data. [53-56]. Analysis of the free volume properties of polymers can give significant insight into the interactions of nanoparticles with the surrounding polymer matrix.

Multilayered Polymeric Films by Co-extrusion

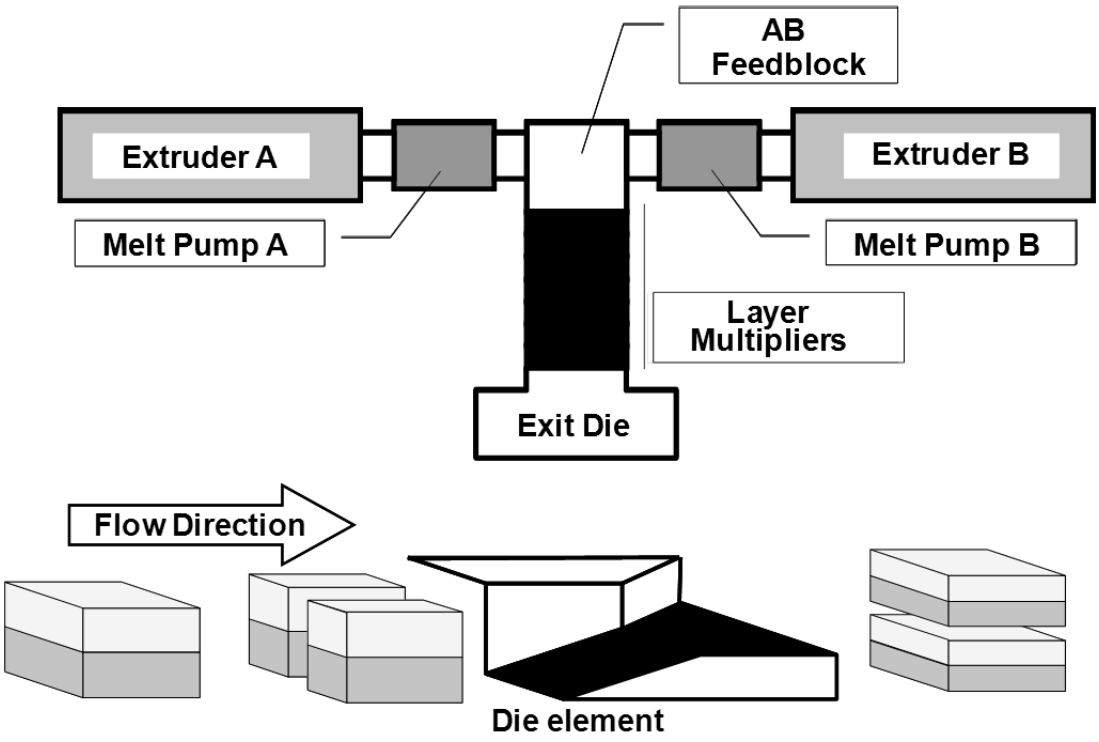

Figure 5. Simplified overview of multilayer coextrusion system. The die element causes the layer multiplication.

Multilayered polymeric films can be created by a continuous layer-multiplying coextrusion processes where two or more dissimilar polymers are combined in microlayered or nanolayered laminates with dozens to thousands of alternating layers with controlled thicknesses [57]. Multilayered polymeric films generated in this manner have demonstrated improvements in toughness and impact resistance when the individual layers are sufficiently thin [58]. Microlayering is an attractive approach for creating designed architectures from particulate filled polymers. If the particles are anisotropic, for

example, platelets, flakes, tubes, or short fibers, the geometric constraints imposed by layer multiplying ensure orientation of the particles in the plane of the layers [59]. The stringent flow conditions required for microlayer coextrusion provide an opportunity to combine miscible polymers on a small scale with negligible mixing [61,62]. Heating the multilayered films composed of miscible polymers into the melt state can activate interdiffusion, which causes the system to gradually convert into a periodic gradient blend with compositional maxima and minima located at the centers of the initial layers. Although the diffusion coefficients of polymer chains are very low, the scale of the microlayers ensures compositional changes on relatively minor time scales of minutes or hours.

References

[1] Alexandre M, Dubois P. Polymer-layered silicate nanocomposites: preparation, properties, and uses of a new class of materials. Mater Sci Eng, 2000; 28: 1-63.

[2] Ray SS, Okamoto M. Polymer/layered silicate nanocomposites: a review from preparation to processing Prog. Polym. Sci. 2003; 28: 1539-1641.

[3] Tjong SC. Structural and mechanical properties of polymer nanocomposites Mater. Sci. Eng., R. 2006; 53: 73-197.

[4] Dabrowski F, Bourbigot S, Delbel R, Bras ML. Kinetic molding of the thermal degradation of polyamide-6 nanocomposite. Eur Polym J 2000; 36: 273–84.

[5] Vaia RA, Jandt KD, Kramer EJ, Giannelis EP. Kinetics of polymer melts intercalation. Macromolecules 1995; 28: 8080–5.

[6] Vaia RA, Giannelis EP. Lattice of polymer melt intercalation in organically-modified layered silicates. Macromolecules 1997; 30: 7990–9.

[7] Vaia RA, Giannelis EP. Polymer melts intercalation in organically-modified layered silicates: model predictions and experiment. Macromolecules 1997; 30: 8000–9.

[8] Lee JY, Baljon ARC, Loring RF, Panagiopoulos AZ. Simulation of polymer melt intercalation in layered nanocomposites. J Chem Phys 1998; 109: 10321–30.

[9] Balazs AC, Singh C, Zhulina E. Modeling the interactions between the polymers and clay surfaces through self-consistent field theory. Macromolecules 1998; 31: 8370–81.

[10] Balazs AC, Singh C, Zhulina E, Lyatskaya Y. Modeling the phase behavior of polymer–clay composites. Acc Chem Res 1999; 32: 651–7.

[11] Fredrickson GH, Bicerano J. Barrier properties of oriented disk composites. J Chem Phys 1999; 110: 2181–8.

[12] Ginzburg VV, Balazs AC. Calculating phase diagram of polymer-platelet mixtures using density functional theory: implication for polymer/clay composites. Macromolecules 1999; 32: 5681–8.

[13] Baljon ARC, Lee JY, Loring RF. Molecular view of polymer flows into a strongly attractive slit. J Chem Phys 2000; 111: 9068–72.

[14] Ginsburg VV, Singh C, Balazs AC. Theoretical phase diagram of polymer/clay composites: the role of grafted organic modifier. Macromolecules 2000; 33: 1089–99.

[15] Kuznetsov D, Balazs AC. Scaling theory for end-functionalized polymers confined between two surfaces: predictions for fabricating polymer nanocomposites. J Chem Phys 2000; 112: 4365–75.

[16] Singh C, Balazs AC. Effect of polymer architecture on the miscibility of polymer/clay mixtures. Polym Int 2000; 49: 469–71.

[17] Ginsburg VV, Balazs AC. Calculating phase diagrams for nanocomposites: the effect of adding end-functionalized chains to polymer/clay mixture. Adv Mater 2000; 12: 1805–9.

[18] Manias E, Kuppa V. Molecular simulations of ultra-confined polymers. Polystyrene intercalated in layered-silicates. In: Vaia RA, Krishnamoorti R, editors. Polymer nanocomposites. ACS symposium series, vol. 804, Oxford: Oxford University Press; 2002. p. 193–207.

[19] Manias E, Kuppa V. Relaxation of polymers in 2-nm slitpores: confinement induced segmental dynamics and suppression of the glass transition. Colloids Surf., A 2001; 187–188: 509–21.

[20] Hackett E, Manias E, Giannelis EP. Molecular dynamics simulations of organically modified layered silicates. J Chem Phys 1998; 108: 7410–5.

[21] Hackett E, Manias E, Giannelis EP. Computer simulation studies of PEO/layered silicate nanocomposites. Chem Mater 2000; 12: 2161–7.

[22] Anastasiadis SH, Karatasos K, Vlachos G, Manias E, Giannelis EP. Nanoscopic confinement effects on local dynamics. Phys Rev Lett 2000; 84: 915–8.

[23] Zax DB, Yang DK, Santos RA, Hegmann H, Giannelis EP, Manias E. Dynamical heterogeneity in nanoconfined poly(styrene) chains. J Chem Phys 2000; 112: 2945–51.

[24] Blumstein A. Polymerization of adsorbed monolayers: II. Thermal degradation of the inserted polymers. J Polym Sci A 1965; 3: 2665–73.

[25] Theng BKG. Formation and properties of clay–polymer complexes. Amsterdam: Elsevier; 1979.

[26] Okada A, Kawasumi M, Usuki A, Kojima Y, Kurauchi T, Kamigaito O. Synthesis and properties of nylon-6/clay hybrids. Schaefer DW, Mark JE, editors. Polymer based molecular composites. MRS Symposium Proceedings, Pittsburgh, vol. 171; 1990. p. 45–50.

[27] Vaia RA, Ishii H, Giannelis EP. Synthesis and properties of two-dimensional nanostructures by direct intercalation of polymer melts in layered silicates. Chem Mater 1993; 5: 1694–6.

[28] Fisher H. Polymer nanocomposites: from fundamental research to specific applications. Mat Sci Eng C 2003; 23: 763-772

[29] Aranda P, Ruiz-Hitzky E. Poly(ethylene oxide)-silicate intercalation materials. Chem Mater 1992; 4: 1395–403.

[30] Greenland DJ. Adsorption of poly(vinyl alcohols) by montmorillonite. J Colloid Sci 1963; 18: 647–64.

[31] Krishnamoorti R, Vaia RA, Giannelis EP. Structure and dynamics of polymer-layered silicate nanocomposites. Chem Mater 1996; 8: 1728–34.

[32] Blumstein A. Polymerization of adsorbed monolayers: II. Thermal degradation of the inserted polymers. J Polym Sci A 1965; 3: 2665–73

[33] Vaia RA, Liu W. X-Ray Powder diffraction of polymer/layered silicate nanocomposites: model and practice. J Polym Sci B 2002; 40: 1590-1600

[34] Vaia RA, Giannelis EP. Lattice of polymer melt intercalation in organically-modified layered silicates. Macromolecules 1997; 30: 7990–9.

[35] Lee JY, Baljon ARC, Loring RF, Panagiopoulos AZ. Simulation of polymer melt intercalation in layered nanocomposites. J Chem Phys 1998; 109: 10321–30

[36] Lang J, Wyser Y. Recent innovations in barrier technologies for plastic packaging—a review. Packaging Technology and Science 2003; 16: 149.

[37] Lagaron JM, Catala R, Gavara R. Structural characteristics defining high barrier properties in polymeric materials. Mater Sci Technol 2004; 20: 1-7.

[38] Nielsen LE. J Models for the Permeability of Filled Polymer Systems. Macromol Sci (Chem) 1967; A1: 929–42.

[39] Lape NK, Nuxoll EE, Cussler EL. Polydisperse flakes in barrier films. J Membr Sci 2004; 236: 29–37.

[40] Gusev AA, Lusti HR. Rational design of nanocomposites for barrier applications. Adv Mater 2001; 13(21): 1641.

[41] Wunderlich B. Reversible crystallization and the rigid–amorphous phase in semicrystalline macromolecules Prog Polym Sci 2003; 28: 383

[42] Wunderlich B. Calorimetry of nanophases of macromolecules Int. J. Thermophys. 2007; 28: 958-967.

[43] Lin J, Shenogin S, Nazarenko S. Oxygen solubility and specific volume of rigid amorphous fraction in semicrystalline poly(ethylene terephthalate). Polymer 2002; 43: 4733.

[44] Olson BG, Lin J, Nazarenko S, Jamieson AM. Positron annihilation lifetime spectroscopy of poly(ethylene terephthalate): contributions from rigid and mobile amorphous fractions. Macromolecules 2003; 36: 7618.

[45] Sargsyan A, Tonoyan A, Davtyan S, Schick C. The amount of immobilized polymer in PMMA SiO_2 nanocomposites determined from calorimetric data. Eur Polym J 2007; 43: 3113.

[46] Corcione EC, Maffezzoli A. Glass transition in thermosetting clay-nanocomposite polyurethanes Thermochim Acta 2009; 485: 43-48.

[47] Wurm A, Ismail M, Kretzschmar B, Pospiech D, Schick C. Retarded crystallization in polyamide/layered silicates nanocomposites caused by an immobilized interphase. Macromolecules 2010; 43: 1480.

[48] Fotiadou S, Chrissopoulou K, Frick B, Anastasiadis SH. Structure and dynamics of polymer chains in hydrophilic nanocomposites. J Polym Sci Part B Polym Phys 2010; 48: 1658.

[49] Fotiadou S, Karageorgaki C, Chrissopoulou K, Karatasos K, Tanis I, Tragoudaras D, Frick B, Anastasiadis SH. Structure and dynamics of hyperbranched polymer/layered silicate nanocomposites. Macromolecules 2013; 46: 2842

[50] Pethrick RA. Positron annihilation: A probe for nanoscale voids and free volume? Prog Polym Sci 1997; 22: 1.

[51] Higuchi H, Yu Z, Jamieson AM, Simha R, McGervey JD. Thermal history and temperature dependence of viscoelastic properties of polymer glasses: relation to free volume quantities. J Polym Sci Polym Phys 1995, 33(17): 2295.

[52] Simha R, Somcynsky T. On the statistical thermodynamics of spherical and chain molecule fluids. Macromolecules 1969; 2: 342.

[53] Dlubek G, Stejny J, Alam MA. Effect of Cross-Linking on the Free-Volume Properties of Diethylene Glycol Bis(allyl carbonate) Polymer Networks: A Positron Annihilation Lifetime Study Macromolecules 1998; 31: 4574.

[54] Srithawatpong R, Peng ZL, Olson BG, Jamieson AM, Simha R, McGervey JD, Maier TR, Halasa AF, Ishida H. Positron annihilation lifetime studies of changes in free volume on cross-linking cis-polyisoprene, high-vinyl polybutadiene, and their miscible blends. J Polym Sci Polym Phys 1999; 37: 2754.

[55] Schmidt M, Maurer FHJ. Relation between free-volume quantities from PVT–EOS analysis and PALS. Polymer 2000; 41: 8419.

[56] Dlubek G, Bamford D, Rodriguez-Gonzalez A, Bornemann S, Stejny J, Schade B, Alam MA, Arnold M. Free volume, glass transition, and degree of branching in metallocene-based propylene/α-olefin copolymers: Positron lifetime, density, and differential scanning calorimetric studies. J Polym Sci Polym Phys 2002; 40: 434.

[57] Im J, Baer E, Hiltner A. High performance polymers; Eds. Baer, E., Moet, A. Hanser: Munich, 1991; p 175-198.

[58] Ma M, Vijayan K, Im J, Hilner A, Baer E. Thickness effects in microlayer composites of polycarbonate and poly(styrene-acrylonitrile). J Mater Sci 1990; 25; 2039.

[59] Nazarenko S, Dennison M, Shuman T, Stepanov V, Hiltner A, Baer E. Creating layers of concentrated inorganic particles by interdiffusion of polyethylenes in microlayers. J App Polym Sci 1999; 73: 2877.

[60] Pollock G, Nazarenko S, Hiltner A, Baer E. Interphase materials by forced assembly of glassy polymers. J Appl Polym Sci 1994; 52: 163.

[61] Haderski D, Nazarenko S, Hiltner A, Baer E. Interdiffusion of linear and branched polyethylene in microlayers studied via melting behavior. Macromol Chem Phys 1995; 196: 2545.

CHAPTER II

RESEARCH OVERVIEW

This dissertation focuses upon nanocomposite materials prepared using the 2:1 phyllosilicate montmorillonite in polymeric systems. Montmorillonite is employed via a solution processing methodology in Chapters III and IV and is employed via extrusion methodologies in Chapter V. Chapter III focuses upon a study of the adsorption behavior of a water soluble hydroxylated hyperbranched polyester intercalated into unmodified sodium montmorillonite (Na^+MMT) clay. An in depth analysis of the morphology by X-ray diffraction (XRD) techniques and transmission electron microscopy (TEM) gives a very clear picture of the adsorption behavior of the hyperbranched polymer onto the clay layers. Chapter IV is focused upon the thermal and free volume properties of the hyperbranched nanocomposite with particular attention paid to the formation of the rigid amorphous fraction (RAF). RAF and the observed morphologies are correlated to a high extent, such that a clear mathematical relationship between the two was derived. Chapter V is focused upon the application of montmorillonite nanocomposites employed in multilayered films with an emphasis on barrier properties and morphological changes with annealing. An improvement of gas barrier properties over materials with much higher clay loadings is observed, which is due to the unique processing conditions that serve to increase clay aspect ratios and concentration concurrently.

CHAPTER III

INTERCALATION BEHAVIOR OF HYDROXYLATED DENDRITIC POLYESTERS IN POLYMER CLAY NANOCOMPOSITES PREPARED FROM AQUEOUS SOLUTION

This chapter was co-authored by Jeremy J. Decker,

Sergei N. Chvalun, and Sergei Nazarenko

Abstract

Second and fourth generations of hydroxylated dendritic polyesters based on 2,2-bis-methylopropionic acid (bis-MPA) with an ethoxylated pentaerytriol (PP50) core were combined with unmodified sodium montmorillonite clay (Na^{+}MMT) in water to generate a broad range of polymer clay nanocomposite films from 0 to 100% wt/wt. X-ray diffraction (XRD) and transmission electron microscopy (TEM) were used to investigate intercalation states of the clay galleries. Intercalation was the dominant state in these nanocomposites. Significant exfoliation was only observed within 0-5% wt/wt of mineral composition range. It was shown that interlayer spacing changed within the composition range 5-95% wt/wt from 0.5 nm to up to 3.5 nm in a step-like fashion with 0.5 nm increments which corresponded to a flattened conformation of confined hyperbranched polymers (HBP). Second and fourth generations exhibited the same layer-by-layer intercalation of completely flattened HBPs. No dependence of interlayer spacings on generation number was found. XRD and TEM revealed the presence of mixed intercalated populations with interlayer spacings at multiples of 0.5 nm.

Introduction

Research has intensified in the area of dendritic polymers due to their highly branched structures, which possess high end group functionality, structures, and unique properties [1-2]. In addition, due to their highly branched structures, dendritic polymers are almost exclusively amorphous in character. From a processing perspective, dendritic polymers often exhibit lower melt and solution viscosities as compared to their linear analogues with the same molecular weights. This is attributed to a lack of entanglements in solution. Dendritic macromolecules are comprised of two classes: dendrimers and hyperbranched polymers. Both are macromolecular compounds built from multifunctional monomers AB_n, where the A and B functionalities couple to form branched structures. Dendrimers are characterized by monodispersity and perfect branching from a central core with multistep synthetic routes, whereas hyperbranched polymers (HBPs) are made by one-pot synthesis and possess less perfect structures and incomplete branch coupling. Hyperbranched polymers, due to their ease of manufacture (relative to dendrimers), offer similar properties, at greatly reduced cost. This has led to increased research of these materials in recent years.

Perhaps due to their ease of accessibility, dendritic hyperbranched polyester polyols based on 2,2-bis-methylopropionic acid (bis-MPA) with an ethoxylated pentaerytriol (PP50) core became a popular model system in a number of studies investigating the chemical structure and physical properties of these systems [3-9]. The pseudo-one-step, divergent synthesis of these aliphatic-ester dendritic polymers was first described by Malmström et al. in 1995 [10]. The creation of these hyperbranched polymers involves the sequential addition of monomer during synthesis and was further

investigated in a number of publications [11-13]. Although characterized by imperfect branching and significant polydispersity, these polymeric structures preserve the essential features of dendrimers, namely, high end-group functionality and a globular architecture. Importantly these HBPs are water soluble due to the strong influence of their hydroxylated end groups [14].

A novel nanocomposite study was conducted with these particular HBPs by Månson's group [15]. It was followed by a series of papers further exploring the behavior of these novel nanocomposites [16-18]. In these studies they prepared HBP/clay nanocomposites via a solution intercalation method using the hyperbranched polyesters and unmodified sodium montmorillonite clay with water as the solvent to yield nanocomposite films. Previous work with water-soluble linear polymers, such as PEO, PVA, and PVP, had successfully demonstrated intercalation of polymer into unmodified clay galleries using this type of methodology [19-20]. With the HBP nanocomposite work, it was anticipated that intercalation of these globular HBPs would lead to larger interlayer spacings than with linear polymers, as collapse of the dendritic structures onto silicate layers could be sterically restricted. So, novel nanocomposites using second, third, and fourth generations of HBPs were previously prepared and studied, and it was concluded that at intermediate Na^{+}MMT contents the interlayer spacings in the resulting intercalated nanocomposites correlated closely with estimates of the molecular diameters for the different generations of HBPs employed. However, at larger mineral contents, the effects of nanoclay confinement led to a flattening of the HBPs. These conclusions were based upon XRD data.

The research carried out by Månson's group became a starting point for this investigation, which was driven by our fundamental interest in exploring the confinement of polymeric structures, in particular dendritic polymers, on the nanoscale level. The adsorption behavior of dendrimers and HBPs on the substrate was in the past predominantly investigated by using the surface techniques such as AFM and ellipsometry [21-22]. However, these studies only allowed study of the adsorption behavior by deposition on a solid substrate. Another potential method to investigate adsorption and confinement of polymeric structures at the nanoscale level is through the utilization of polymer-clay nanocomposites. These offer additional levels of confinement, via intercalated nanocomposite structures, which introduce polymers to multiple substrate interactions.

The main goal of the project described in this chapter was to revisit the nanocomposite work conducted by Månson's group with an emphasis on preparing a very broad, and very detailed, range of nanocomposites, using a very small 5% wt/wt step, from 0 to 100% wt/wt. The intercalation behavior of these hydroxylated dendritic polyesters as a function of clay content was then investigated by a tandem of X-ray diffraction (XRD) and transmission electron microscopy (TEM). It was anticipated that XRD would be particularly revealing at larger mineral content and TEM at smaller mineral compositions. The confinement effects upon these flattened hyperbranched polymers are detailed in an accompanying publication utilizing differential scanning calorimetry and positron annihilation lifetime spectroscopy.

The practical rationale for this research can be stated as follows. Polymer clay nanocomposites have received significant attention in the recent decades because they

often exhibit chemical and physical properties that differ from those of conventional composite materials [19,20,23]. Due to their inherent hydrophilicity, layered silicates such as sodium montmorillonite (Na^+MMT) generally require surfactant modification to increase the organophilicity of the clays in order to promote dispersion in a polymer matrix. However, some hydrophilic polymers exhibit an affinity for the hydrophilic clay layers and therefore nanocomposites can be prepared by the aqueous blending of these polymers and clay without the introduction of surfactants. While hydrophilic polymers such as poly(vinyl alcohol) have been successfully used to prepare nanocomposites with Na^+MMT, conventional polymer solutions often possess a high viscosity and can require shear intensive processing procedures [24]. The utilization of hydrophilic hydroxylated hyperbranched polyesters, which possesses low solution viscosities, allows for easy processing of nanocomposites with Na^+MMT up to very high clay contents. These nanocomposites may also potentially be used as an alternative to organoclays prepared by cation exchange reactions and dispersed into other polymer matrices [25].

Experimental

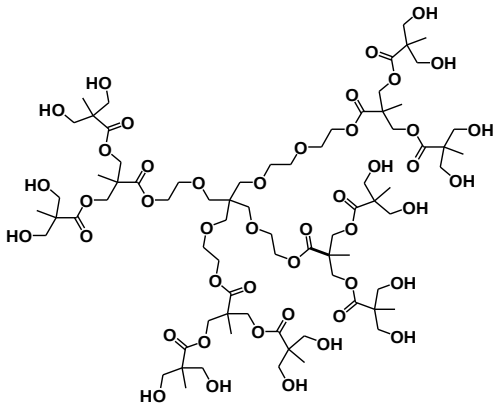

Figure 6. Schematic representation of the idealized structure for the second pseudogeneration HBP.

Sodium montmorillonite clay (Na-MMT) Cloisite® with a cation exchange capacity (CEC) of 92.6 meq/100 g was purchased from Southern Clay Products. As received, clay powder was sifted through a 75 micron sieve, dried at 150°C under vacuum overnight, and stored over desiccant prior to use. Two hydroxyl-functional dendritic (hyperbranched) polyesters, Boltorn™ H20 and H40 (2^{nd} and 4^{th} pseudogenerations, respectively), were obtained from Perstorp Specialty Chemicals AB, Sweden, in the form of pellets. HBP2 and HBP4 will henceforth be used to designate the second and the fourth pseudogenerations of these hydroxylated hyperbranched polyesters. A schematic representation of the idealized structure of the second pseudogeneration of the hyperbranched polyester is shown in figure 6.

Nanocomposites were prepared via a solution-intercalation method using deionized (DI) water as the solvent medium. The processing methodology was based upon that proposed by Plummer et al. [15]. The required amount of Na^{+}MMT clay was first dispersed in DI water at 50°C temperature and stirred for at least 8 hours to optimize clay delamination. The concentration of clay in the deionized water was kept below 1% (wt/wt) in order to ensure that individual clay layers were well dispersed. Sufficiently diluted, sodium montmorillonite particles delaminate into single layers [26].

The required amount of Boltorn™ polyols was then dissolved in boiling DI water. The concentration of polymer in water was kept at or below 10% (wt/wt), as this concentration was seen to effectively disperse and dissolve the HBP at or near 100°C. This solution was then quantitatively transferred into the clay dispersion. This combined solution was then rapidly stirred in open air at 50°C until the dispersion approached the level of the stir bar but remained in a liquid state. It was then transferred to Teflon trays

and dried for 2 days in a convection oven at 50°C. Two further days of drying followed, under vacuum, at 120°C. This temperature was demonstrated as optimal for removing water from Boltorn™ polyols [27]. The resulting nanocomposite films were stored over desiccant at room temperature.

One dimensional X-ray diffraction spectra were collected on a Rigaku Ultima III diffractometer (Cu Kα radiation, λ = 1.542Å) at room temperature using Bragg-Brentano parafocusing geometry (reflection mode XRD). XRD information was obtained from samples powdered in an analytical mill and from intact nanocomposite films. Powdered samples ensured that the Debye-Sherrer diffraction rings were distributed evenly, thus eliminating orientational effects of the HBP and silicate layers in the nanocomposite. The use of powdered samples also ensures an accurate representation of the entire bulk sample and is the most accurate method for obtaining representative d-spacing behavior for a nanocomposite structure.

In all cases, samples were analyzed immediately after removal from the dessicator to reduce water uptake. For optimal consistency, the angular positions of peaks were resolved using the peak search algorithm of MDI Jade 7©. Two dimensional (2D) transmission XRD analysis was performed using photographic film located 50 mm from the sample films at room temperature using a Ni-filtered Cu Kα source. The X-ray beam was transmitted parallel to the plane of the nanocomposite film.

Small angle X-ray scattering (SAXS) was employed to resolve *d*-spacing values larger or comparable to 3 nm that could not be resolved by the 1D wide angle XRD apparatus. The experiments were carried out at room temperature in transmission mode using a Kratky block camera and Ni-filtered CuKα radiation. Film samples were tested.

The diverging and receiving slits were both 100 μm wide, providing a high resolution. The half-width of the primary beam was $3.3 \cdot 10^{-2}$ nm^{-1}. The scattered intensity was measured at angular increments of $1.2 \cdot 10^{-1} nm^{-1}$. Because of possible texture present in the prepared samples with silicate layers oriented parallel to substrate, the diffractograms were recorded in the direction perpendicular and parallel to the film plane.

For transmission electron microscopy (TEM) the nanocomposite films were embedded in epoxy resin and the embedded films were trimmed so that the centers of the films, removed from direct contact with the embedding medium, could be microtomed. About 90 nm thick sections were cut at T = -30°C in the direction perpendicular to the film normal using a Leica cryo-ultramicrotome FC6 equipped with glass knives. These sections were imaged using a Zeiss 109T TEM operated at 80 kV under bright field conditions. Since the silicate layers have a higher electron density than the surrounding HBP matrix, they appear darker in the images. Image analysis of the intercalated samples was carried out using UTHSCSA Image Tool version 3.00.

Density measurements of the nanocomposites were performed using a buoyancy method. The densities of the nanocomposite films were matched with that of an inert liquid. Solutions of methylene Chloride, dibromoethane, chloroform, and bromoform were used for the test solutions. The experiments were carried out in a graduate cylinder equipped with a stir bar. Nanocomposite films averaging 25 mm^2 were immersed in the solvent solution and the density of the solution was adjusted by solvent addition. When films migrated neither up nor down in the static graduated cylinder solution over a 15 minute time period, the solution density was measured by hydrometer and taken as equivalent to the film density.

Results and Discussion

Intercalation Behavior Probed by XRD

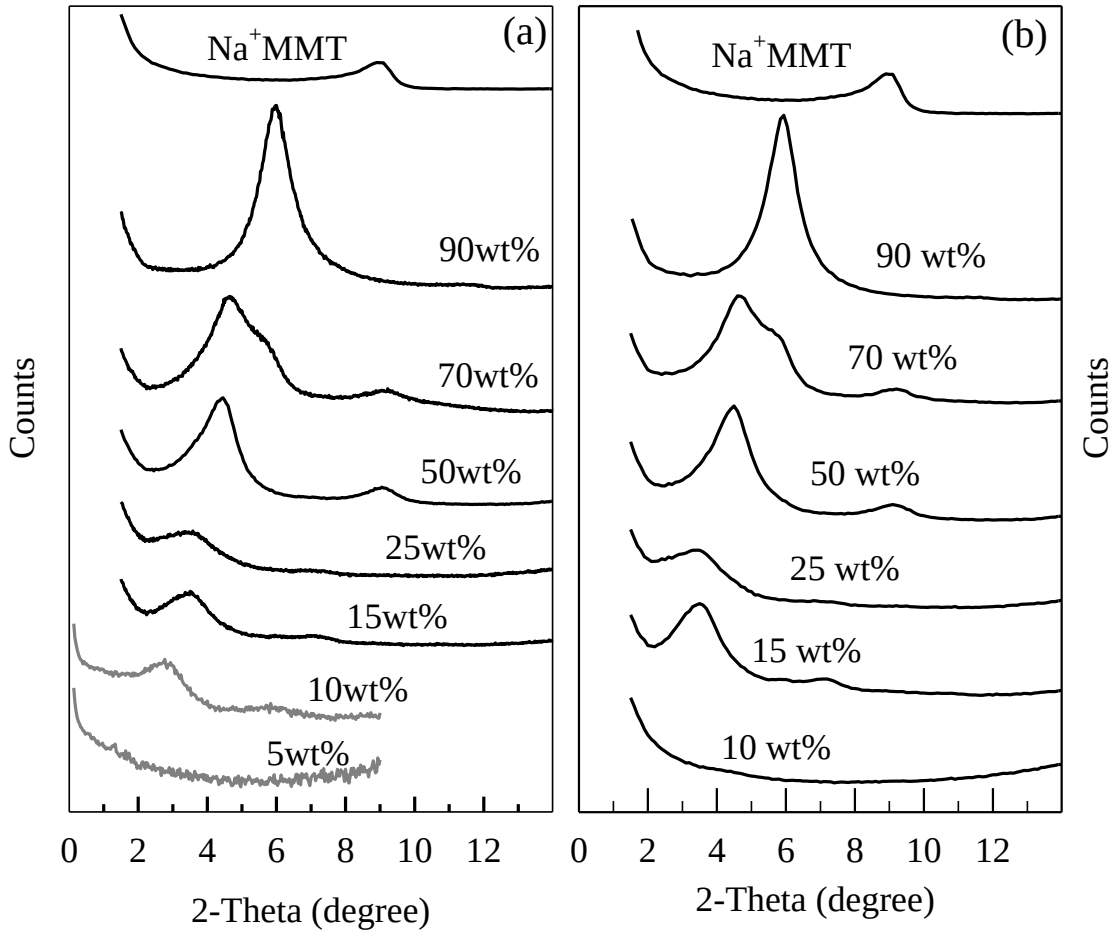

Figure 7. Representative XRD data for HBP4 (a) and HBP2 (b) nanocomposites for varying clay compositions. Solid black lines indicate powdered nanocomposite films analyzed by WAXS; gray lines indicate films analyzed by SAXS.

Figure 7 shows two sets of representative XRD scans of HBP4/Na^+MMT and HBP2/Na^+MMT nanocomposite systems containing different amounts of Na^+MMT, which in this study was varied from 5 to 95% wt/wt. The figures also include a pristine Na^+MMT control for comparison. The data represent a combination of wide (larger mineral content) and small (smaller mineral content) angle XRDs. Wide angle diffractograms were obtained using powder samples, while small angle data were

obtained using film samples with the beam in plane to the film. The HBP4/Na^+MMT and HBP2/Na^+MMT nanocomposite systems showed similar XRD behavior and, therefore, later in this chapter they are either presented together or the data for HBP4/Na^+MMT is presented separately to illustrate more detailed behavior.

The diffractograms for nanocomposites at or above 10wt% (HBP4) and 15wt% (HBP2) demonstrated clear clay intercalation behavior. Interestingly, these diffractograms exhibited for some compositions one and for some compositions two or more overlapping first order diffraction peaks. Intercalation related XRD peaks originate from a constructive interference of the X-ray beam diffracted from a set of parallel silicate layers constituting an ordered clay tactoid. Using Bragg's law the *d*-spacings can be calculated. The interlayer spacing, *l*, subsequently can be calculated by subtracting the crystalline silicate sheet thickness (0.96 nm, as determined from XRD analysis of dried Na^+MMT) from the *d*-spacing. Intercalation of the dendritic polymer between the layers increases the interlayer spacing of the pristine clay and leads to smaller diffraction peak angles. XRD data with several diffraction peaks implied that two or more intercalated clay populations with different interlayer spacing coexisted at least in some HBP nanocomposite systems. Diffraction peaks shifted to lower angles corresponding to larger interlayer spacings with the decreasing of clay content. The diffractograms for nanocomposites below 10wt% (HBP4) and 15wt% (HBP2) showed no clear diffraction peaks, indicative of a transition from ordered intercalated structure at larger clay concentrations to a disordered intercalated structure followed first by partial, and perhaps eventually, complete, clay exfoliation at progressively smaller clay concentrations.

Table 2

Angular Positions and Interlayer Spacings of XRD Data for HBP4 Nanocomposites

% wt/wt Na^+MMT	Angular Position (2Θ)				Interlayer Spacings (nm)			
	1st order		2nd order		1st order		2nd order	
10	2.83		5.83		2.16		2.07	
15	3.50		6.10	7.14	1.56		1.94	1.51
20	3.57		7.10		1.51		1.53	
25	3.58		6.97		1.51		1.58	
30	3.49		5.87	7.10	1.57		2.05	1.53
35	3.58		7.12	8.84	1.51		1.52	1.04
40	3.64		7.08	9.12	1.47		1.54	0.98
45	3.60	4.37	7.28	9.19	1.49	1.06	1.47	0.96
50	4.49		7.16	9.20	1.01		1.51	0.96
55	4.51		7.10	9.43	1.00		1.53	0.91
60	4.45		7.07	9.15	1.02		1.54	0.97
65	4.64	5.71	9.12		0.94	0.59	0.98	
70	4.62	5.75	9.22		0.95	0.58	0.96	
75	4.82	5.77	9.37		0.87	0.57	0.93	
80	4.63	5.82	8.73	11.58	0.95	0.56	1.06	0.57
85	5.84		-		0.55		-	
90	6.00		11.42		0.51		0.59	
95	6.13		-		0.48		-	

Multiple angular positions and interlayer spacings of the same order are shown in split cells.

Table 3

Angular Positions and Interlayer Spacings of XRD Data for HBP2 Nanocomposites

% wt/wt Na^+MMT	Angular Position (2Θ)		Interlayer Spacings (nm)	
	1st order	2nd order	1st order	2nd order
15	3.44	6.00 / 7.10	1.60	1.98 / 1.53
20	3.37	7.16	1.66	1.51
25	3.43	7.12	1.61	1.52
30	3.71	9.32	1.42	0.94
40	4.30	7.04 / 9.11	1.09	1.55 / 0.98
50	4.50	9.10	1.00	0.98
60	4.51	9.11	1.00	0.98
70	4.60 / 5.55	9.20	0.96 / 0.63	0.96
80	5.89	9.04 / 11.51	0.54	1.00 / 0.58
90	5.90	11.66	0.54	0.56

Multiple angular positions and interlayer spacings of the same order are shown in split cells.

A detailed analysis of interlayer spacing behavior as a function of mineral content for HBP4/Na^+MMT and HBP2/Na^+MMT nanocomposite systems is presented in Table 2 and is also shown in Figure 8. Figure 10 and Scheme 1 are used in conjunction with Table 2, Table 3 and Figure 8. Figure 10 presents direct XRD data and Scheme 1 illustrates this complex interlayer spacing (intercalation) behavior. For presentation clarity XRD supporting Figures 10 includes a grid, which indicates angular positions of

several first (guide arrows up) and second (guide arrows down) order reflections associated with various interlayer spacings.

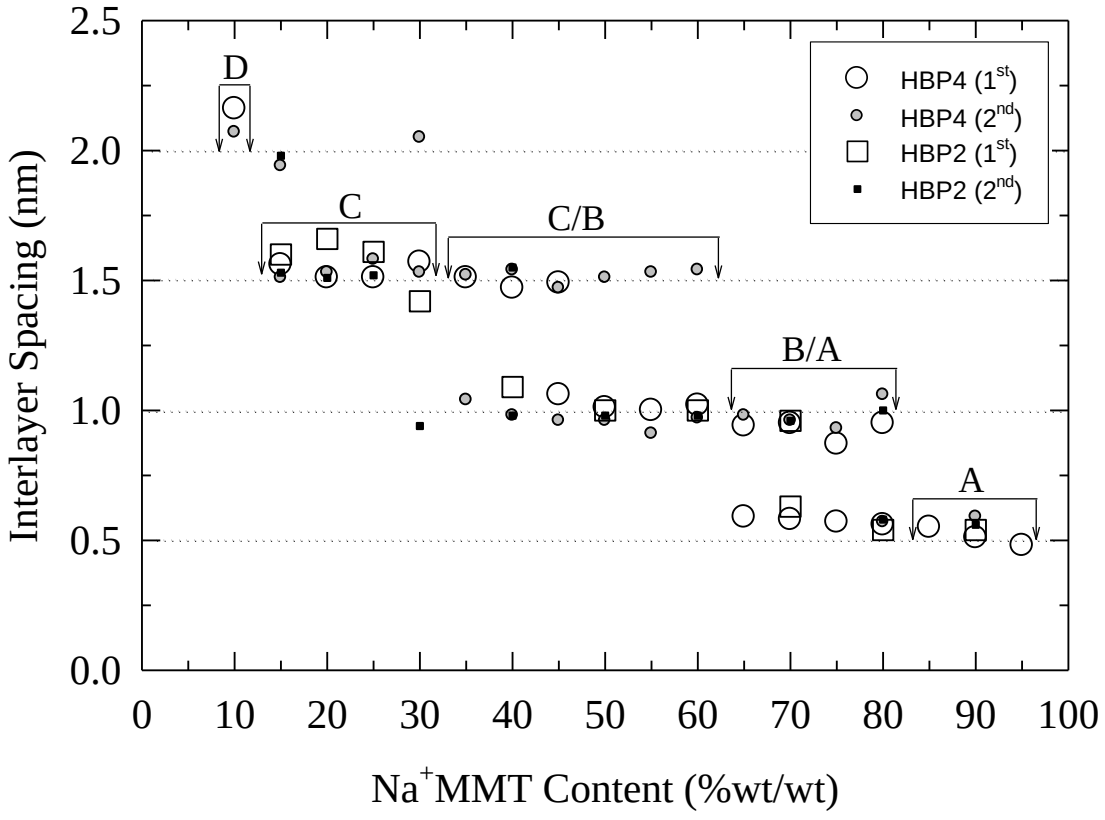

Figure 8. Interlayer spacing behavior observed in HBP4 and HBP2 nanocomposites as a function of % wt/wt Na^+MMT. Large and small circles are the data calculated using first and second order diffraction peaks respectively for HBP4 systems. Large and small squares are the data calculated using first and second order peaks respectively for HBP2 systems. Letters A-D and highlighted regions are indicated in discussion.

Interlayer spacing (spacings) were determined from the first order intercalation peaks and from second order diffraction peaks. The second order diffraction peaks often allowed us to elucidate multiple *d*-spacings even more accurately, as these peaks were angularly much better resolved and exhibited less overlap compared to the corresponding first order peaks. Investigation of the interlayer spacings for the intercalated nanocomposites prepared from both HBP4 and HBP2 clearly showed an incremental

increase of the interlayer spacing as the clay content decreased. As clay content went from the highest levels to the lowest, the interlayer spacings progressed from a minimum of about 0.5 nm to a maximum of about 2.0 nm with a step size of about 0.5 nm. It appears that this 0.5 nm increment corresponds to the vertical spacing of HBP molecules if they adopt a flattened (planar) conformation. Indeed, layer thickness of 0.5 nm closely resembles the calculated vertical spacing of linear aliphatic polyester chains when exhibiting planar conformations, as determined by molecular mechanics computations [28].

It is useful to note here that dendrimers with flexible branch units have been predicted by computer simulations to substantially flatten and spread out upon a substrate, dependent upon generation number and interaction strength of the dendrimer to the substrate [29,30]. Indeed, highly compressed and flattened dendritic macromolecules of charged polyamidoamine (PAMAM) have been observed from monolayer deposition upon a charged silicon surface [31-34]. Flexible dendritic polyesters with terminal hydroxyl groups have been shown to preferentially adsorb and flatten upon a mica substrate, which was attributed to attractive forces between the negatively charged mica surface and the hydroxyl moieties of the polyesters [35]. It has also been demonstrated that dendritic macromolecules composed of flexible branch units tend to deform under external stresses, whether due to external compressive forces or due to polymer/ substrate interactions [22].

Therefore, we argue here that the observed incremental changes in interlayer spacing are in agreement with a process of intercalation which assumes a layer-by-layer deposition of flattened HBP molecules. This process implies incorporation between the

silicate sheets first of a flattened HBP mono-layer, then a bi-layer, a tri-layer, etc. This proposed HBP intercalation behavior, which involves the flattening of HBP molecules, is therefore similar to that suggested originally by Rodlert et al. [16]. However, they concluded this behavior only in the region of high mineral content. In the middle and low mineral composition range the authors hypothesized, based on their XRD data, the possibility of intercalation between silicate layers of HBPs which maintained a globular (spherical) conformation. These conclusions, however, were based upon smaller data sets than that generated in the current work. In either case, this stepwise increase of interlayer spacing observed for HBP clay nanocomposites with decreasing of mineral content considerably differs from that reported for clay nanocomposites prepared using water soluble linear polymers, for instance PVOH, where a more gradual increase has been reported [24].

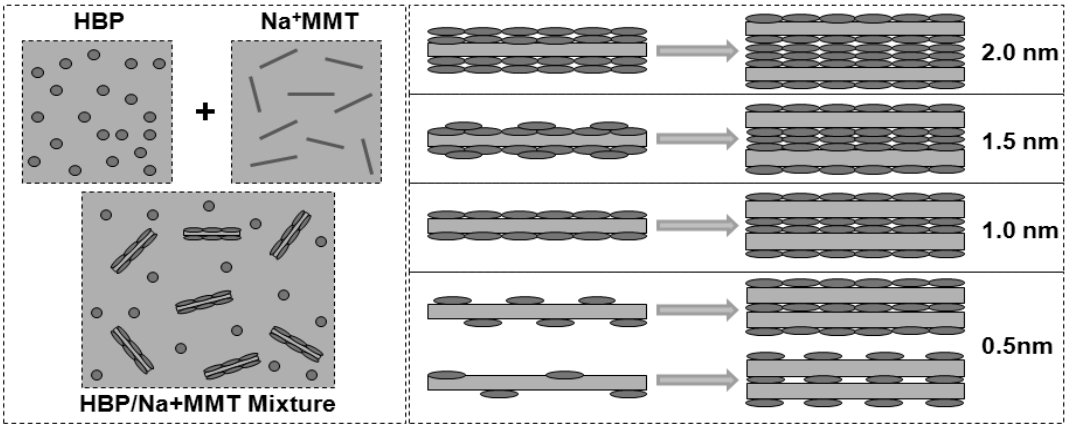

Scheme 1. Pictorial model for proposed stepwise layer formation of hyperbranched polymer into montmorillonite galleries.

The process that may describe the stepwise increase of interlayer spacings is shown pictorially in Scheme 1. It is important to start from a discussion of the solution to understand the overall behavior. The concentration of clay and polymer in water was

always chosen to be smaller than 1% wt/wt and 10% wt/wt correspondingly. Under these conditions, the clay sheets were delaminated and the polymer was in solution. The amount of surface coverage should generally depend on relative concentration of clay and polymer in the solution. We believe that the HBP molecules adopt this planar conformation already in the solution when they adsorb onto the clay surface. The confinement leading to flattening likely occurs due to interaction between the polar shell (the hydroxylated periphery structures of the HBP molecules) with the charged silicate layers. During processing, as the water evaporates, the solution concentration increases, leading to increased clay/polymer interactions. The transformation to nanocomposite occurs as a result of re-aggregation and the stacking of HBP covered clay layers. The mechanism of how restacking takes place is not apparent, and we make no claims towards thermodynamic or kinetic factors here. However, we may think that lower viscosity during HBP nanocomposite processing plays an important role in the observed quantization of interlayer spacings. This is in contrast to aforementioned nanocomposites prepared with some water soluble linear polymeric systems, where viscosity is a much more inhibiting factor and clearly impacts the intercalation behavior [24].

An in depth discussion of the observations made by XRD follows. The next several paragraphs describe in detail the different regions of interlayer spacing behavior as probed by XRD with regard to mineral composition. This discussion proceeds from the highest clay loadings to the lowest in order to explain the interlayer behavior observed.

The nanocomposites containing 85-95 wt% MMT, region A, as shown in Figure 8, exhibited an interlayer spacing of about 0.5 nm implying that on average one flat HBP

monolayer separates clay sheets in the intercalated tactoids. The composition of clay in an ideal hybrid nanocomposite structure consisting of perfect alternating layers of flattened HBP and the silicate with thicknesses 0.5 nm and 0.96 nm (individual clay sheet thickness) can be calculated as follows. For these calculations we used the bulk density of dried HPB4 as measured in this study, 1.306 g/cm^3, and clay density as reported by Southern Clay Products LLC, 2.86 g/cm^3. These calculations of volume and weight content for this ideal hybrid structure were conducted and yielded a perfect hybrid with an interlayer spacing of 0.5 nm at 66% vol/vol and 81% wt/wt Na^+MMT. Notably, this weight (volume) fraction was found to be very close to the point of transition from monolayer to bilayer spacing as shown in Figure 8. Above 81% wt/wt Na^+MMT it is not unreasonable to conclude that the HBP monolayer may only be formed from an incomplete coverage of the clay layers upon reaggregation. It is clear that even with this incomplete coverage, the clay layers maintain an ordered structure, as demonstrated by the presence of the X-ray scattering peaks.

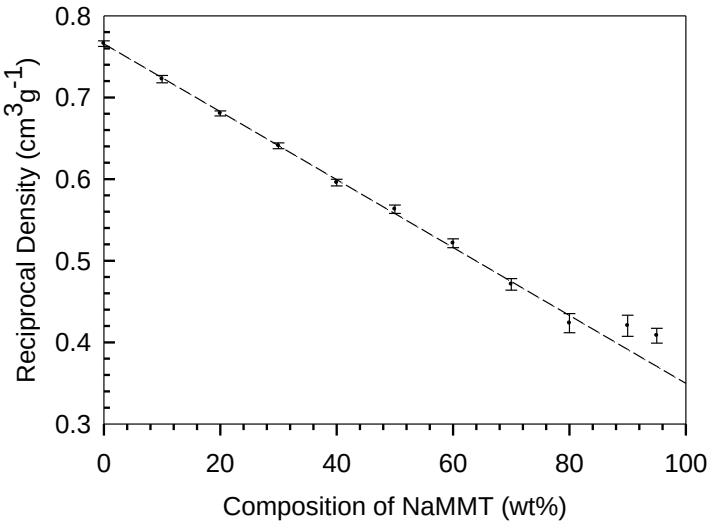

Figure 9. Reciprocal density of HBP4/Na^+MMT nanocomposites as a function of clay content.

Since the surface coverage calculation indicated that above 81% (wt/wt) there is an incomplete surface coverage of the clay layers, it was reasonable to attempt to verify this behavior. In fact, similar question can reasonably be posed with regard to any of the transitional regions associated with incomplete coverage of the clay sheets by the second, third, etc. flattened HBP layers. To explore this behavior the nanocomposite density was measured over the mineral composition range. A linear dependence of reciprocal density versus weight content of clay can be expected if the surface coverage obeyed two phase model behavior, i.e. only polymer and clay with no voids present. Reciprocal densities ($1/\rho$) versus wt/wt% MMT for HBP/Na^+MMT nanocomposites are shown in Figure 9. The dashed line represents the two phase model prediction assuming clay and polymer bulk densities are unchanged and clay surface coverage is complete. Deviation from predicted two phase behavior is observed only for nanocomposites exhibiting 90 and 95 wt% Na^+MMT. In the mineral range 0-80% wt% no clear deviation from predicted two-phase trend is evident. This implies that either no voids were forming at lower mineral content or the density method used here was not sensitive enough to detect any perceptible deviation from the two phase model behavior. However, this method provided proof that HBP/clay hybrids in the high mineral content region A contained a noticeable amount of nanoscale voids. Whether these nanocomposites represent a fundamentally interesting and practically useful class of nanoporous polymer clay hybrids are to be investigated.

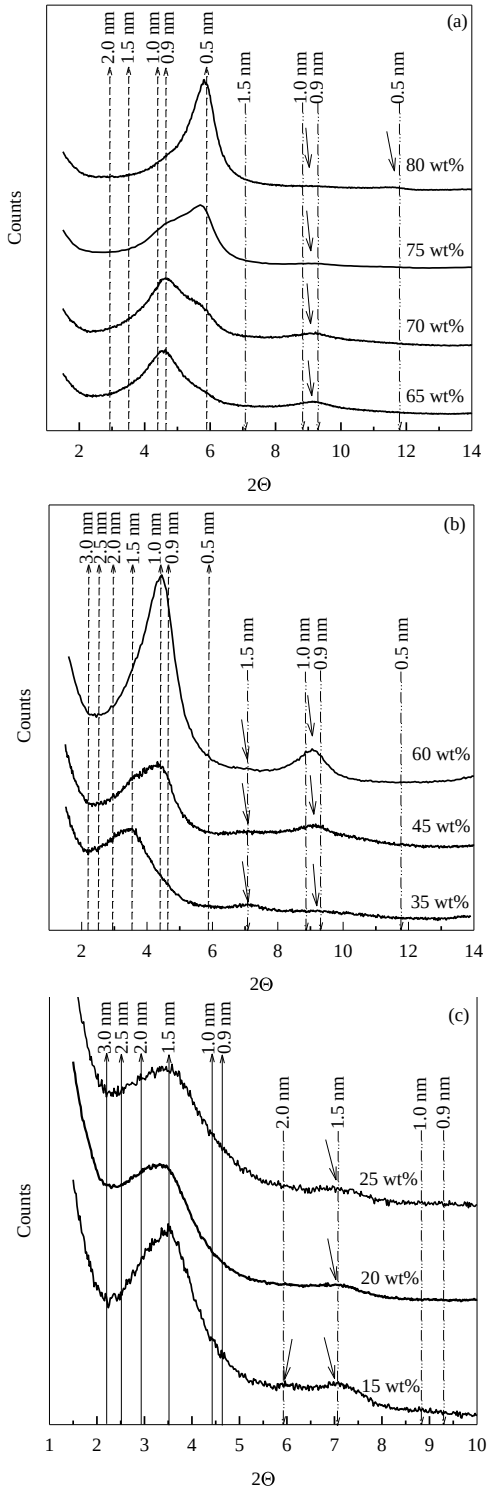

Figure 10. XRD data of HBP4 nanocomposites representing (a) region B/A (80-65% wt/wt Na^{+}MMT), (b) region C/B (60-35% wt/wt Na^{+}MMT), and(c) region C (30-15% wt/wt Na^{+}MMT). Angled downward arrows indicate second order reflections.

A characteristic feature of the compositional region B/A (80% to 65% wt/wt MMT) was that at least two different intercalated populations with an interlayer spacing about 0.5 nm and 1.0 nm apparently coexisted in the nanocomposite structure. The interlayer spacing of 1.0 nm implied that on average two flat monolayers (a bilayer) separate clay sheets. Figure 10a presents supporting XRD data obtained using powdered HBP4/Na^+MMT nanocomposite systems to illustrate the behavior. For clarity of presentation, Figure 10 includes lines which indicate the angular positions of several first (dashed line, arrows up) and second (dashed-dotted line, arrows down) order reflections associated with various interlayer spacings. XRD data for HBP4/Na^+MMT and HBP2/Na^+MMT nanocomposite systems were very similar, and therefore, only XRDs for one system are shown. Each of the two coexisting intercalated populations can be directly related to one of the two overlapping diffraction peaks in the range of $4 < 2\Theta < 6$.

At larger mineral content in this region the peak associated with the 0.5 nm interlayer spacing was larger, while the peak associated with 1.0 nm was smaller. With mineral content decreasing the first order peak intensities were gradually reversed. The second order diffraction peak associated with interlayer spacing 1.0 nm also gradually increased with decreasing of wt/wt MMT. At 80% (wt/wt) and 65% (wt/wt) the corresponding XRDs clearly revealed one dominant peak associated subsequently with 0.5 nm and 1.0 nm interlayer spacings. All these facts implied that intercalated populations with interlayer spacing 0.5 nm dominated at larger mineral content of this region and intercalated population with interlayer spacing 1.0 nm dominated at lower mineral content.

Using the same calculations, as discussed previously, for determining a perfect hybrid with 1.0 nm interlayers, yields a perfect hybrid with an interlayer spacing of 1.0 nm at 49% vol/vol and 68% wt/wt Na^{+}MMT. It is therefore reasonable to hypothesize that region B/A covers a regime where the nanocomposite structure is transforming from one ideal hybrid structure with 1.0 nm interlayers to one with 0.5 nm interlayers. The process leading to formation of 1.0 nm interlayer spacing can be qualitatively visualized as follows. Prior to intercalated tactoid formation the clay platelets must be predominantly covered by a monolayer of flattened HBPs. Re-aggregation into an intercalated structure results in the formation of the HBP bilayer as shown in Scheme1. Surface coverage of the clay indeed appears to dominate the nanocomposite structure at these higher clay loadings.

As in the case with region B/A the characteristic feature of region C/B, 60% to 35% wt/wt MMT, was two intercalated populations but with interlayer spacings of 1.0 nm and 1.5 nm. The interlayer spacing of 1.5 nm implied that on average three flat monolayers (one trilayer) separated the clay sheets. Figure 10b presents the supporting XRD data (powdered samples) to illustrate this behavior. On each diffractogram one can see two larger overlapping first order diffraction peaks and two well separated smaller second order diffraction peaks corresponding to two intercalated populations with interlayer spacings of about 1.0 nm and 1.5 nm. At larger mineral content the first order XRD peak associated with 1.0 nm intercalated population is larger, while XRD peak associated with the 1.5 nm intercalated population is smaller. The situation is reversed gradually with the decreasing of mineral content. The corresponding second order diffraction peaks behave similarly, with the corresponding peak intensities reversed with

decreasing of mineral content. The process leading to the formation 1.5 nm interlayer spacings is displayed pictorially in Scheme 1. In this case, before clay layer re-aggregation, the clay platelets are completely covered with the first flattened HBP layer and only partially covered by the second layer. Re-aggregation of layers upon nanocomposite formation must lead then to formation of a trilayer sandwiched between clay layers. Calculated volume and weight mineral content of a perfect hybrid with polymer interlayer spacing of 1.5 nm are 39% vol/vol and 58% wt/wt, respectively. It is clear that at 60% wt/wt Na^{+}MMT, the interlayer spacing is predominantly 1.0 nm, as expected from the calculations; however, aside from a broadening of the peaks to lower 2Θ values, there is no conclusive XRD evidence of interlayer populations above 1.5 nm in this region. It was believed that at these lower clay content regimes, the nanocomposites were deviating from a perfect hybrid structure, and a significant amount of free polymer was present. Transmission electron microscopy was used to confirm this assumption. TEM results are reported later in this chapter.

As the clay content was further reduced into region C (30-15 wt% MMT), one broad first order diffraction peak attributed to an interlayer spacing of about 1.5 nm was observed. Figure 10c provides representative XRD data for this region. However, at these lower volume fractions (7-16% vol/vol) of montmorillonite, it is expected that there will be an increase in layer disorder, which will contribute to a weakening and broadening of the basal reflections [36]. From the second order reflections that could be resolved, it is apparent that interlayer populations of 2.0 nm are also present in this range. Indeed, this is not unreasonable, as at lower 2Θ values interlayer spacings correspond to much closer 2Θ values than at larger reflection angles. We attempt to address this

situation in Figure 10 by overlaying an interlayer spacing grid. For HBP4 sample 15% and 30% (wt/wt) representing region C/D we observed one first order diffraction peak attributed to about 1.5 nm interlayer spacing and two smaller second order diffraction peaks attributed to interlayer spacings 1.5 nm and 2.0 nm. With other samples in this range, the second order peaks were too poorly resolved to be reliably determined.

For sample 10% (wt/wt) (Region D) the XRD data was obtained by SAXS of an intact film with the beam transmitted parallel to the film surface. Wide angle measurements of the powdered sample in reflection mode gave XRD data where no basal reflections could be resolved, as the intercalated clay could only be seen when it was in an oriented state and the reflections were, thus, more intense. A broader first order peak with the maximum corresponding to about 2.2 nm was observed. The position of the lower intensity second order diffraction peak showed an interlayer spacing of 2.1 nm. It must also be noted that small angle XRD analysis of HBP4 nanocomposite films with the following compositions were scanned by the small angle apparatus: 5, 10, and 15% wt/wt Na^{+}MMT. When scanned in plane, the data was as shown in Table 3 and Figure 8 (small angle of the 15% wt/wt Na^{+}MMT film was in accord with that of the powdered sample run in wide angle reflection geometry). However, when these samples were scanned with the beam transmitted normal to the film plane, no reflections were observed. This indicated nanoclay orientation in the films themselves, which was subsequently investigated and is addressed later in the chapter.

Due to the observed XRD reflections for the multiple intercalated populations that coexisted in the nanocomposite films, a question as to their origin was posed. The formation of a clay concentration gradient formed in the thickness direction as the high

density clay settled during nanocomposite film preparation was considered to be the most straightforward and plausible reason for explaining the XRD data carried out on powdered samples. It was anticipated in this case that the top surface of a nanocomposite film would exhibit a lower and the bottom a higher than average mineral content. Due to this settling effect, the top surface must then be represented by intercalated population with larger and the bottom surface with smaller interlayer spacings, as they would in effect be in different HBP concentration regimes. To investigate this, the top and bottom surfaces of intact nanocomposite films were probed by XRD operated in reflection mode by scanning each side respectively, while being mindful of maintaining a flat surface and good sample alignment; deviations could lead to a skewing of the resulting data. The corresponding XRD of the top and bottom surfaces of HBP4/Na^{+}MMT (70, 50, and 35% wt/wt) are shown in Figure 11. For presentation clarity the figure includes a grid which indicates angular positions of several first (arrows up) and second (arrows down) order reflections associated with various interlayer spacings.

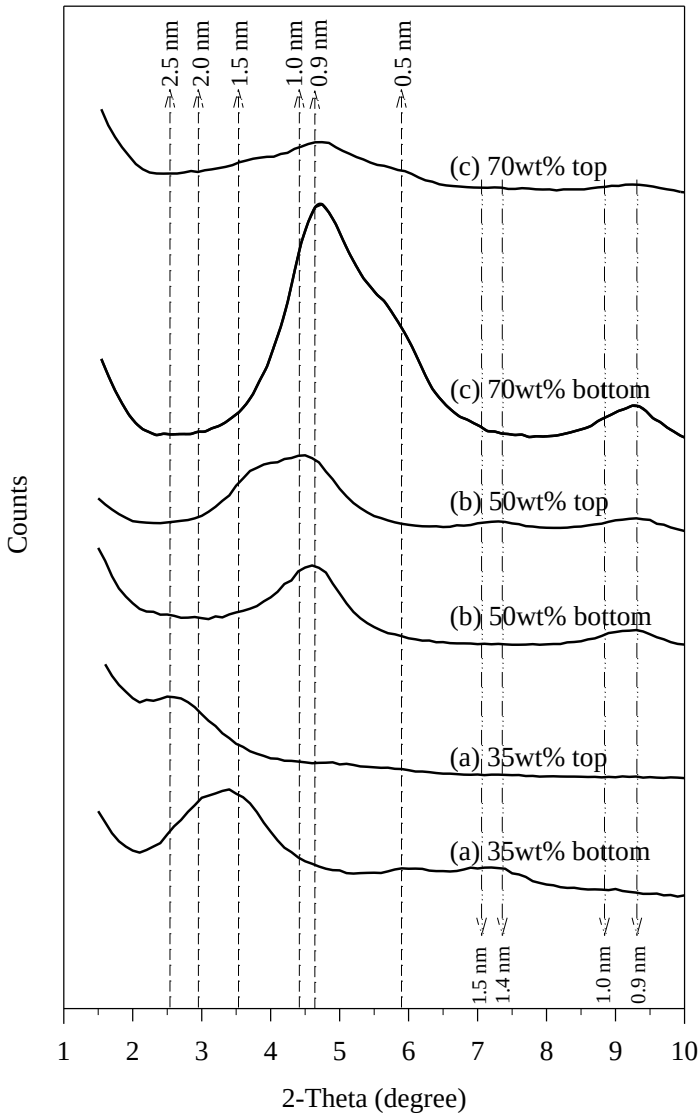

Figure 11. XRD data for intact HBP4 nanocomposite films scanned in reflection mode. Top and bottom of intact films scanned.

Indeed, the diffractograms of the top surfaces were noticeably shifted toward lower angles, indicative of larger interlayer spacings, in comparison with those of the bottom surfaces. As anticipated, this implied that clay settling during film formation caused the formation of a concentration gradient with lower mineral content on the top and larger one on the bottom of the film sample (with an increase in interlayer spacings for the less concentrated regions in the gradient structure). Interestingly, and this was

especially noticeable on XRDs for 70 and 50% (wt/wt) samples shown in Figure 11, the top and bottom surfaces still revealed multiple intercalated populations. The origin of these multiple intercalated populations can be explained in terms of the depth of X-ray sample penetration, from which the scattering data are collected. Clearly, this penetration depth was large enough to cover sizeable portion of the concentration gradient. Vaia et al. estimated for a clay nanocomposite system the sample penetration depth at which a 1000-fold decrease in X-ray incident intensity occurs in the reflection experiment as a function of scattering angle 2Θ and mineral composition, in a previous publication, and we use these estimations here [36]. In the case of layered silicates containing polymeric system for $2\Theta = 2^{o}$ and 4^{o} (this covers our range of 2Θ reasonably well) for 100% layered silicate they calculated 4.6 and 11.5 μm correspondingly, and for 10% (wt/wt) it was 46 and 115 μm. However, these penetration depths are based upon the absorption coefficient of the nanocomposites analyzed, and in the presence of a potential density gradient in the films, these numbers are only used for estimative purposes. Taking into account that the nanocomposite film thicknesses in this work were from 300-500 μm, which is larger than the expected penetration depths for these nanocomposite films, we cannot discount the possibility that there was an additional mechanism responsible for the multiple intercalated populations observed. If there is indeed a cause for the multiple observed populations beyond that of gradient formation, it may be associated with the existence of a statistical distribution of mineral layer coverage. If this is the case, then it is possible that multiple intercalated populations in HBP/clay nanocomposites would exist even if constant concentration could be maintained across the film samples and no

concentration gradients were formed. This is discussed further in the section dealing with the analysis of interlayer spacings by TEM.

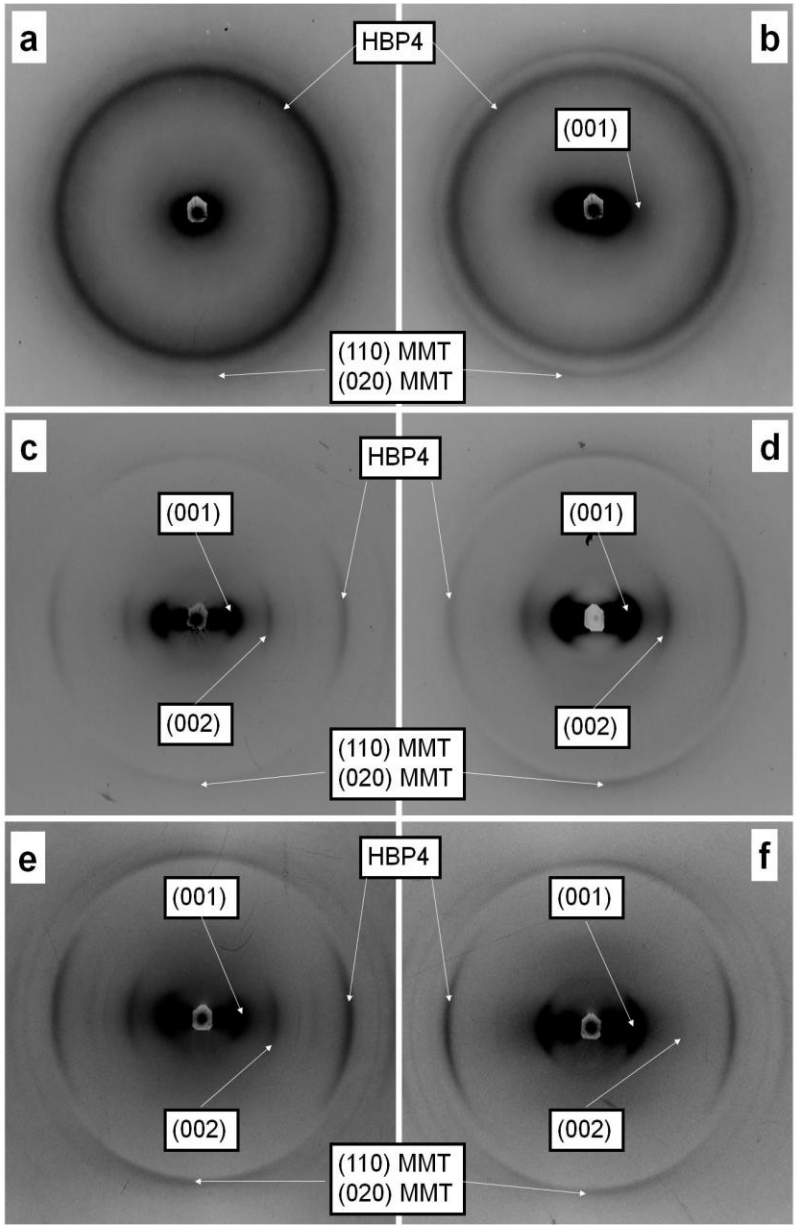

Figure 12. 2D WAXS data for HBP4/Na^+MMT nanocomposite films with X-ray beam transmitted in plane of the film surface. (a) 5 wt% Na^+MMT, (b) 15 wt% Na^+MMT, (c) 25 wt% Na^+MMT, (d) 40 wt% Na^+MMT, (e) 60 wt% Na^+MMT, (f) 90 wt% Na^+MMT.

Continuing further with the analysis of HBP/clay nanocomposite film structure, 2-D XRD experiments were carried out on the solution cast nanocomposite films with the beam transmitted parallel (edgewise) to the surface of the film in order investigate clay orientation in the nanocomposite films. Figure 12 shows the corresponding XRD patterns for sample films containing 5, 15, 25, 40, 60, and 90% wt/wt of clay. The appearance of the diffraction arcs associated with (00*l*) reflections of intercalated silicate layers demonstrated an orientation of the montmorillonite parallel to the film surface. The arcs were more pronounced as clay concentration increased. In addition to (00*l*) reflections, the orientation of the MMT layers was demonstrated by the diffraction arcs associated with (110) and (020) crystalline reflections of MMT clay itself. These reflections are orthogonal to the (00*l*) reflections of the clay basal reflections and grow narrower as orientation increases with silicate loading.

In addition to the clear ordering of the nanoclay in the film, it can be seen that as the composition of clay increases in the polymer matrix, so too does the ordering of the HBP reflection itself. The HBP scattering transitioned from an amorphous halo at the low clay loading of 5% wt/wt MMT to a more narrowed arc with increasing clay loading. This ordering of the HBP diffraction arc is in plane with that of the MMT. This is attributed to a flattening and stretching of the HBP upon the clay layers. As the volume fraction of clay increases, so does the fraction of adsorbed and oriented HBP4, resulting in these narrowed diffraction arcs for the HBP.

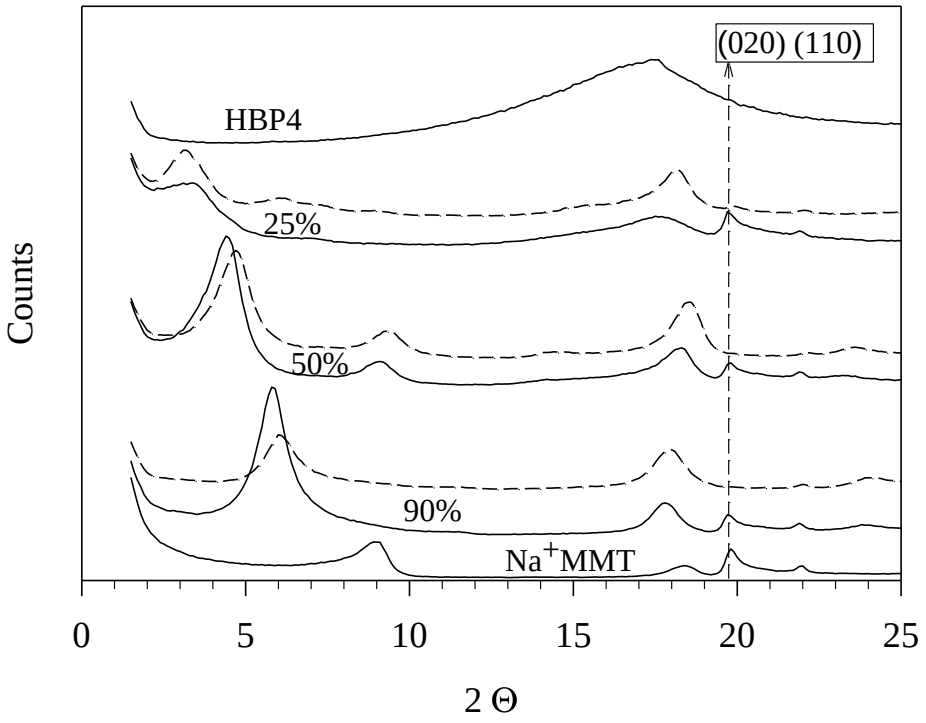

Figure 13. Reflection mode XRD data for HBP4/Na^{+}MMT powders (solid lines), and intact films (dashed lines).

The orientation of the hyperbranched polyester itself was reinforced by comparison of X-ray diffractograms carried out in reflection mode of the powdered and intact nanocomposite films. These data are shown in Figure 13. The orientation of the MMT in the intact nanocomposite films can be observed by tracking the (110) and (020) reflections of the MMT, as previously demonstrated in Figure 12. For the powdered nanocomposite films, these are evident at $2\Theta = 19.8°$ and are visible due to the randomized orientation of the powder. For the nanocomposite films, however, these peaks are virtually nonexistent due to the orientation of the silicate layers parallel to the film surface.

In addition to the nanoclay orientation, there is also a change in the amorphous halo of the HBP4 under confinement, as observed by the 2-D data. There is a narrowing

of the amorphous halo and a shift to higher 2Θ values. Again, this behavior is attributed to flattening and increased orientation of the HBP as it is sandwiched between the clay layers. This provides further evidence; in addition to the observed stepwise interlayer spacing behavior, that the hyperbranched polymers have adopted a flattened structure after adsorption to and confinement by the clay.

Intercalation Behavior Probed by TEM

TEM was used in this work mainly to observe intercalated and exfoliated morphologies of the HBP/clay nanocomposite systems and to investigate average interlayer spacings in order to complement the XRD data. Due to the high degree of orientation of the MMT layers in plane with the film surface, TEM is a useful technique for morphological analysis in these nanocomposite systems, as the clay layers can be readily imaged. Also, smectic clays such as montmorillonite possess a high electron density and can be directly imaged by TEM without the need for staining agents. A limitation of TEM, however, is that unlike X-ray analysis, which investigates a bulk sample, TEM only images small areas of a nanocomposite sample and is limited to observing morphologies one ultrathin section at a time. To counteract this deficiency, a large number of sections were imaged for each nanocomposite film. Because of the observed orientation of the clay layers in plane with the film surface, microtoming of the film edges was optimal for imaging. The knife edge was aligned at 90˚ to the film surface and sectioning proceeded along the film edge. Image analysis software was used to analyze the resulting TEM micrographs. Both interlayer spacings and the number of clay layers in each aggregated clay stack were analyzed.

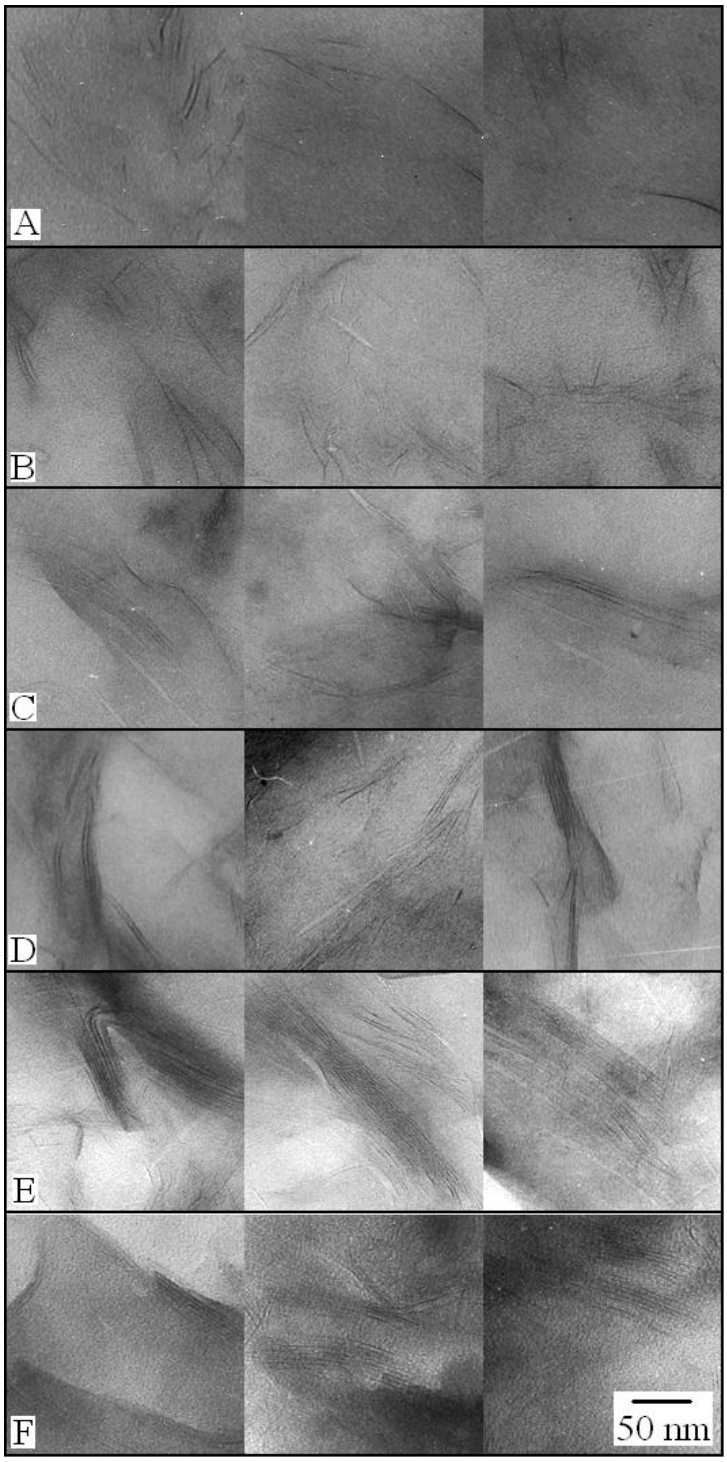

Figure 14. Representative high magnification TEM micrograph sections of HBP4/Na^{+}MMT nanocomposites with (A) 1, (B) 5, (C) 15, (D) 20, (E) 25, and (F) 40% wt/wt clay content.

High resolution TEM images were obtained on samples containing 1, 5, 15, 20, 25, and 40% wt/wt Na^+MMT in HBP4. Numerous representative TEM micrographs for each composition are shown in Figure 14. Nanocomposite films with clay contents greater than 40% wt/wt Na^+MMT proved too brittle to effectively section for microscopy. Image analysis was carried out for galleries of images where the layers could be clearly resolved. The methodology was as follows. When clay layers were observed to be in an ordered intercalated state, which was designated for this study as parallel and less than 10 nm apart, the height of the aggregate was measured from the outer edges of the MMT layers (H), and the number of clay layers (n) was counted. Interlayer spacings (l) were calculated from the aggregate data by assuming the thickness of individual montmorillonite clay layers to be h_c = 0.96 nm, using the following equation: $l = (H - nh_c)/(n-1)$. For the sake of this analysis, exfoliation was defined to be when clay layers were 10 or more nm apart.

The average number of clay layers per intercalated stack within the nanocomposite was determined by averaging the total number of clay layers in the intercalated stacks and the exfoliated clay layers observed (1 layer in a stack). The extent (fraction) of exfoliation (%*E*) was determined by dividing the number of exfoliated clay layers observed by the sum of the number of intercalated and exfoliated clay layers observed. In order to accurately assess both the extent of exfoliation, the average interlayer spacings in the intercalated stacks, and the average number of clay layers per stack, a large statistical sampling of aggregates and exfoliated layers was used. For 1 wt% Na^+MMT, an excess of 300 measurements were taken due to the greater degree of exfoliation, and over 200 measurements were taken for 5 wt% Na^+MMT for the same

reason. For the higher clay content samples, an excess of 100 measurements were taken as the intercalation was far more predominant and each stack contained multiple clay layers.

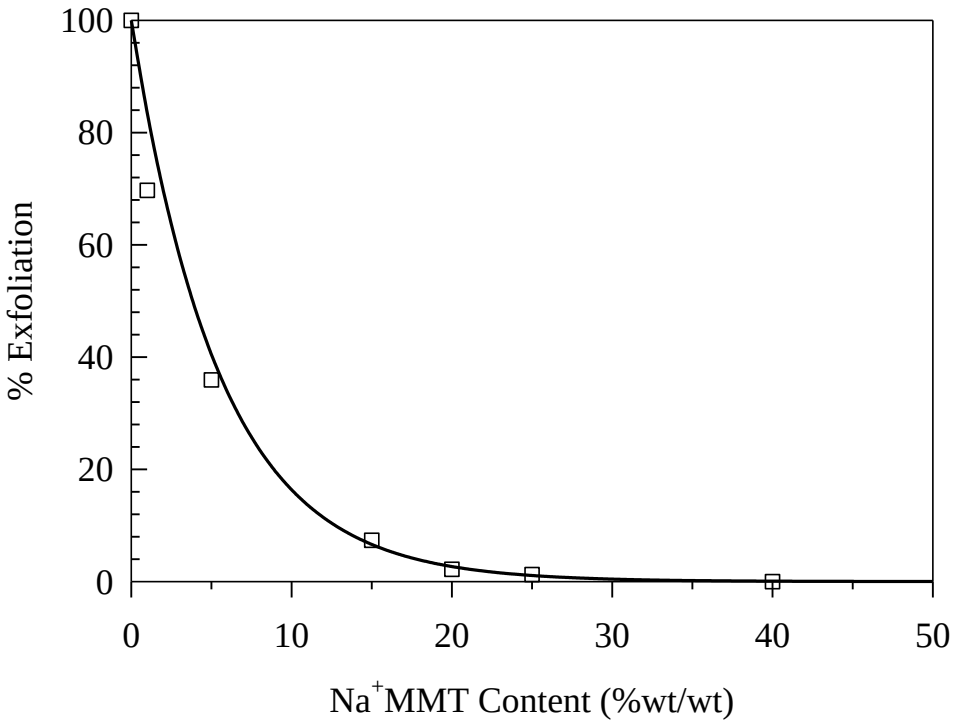

Figure 15. % Exfoliation determined by image analysis of TEM micrographs for HBP4/Na^+MMT nanocomposites.

An analysis of the extent of exfoliation with clay loading is shown in Figure 15. One can clearly see in this Figure that at lower clay contents exfoliation dominated over intercalation but exponentially decreased in favor of an intercalated structure with increasing clay. Regression analysis of the degree of exfoliation *E* as a function of mineral composition w_c (% wt/wt) was performed with the following constraint: 0% wt/wt Na^+MMT must correspond to 100% exfoliation, as this is a natural limit. With this constraint, the extent of exfoliation closely followed the exponential formula $E = \exp(-0.18w_c)$, where w_c represents the weight percent of Na^+MMT.

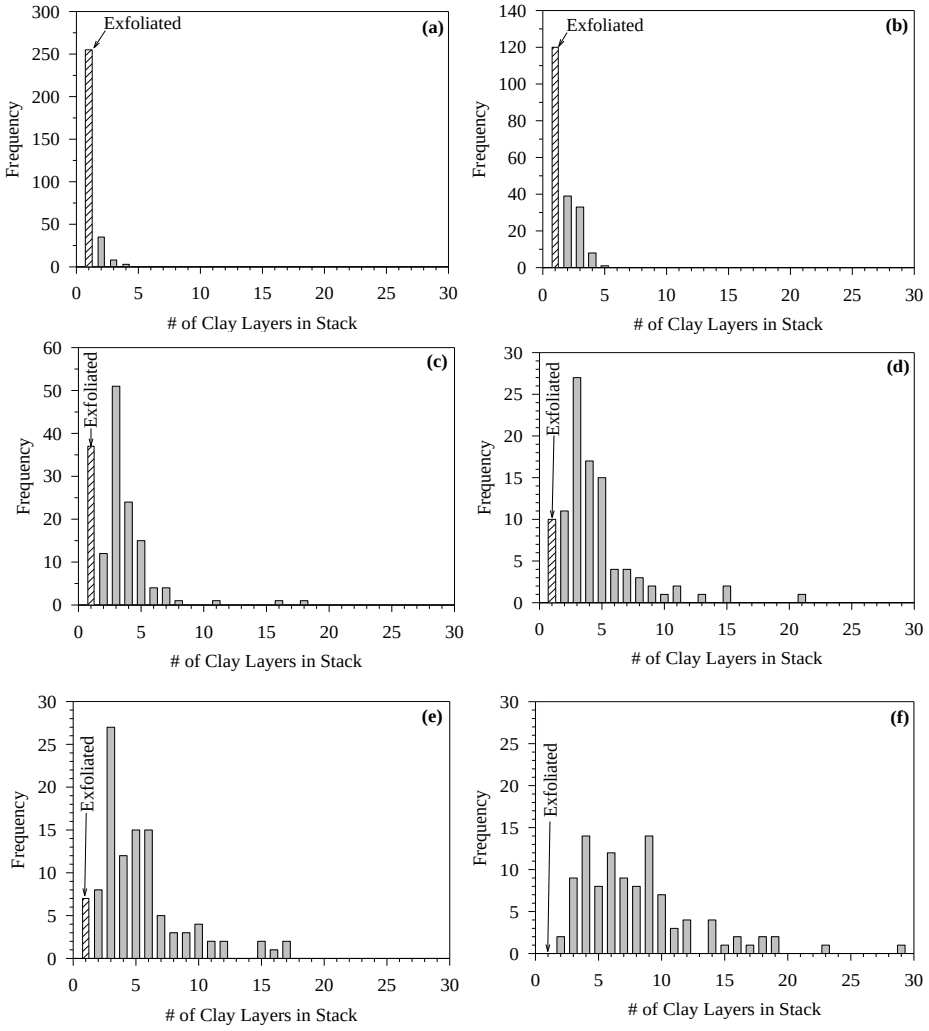

Figure 16. Histograms showing the distribution of clay layers in separate clay stacks for the 4th pseudogeneration nanocomposites analyzed. The following Boltorn H40 with Na+MMT nanocomposite films were analyzed: (a) 1 wt% Na^+MMT, (b) 5 wt% Na^+MMT, (c) 15 wt% Na^+MMT, (d) 20wt% Na^+MMT, (e) 25 wt% Na^+MMT, (f) 40 wt% Na^+MMT. The hashed bar represents the population of exfoliated clay observed in the TEM micrographs (1 clay layer).

Histograms showing the number of layers per intercalated clay stack are displayed in Figure 16. At low clay concentrations, the exfoliation state dominated; however, a small number of intercalated layer stacks can still be found even at mineral content as low as 1%. At 1% and 5% wt/wt the number of layers per intercalated stacks is very small (2-4 layers). This distribution broadened considerably with higher mineral content.

At 40% wt/wt of clay a very broad range of layer stacks can be observed, with the majority of stacks containing less than 10 layers per aggregate.

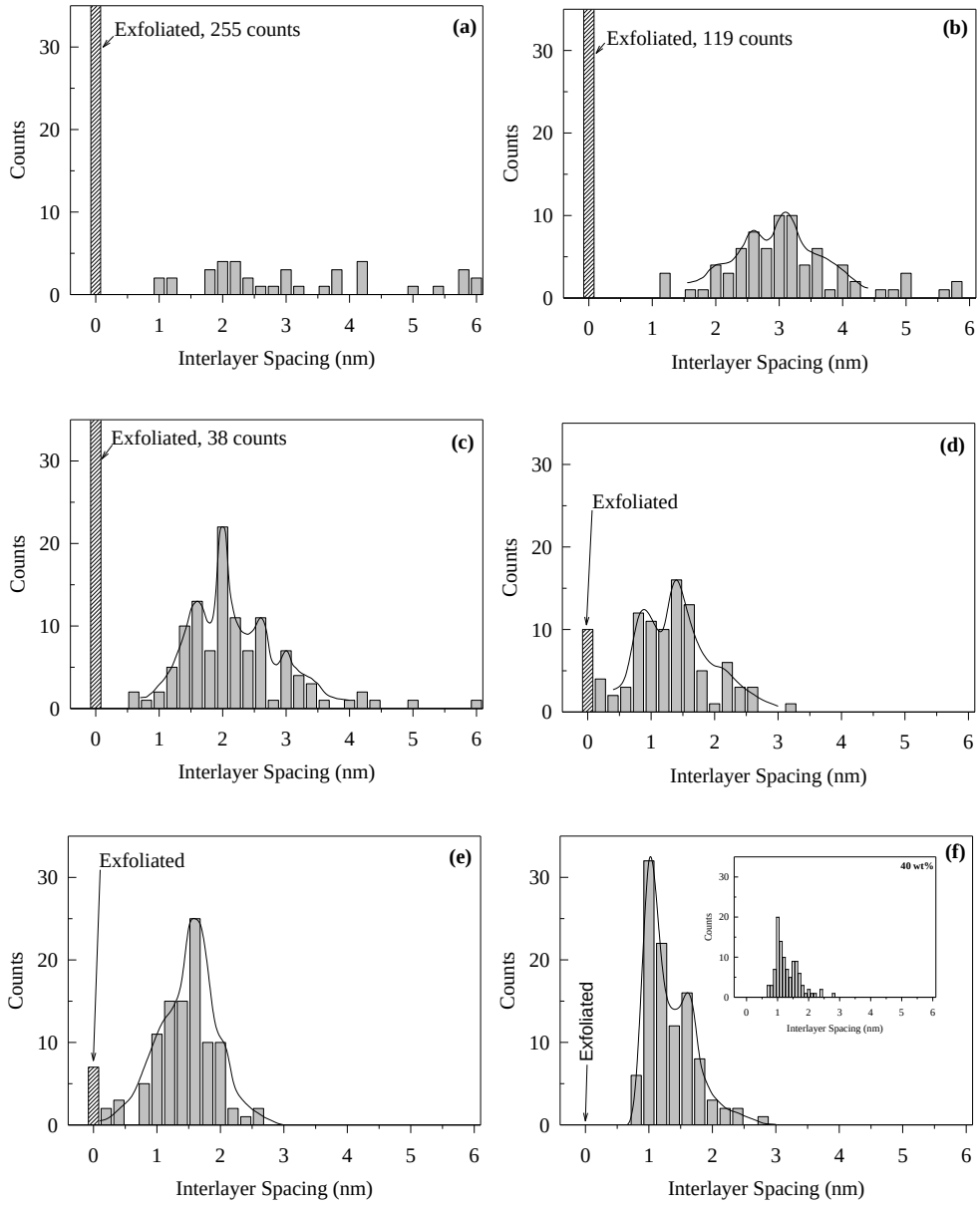

Figure 17. Histograms showing the extrapolated interlayer spacings and frequency of occurrence for individual clay stacks in the HBP4 nanocomposites analyzed. The following films were analyzed: (a) 1 wt% Na^{+}MMT, (b) 5 wt% Na^{+}MMT, (c) 15 wt% Na^{+}MMT, (d) 20wt% Na^{+}MMT, (e) 25 wt% Na^{+}MMT, (f) 40 wt% Na^{+}MMT. The hashed bar at 0 nm represents the population of exfoliated clay layers observed in the TEM micrographs. Curves have been aided to assist the reader.

The next set of histograms describes interlayer spacing as a function of mineral composition. These results are important when compared to the X-ray diffraction data reported in the early sections of this paper. An interlayer spacing increment of 0.2 nm was chosen for building these histograms. Distribution curves are added to assist the discussion. At 1% wt/wt Na^{+}MMT, exfoliation was the predominant state and a statistically insignificant number of intercalated layers were present that exhibited no distinct interlayer spacing behavior. In contrast, at 40%, the intercalated state was dominant, with no resolved exfoliated clay layers. This histogram indicates a bimodal distribution of interlayer spacings exhibiting two maxima, at about 1.0 nm and about 1.5 nm. To support this bimodal distribution the insert at 40% wt/wt is a histogram built using interlayer spacing steps of 0.1 nm. This bimodal interlayer spacing behavior as obtained via TEM analysis is in qualitative agreement with the results of XRD data obtained for this composition. The term qualitative is used here due to the fact that unlike the larger sample areas analyzed by XRD, for TEM analysis, the micrographs are images taken of very small sample cross-sectional areas, of about 6 square microns, and the microtomed sections themselves were on the order of 50μm x 50μm and sectioned from the centers of the nanocomposite films. However, based on the very small section size analyzed by TEM, it appears that factors exist, in addition to the formation of a concentration gradient in the film, that are responsible for the formation of multiple populations of interlayer spacings. In the early XRD section of this chapter it was stated that a statistical distribution of silicate layer coverage in the solution or upon solvent evaporation and layer restacking could be that factor.

Assuming that a statistical distribution of layer coverage exists, a question must be posed. What mechanism prevents the formation of intercalated stacks with mixed interlayer spacings? If intercalation leads freely to clay layers with random interlayer populations within a single tactoid, these mixed tactoids would result in a single, not bimodal, distribution of interlayer distances as calculated by using TEM analysis. The image analysis data suggests that there is a driving force for layers with the same level of HBP coverage to reaggregate preferentially. Perhaps the answer lies in considering that electrostatic interactions between positively charged sodium cations and negatively charged layers is the driving force for the stacks to be reformed upon solvent evaporation and the interaction is different in the case of charged silicate layers exhibiting different HBP coverage.

Continuing with the histograms of interlayer spacings obtained for different mineral compositions, at 25% wt/wt the corresponding histogram showed one main maximum situated at about 1.5 nm with two shoulders at about 1.0 nm and at about 2.0 nm. The interlayer spacing distribution was broadened as compared to the 40% wt/wt system. For the same composition XRD in fact showed one broader peak from which an interlayer spacing of 1.5 nm was calculated. At 20% wt/wt a very similar distribution of interlayer spacings was observed as in the case of 25% composition with the main maximum situated at about 1.5 nm in accord with the corresponding XRD observation. A smaller peak at 1.0 nm and a shoulder at 2.0 nm can also be seen. At 15% wt/wt we were able to differentiate one main maximum situated at 2.0 nm, two smaller maxima situated at about 1.5 nm and 2.5 nm, and a shoulder which most probably corresponds to a small peak situated at about 3.0 nm. The corresponding XRD showed a broader peak in accord

with the interlayer spacing 1.5 nm, but it is virtually impossible in this 2Θ range to differentiate peaks exhibiting 1.5 nm, 2.0 nm and 2.5 nm interlayer spacings as they overlap strongly. At 5%, despite the large presence of an exfoliated state, the distribution of interlayer spacings for the existing ordered tactoids can still be seen. Naturally, it was fairly difficult to interpret the interlayer spacings distribution at this lower mineral composition as the interlayer statistics were far from being perfect as compared to, for instance, the 40% wt/wt sample. The main maximum though can be seen as situated at about 3.0 nm, a smaller maximum perhaps can be claimed at 2.5 nm and two lesser defined shoulders resulting probably from small peaks situated at 2.0 nm and 3.5 nm can somewhat be resolved. It should be noted that the presence of 3.0 nm and 3.5 nm spacings seem to exceed the length of a diameter of 2.6 nm estimated elsewhere for the size of the fourth generation of a hydroxylated polyester dendrimer in a globular conformation [17]. This is in accordance with the small angle XRD data gathered in this regime as well as the 2^{nd} order reflections noted for the nanocomposites in region C of Figure 8.

The observed interlayer spacings observed from the interpretation of the TEM data provide additional evidence that the silicate sheets are not pillared by HBP in a globular (spherical) conformation. The intercalated interlayer spacing in HBP/clay nanocomposites appears to be dominated by a layer-by-layer deposition of flattened HBP molecules on the clay substrate. These final interlayer spacings can be larger or smaller than the diameter of the globular (spherical) conformation of the HBP. The observed step-wise changes in interlayer spacings must be due to the HBPs adopting a flattened conformation in the intercalated state.

Conclusions

The second and fourth generations of hydroxylated dendritic polyesters based on 2,2-bis-methylopropionic acid (bis-MPA) with an ethoxylated pentaerythritol (PP50) core were combined with unmodified sodium montmorillonite clay (Na^+MMT) using water as a solvent to generate a broad range of polymer clay nanocomposite films covering compositions from 0 to 100% wt/wt Na^+MMT. X-ray diffraction (XRD) and transmission electron microscopy (TEM) were used to investigate intercalation of these hyperbranched polymers (HBPs) into clay galleries. XRD was particularly revealing at larger mineral content and TEM at smaller mineral compositions. It was shown that the intercalated state was the predominant state in these nanocomposites. Exfoliation was dominant only within 0-5% wt/wt of mineral composition range. The fraction of exfoliated layers exponentially decreased in favor of an intercalated structure with increased clay content. By about 30% wt/wt only intercalated state was present. It was demonstrated that interlayer spacings changed within the composition range 5-95% wt/wt from 0.5 nm to up to 3.5 nm in a step-like fashion with 0.5 nm increments which corresponded to a flattened conformation of confined HBPs. Second and fourth generations exhibited virtually the same layer-by-layer intercalation of completely flattened HBPs. No dependence of interlayer spacings on generation number was found. Both XRD and TEM revealed the presence of several coexisting intercalated populations exhibiting different interlayer spacings in multiples of 0.5 nm. Only one intercalated population exhibiting intercalated spacing about 0.5 nm existed between 80 and 95% wt/wt. The number of observed coexisting intercalated populations increased with decreased mineral content. Two or more populations were observed at lower mineral compositions. Two factors were

considered to contribute to the observed multiple intercalated populations coexisting in nanocomposite films. A concentration gradient formed due to sedimentation of clay upon slow water evaporation, which would lead to different concentrations and resulting interlayer spacings and a statistical distribution of mineral layer coverage upon film formation. The presence of a concentration gradient was confirmed via XRD measurements of intact films accompanied by a predominant orientation of clay layers parallel to the film surface. TEM confirmed the presence of multiple intercalated populations even in microscopic regions of the nanocomposite films, which lead to the conclusion that a statistical distribution of mineral layer coverage existed even in regions of similar clay concentration.

References

[1] Seiler M. Dendritic polymers – interdisciplinary research and emerging applications from unique structural properties. Chem Eng Tech 2002; 25(3): 237-253.

[2] Jikei M, Kakimoto M. Hyperbranched polymers: a promising new class of materials. Prog Polym Sci 2001; 26: 1233-1285.

[3] Zhu PW, Zheng S, Simon G. Dielectric relaxations in a hyperbranched polyester with terminal hydroxyl groups: effects of generation number. Macromol Chem Phys 2001; 202: 3008-3017.

[4] Luciani A, Plummer CJG, Nguyen, T, Garamszegi L, Manson JE. Characterization of the commercial hyperbranched polyesters. Polym Sci Part B Polym Phys 2004; 42: 1218-1225.

[5] Žagar E, Žigon M. Local dynamics and hydrogen bonding in hyperbranched aliphatic polyesters. Macromolecules 2002; 35: 9913-9925.

[6] Žagar E, Huskić M, Žigon M. Structure-to-properties relationship of aliphatic hyperbranched polyesters. Macrom. Chem Phys 2007; 208: 1379-1387.

[7] Žagar E, Huskić M, Grdadolnik J, Žigon M, Zupančić-Valant A. Screening effects in solutions of a hyperbranched, dendrimer-like polyester. Macromolecules 2005; 38: 3933-3942.

[8] Žagar E, Žigon M, Podzimek S. Characterization of commercial aliphatic hyperbranched polyesters. Polymer 2006; 47: 166-175.

[9] Tanis I, Karatasos K. Glass transition in dendrimers. Macromolecules 2009; 42: 9581-9591.

[10] Malmström E, Johansson M, Hult A. Hyperbranched aliphatic polyesters. Macromolecules 1995; 28: 1698-1703.

[11] Burgath A, Sunder, A, Frey H. Role of cyclization in the synthesis of hyperbranched aliphatic polyesters. Macromol Chem Phys 2000; 201: 782-791.

[12] Malmström E, Hult A. Kinetics of formation of hyperbranched polyesters based on 2,2-bis(methylol)propionic acid. Macromolecules 1996; 29: 1222-1228.

[13] Magnusson H, Malmström E, Hult A. Hyperbranched Polymers. Macromolecules 2000; 33: 3099-3104.

[14] Zeiner T, Shrader P, Enders S, Browarzik D. Phase- and interfacial behavior of hyperbranched polymer solutions. J. Phase. Equilib. 2011; 302: 321-330.

[15] Plummer CJG, Gramszegi L, Leterrier Y, Rodlert M, Månson JE. Hyperbranched polymer layered silicates nanocomposites. Chem. Mater. 2002; 14: 486-488.

[16] Rodlert M, Plummer CJG, Grünbauer HJM, Månson, JE. Hyperbranched polymer/clay nanocomposites. Adv Eng Mater 2004; 6(9): 715-719.

[17] Rodlert M, Plummer CJG, Gramszegi L, Leterrier Y, Grunbauer HJM, Månson JE. Hyperbranched polymer/montmorillonite clay nanocomposites. Polymer 2004; 45: 949-960.

[18] Rodlert M, Plummer CJG, Leterrier Y, Månson JE. Rheological behavior of hyperbranched polymer montmorillonite clay nanocomposites J Rheol 2004; 48(5): 1049-1065.

[19] Alexandre M, Dubois P. Polymer-layered silicate nanocomposites: preparation, properties and uses of a new class of materials. Mater Sci Eng, R. 2000; 28: 1-63.

[20] Ray SS, Okamoto M. Polymer/layered silicate nanocomposites. Prog Polym Sci 2003; 28: 1539-1641.

[21] Peleshanko S, Tsukruk VV. The architectures and surface behavior of. highly branched molecules. Prog Polym Sci 2008; 33: 523-580.

[22] Tsukruk VV. Dendritic macromolecules at interfaces. Adv Mater 1998; 10(3): 253-257.

[23] Tjong SC. Structural and mechanical properties of polymer nanocomposites. Mater Sci Eng. 2006; 53: 73-197.

[24] Strawhecker KE, Manias E. Structure and properties of poly(vinyl alcohol)/na

[25] montmorillonite nanocomposites. Chem Mater 2000; 12: 2943-2949.

[26] Ecole Polytech, Rodlert M, Plummer CJG, Gramszegi L, Leterrier Y, Rodlert M, Månson JE. Composites and methods for their production. 2003; Patent: W003016392.

[27] Lagaly G, Ziesmer S. Colloid chemistry of clay minerals: the coagulation of montmorillonite dispersions. Adv Colloid Interface Sci 2002; 100-102: 105-128.

[28] Carmezini G, Mackay ME, Sauer BB, Kampert W. Manipulation of hyperbranched polymers' conformation. Chem Mater 2002; 14: 819-825.

[29] Liau W, Boyd RH. Structure and packing in crystalline aliphatic polyesters. Macromolecules 1990; 23: 1531-1539.

[30] Mansfield ML. Surface adsorption of model dendrimers. Polymer 1996; 37(17): 3835-3841.

[31] Ratner M, Neelov I, Sundholm, F, Grinyov B. Adsorption behavior of dendritic polymers. Funct Mater 2003; 10(2): 273-275.

[32] Bliznyuk VN, Rinderspacher F, Tsukruk VV. Dendritic macromolecules at interfaces. Polymer 1998; 39(21): 5249-5252.

[33] Tsukruk VV, Rinderspacher F, Bliznyuk VN. Multilayered assembly of PAMAM dendrimers. Langmuir 1997; 13(8): 2171-2176.

[34] Hierlemann A, Campbell JK, Baker LA, Crooks RM, Ricco AJ. Structural distortion of dendrimers on gold surfaces: a tapping-mode AFM investigation. J Am Chem Soc. 1998; 120: 5323-5324.

[35] Li J, Piehler LT, Qin D, Baker JR, Tomalia DA. Dendrimers for Nanoparticle Synthesis and Dispersion. Langmuir 2000; 16: 5613-5616.

[36] Singh MS, Sood R, Kaur G, Sakai K, Yoshimura T, Esumi K. Characterization of aliphatic and aromatic polyester hyperbranched dendrimers by AFM imaging. Colloid Polym Sci 2005; 284: 74-79.

[37] Vaia RA, Liu W. J. X-ray powder diffraction of polymer/layered silicate nanocomposites. Polym Sci Polym Phys 2002; 40: 1590-1600.

CHAPTER IV

ANALYSIS OF THE RIGID AND MOBILE AMORPHOUS FRACTIONS OF INTERCALATED HYDROXYLATED DENDRITIC POLYESTER/CLAY NANOCOMPOSITES PREPARED FROM AQUEOUS SOLUTION BY DIFFERENTIAL SCANNING CALORIMETRY AND POSITRON ANNIHILATION LIFETIME SPECTROSCOPY

This chapter was co-authored by Jeremy J. Decker, James Goetz, Brian Olson, Alexander M Jamieson, and Sergei Nazarenko

Abstract

The fourth generation of a water soluble hydroxylated dendritic polyester was combined with sodium montmorillonite clay using water to generate a broad range of polymer clay nanocomposites covering compositions from 0 to 100% wt/wt Na^{+}MMT. X-ray diffraction indicated intercalation was the dominant state and interlayer spacings changed in 0.5 nm increments, corresponding to a flattened conformation of the confined HBPs. Differential scanning calorimetry showed changes in heat capacity, ΔC_p, at T_g with clay content attributed to the formation of a rigid amorphous fraction (RAF). The fractions of RAF were quantified from the changes in heat capacity with clay content, and the trends of RAF formation were verified by ortho positronium temperature scans, using positron annihilation lifetime spectroscopy, which tracked changes in thermal expansivity of the nanocomposites with clay content. The observed interlayer spacings correlated in a manner quantifiable with the changes in heat capacity. RAF was found to remain vitrified at elevated temperatures.

Introduction

Polymer clay nanocomposites have received significant attention in recent decades because they often exhibit chemical and physical properties that differ from those of conventional composite materials [1-3]. Due to their inherent hydrophilicity, layered silicates such as sodium montmorillonite (Na^+MMT) are incompatible with most polymers. In order to promote dispersion in a polymer matrix, layered silicates typically require modification by surfactants which increase the organophilicity of the clay surfaces. Once prepared, the morphology of nanocomposites can generally be classified as phase separated, intercalated, disordered intercalated, and exfoliated. The existence of these morphologies is dependent upon the interactions between the nanoclay and polymer and the processing conditions [1-3]. Intercalated nanocomposites occur due to the insertion of the polymer between individual silicate layers. These structures occur in a regular fashion with crystallographic dimensions. Hydroxylated edge-to-edge interactions between the clay tactoids can also lead to the formation of flocculated nanocomposites, which maintain their intercalated character with increased lateral dimensions. Individual clay layers can also be separated in the polymer matrix, which is indicative of an exfoliated morphology. Generally, exfoliated nanocomposites are seen to occur at much lower clay loadings than intercalated nanocomposites. It is, however, quite common to see a mixture of these morphologies in polymer/clay nanocomposites [1]. One such example is when the intercalated clay layers are stacked, but the layers are not parallel, which can be classified as a disordered-intercalated state.

Water-soluble linear polymers, such as PEO, PVA, and PVP, have successfully been intercalated into unmodified clay galleries by melt processing and solution casting

methodologies [1-2]. Solution cast nanocomposites can be prepared with linear hydrophilic polymers and Na^{+}MMT; however, the high processing viscosities in these systems can require shear intensive processing procedures, especially at high clay contents [4]. Hyperbranched polymers possess lower solution viscosities than conventional linear polymers, due to their globular structures, which allow fewer entanglements in solution [5]. These lower solution viscosities allow for the solution processing of nanocomposites, even at high clay concentrations, that do not require such shear intensive procedures.

Perhaps due to their ease of accessibility, dendritic hyperbranched polyester polyols based on 2,2-bis-methylopropionic acid (bis-MPA) with an ethoxylated pentaerythritol (PP50, Perstorp) core became a popular model system for a number of studies that investigated their chemical structure and physical properties [6-12]. The pseudo-one-step, divergent synthesis of these aliphatic-ester dendritic polymers was first described in 1995 [13]. The synthesis of these hyperbranched polymers (HBPs) involves the sequential addition of monomer and has been investigated in a number of publications [14-16]. These polymeric structures preserve the essential features of dendrimers, namely high end-group functionality and a globular architecture, but possess imperfect branching and large polydispersities [5]. Relevant to the current publication, these HBPs are water soluble due to the presence of branch-terminal hydroxylated end groups [17].

The adsorption behavior of dendritic polymers on a substrate has been predominantly investigated using surface techniques such as AFM and ellipsometry. It has been found that a high interaction strength between the end functional groups of dendritic polymers and a substrate leads to the collapse of the globular structure of the

dendritic polymer. This attraction can lead to significant flattening of the globular structures, including the formation of flattened monolayer structures on suitable substrates [18-22]. Molecular dynamics simulations have predicted that substantial flattening of dendrimers, from an otherwise globular state, is dependent upon the interaction strengths between the dendritic polymer and substrate [23].

Another useful method to investigate the adsorption of polymers on substrates is through the generation of polymer-clay nanocomposites. The incorporation of polymer into clay stacks introduces numerous substrates into the polymer matrix and these interactions can be probed by bulk techniques. One such study was conducted with the aforementioned hyperbranched polyester polyols by Månson's group and was followed by a series of papers exploring the behavior of these nanocomposites for the second, third, and fourth pseudogenerations of HBPs [24-27]. In these studies, HBP/clay nanocomposites were prepared via an aqueous solution intercalation method, utilizing unmodified Na^{+}MMT to produce nanocomposite films. In these studies, X-ray diffraction (XRD) data was used to conclude that at intermediate Na^{+}MMT contents, the interlayer spacings of the intercalated nanocomposites correlated closely with estimates of the molecular diameters for the different generations of HBPs employed. It was concluded that the HBPs maintained their globular architecture in an intercalated state throughout about half of the compositional range. However, it was proposed that at the larger clay contents, the HBPs began to flatten within the clay stacks. This flattening behavior, in the highest clay content regimes, lead to equivalent interlayer spacings for the second, third, and fourth generations of the hyperbranched polymers.

These results led us to investigate the morphology of these nanocomposites in greater detail in order to better understand how the constraints imposed by the clay layers affected the conformational state of these dendritic polymers. We investigated nanocomposites comprised of the second and fourth pseudogenerations of the same hydroxylated dendritic polyesters combined with unmodified Na^+MMT, utilizing water as the solvent [28]. A broader range of polymer clay nanocomposite films covering compositions from 0 to 100% wt/wt Na^+MMT were prepared from both generations of HBP. XRD and transmission electron microscopy (TEM) were used to investigate the intercalation state of these hyperbranched polymers in the clay galleries. Intercalation peaks were observed by powdered XRD at and above 15% wt/wt Na^+MMT content for both HBP systems. Intercalation was present at all clay loadings, as evidenced by TEM, but at the lower clay content regimes exfoliated and disordered intercalated states were also present. As the nanocomposite clay content increased, so too did the number of clay layers per intercalated stack. From the d-spacing information obtained by XRD, the structural characteristics of the HBPs in confinement were explored. The observed interlayer spacings for the 2^{nd} and 4^{th} pseudogenerations of HBP were observed to change in discrete increments of ~0.5 nm as the clay content of the nanocomposites varied.

Importantly, it was observed that the interlayer spacings for the second and fourth generations of HBP were nearly identical at the same clay compositions, which indicated that the interlayer spacings were independent of the HPB generation number (molecular weight). In addition, the interlayer spacings for both HBP2 and HBP4 decreased with increasing clay content in ~0.5 nm increments until finally reaching a minimum spacing of ~0.5 nm at the highest clay contents. The changes in interlayer spacings occurred in

0.5 nm steps which were consistent with the existence of discrete layers of flattened HBP between the clay layers. It was proposed that the HBP adsorbed onto the clay layers in solution, with the re-aggregation of the coated clay layers leading to intercalation as the water evaporated during film formation. These hyperbranched polyester nanocomposites were composed of only sodium montmorillonite clay and hyperbranched polyester and provided a simple two component system with which to investigate the effects of HBP adsorption and nanoconfinement. The structural collapse and confinement of the HBP by the clay layers, was expected to result in the formation of a rigid amorphous fraction within the HBP4, which could be investigated by bulk techniques.

The concept of the rigid amorphous fraction (RAF) was introduced to explain the vivid deviation from one-to-one correspondence between crystallinity and the observed change in heat capacity, ΔC_p , in the glass transition, T_g, interval for semicrystalline polymers [29]. In the simplest terms, the RAF represents the fraction of amorphous phase that does not contribute to the change in heat capacity. It is believed that this phase is due to immobilization of the polymer chains by interfaces and has been investigated in semicrystalline polymers for many years, where the interfaces form due to polymer crystallinity [29-32]. More recently, there have been investigations into the formation of the rigid amorphous phase in nanocomposite systems where inorganic fillers have also lead to the immobilization of the amorphous polymer [33-36]. In these papers the rigid amorphous fraction was attributed to the interfacial interactions of the inorganic fillers with the polymer matrices. Currently, there is no evidence that the rigid amorphous fraction undergoes devitrification in nanocomposite systems since, unlike polymer crystals, the inorganic particles do not melt within the thermal stability range of the

polymers. This means that the interactions between the polymer and inorganic substrate are maintained at elevated temperatures and prevent the devitrification of the immobilized fraction [33]. Indeed this was recently demonstrated in a nanocomposites study of the dynamics of an amorphous hyperbranched polyesteramide intercalated in Na^+MMT layers investigated by quasi elastic-neutron scattering. In this study, it was observed that the polymer chains confined within the clay galleries exhibited behavior similar to that of the bulk polymer below the glass transition temperature, but above this T_g the HBP dynamics were frozen due to the clay nanoconfinement, which was supported by observed decreases in ΔC_p at T_g with clay content [37].

In the current paper we report heat capacity measurements from differential scanning calorimetry (DSC) and free volume measurements from positron annihilation lifetime spectroscopy (PALS) for the previously studied nanocomposite systems prepared from the fourth pseudogeneration of hydroxylated dendritic polyesters and Na^+MMT [28]. Heat capacity measurements were used to quantify the immobilized interfacial fraction of the polymer (RAF) as described by Wunderlich [29]. Since the Na^+MMT underwent no thermal transitions within the investigated temperature ranges, it proved ideal for an investigation of the polymer immobilization at the clay interfaces. These nanocomposites had been previously generated over a large range of clay compositions and the nanocomposite morphology investigated by X-ray diffraction techniques and transmission electron microscopy (TEM). It was, therefore, possible to correlate the observed interlayer spacings of the intercalated clay with RAF formation at the various clay contents investigated.

Positron annihilation lifetime spectroscopy (PALS) is a useful technique used to probe structural disorder in polymers [38]. In particular, quantitative comparisons have been established between the characteristic parameters, intensity, I_3, and lifetime, τ_3, of the orthopositronium (o-Ps) annihilation component of PALS and the fractional free volume f_v of amorphous polymers, as computed by statistical mechanical theory [39,40]. The o-Ps intensity, I_3, is regarded as a measure of the density of the free volume holes. The o-Ps lifetime, τ_3, can be related to the hole radius R and hence to the hole volume $\langle v_f \rangle = (4\pi/3)R^3$. Thus, $f_v = CI_3v_f$, where C is a constant which must be established for each polymer. Approaches have also been developed to correlate the o-Ps lifetimes with fractional free volume without the use of I_3 data [41-44]. If the HBP confined within the clay galleries exhibits glassy behavior at temperatures above the bulk T_g, then this should be evidenced by changes in τ_3 with temperature, as the free volume temperature coefficients of the glassy and liquid phases are different. Since the RAF portion of the system is expected to remain vitrified above T_g, this should lead to a decrease in the temperature coefficient of τ_3 above T_g, relative to the virgin HBP, caused by the additive contributions of both the glassy and liquid coefficients to the thermal expansion of the nanocomposite systems. The effects of confinement, as characterized by both thermal and free volume techniques, will provide valuable insight into the effect of clay intercalation on the hyperbranched polymer in these nanocomposite systems.

Experimental

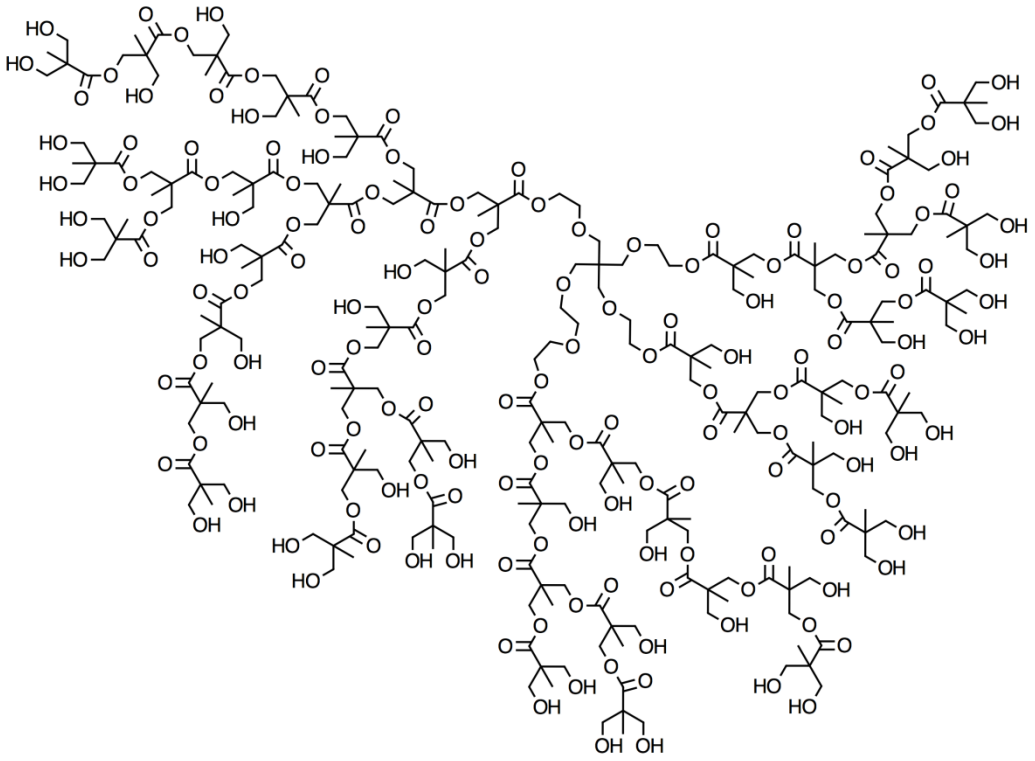

Figure 18. Structure of HBP4 accounting for imperfect branching.

Sodium montmorillonite clay (Na-MMT) Cloisite® with a cation exchange capacity (CEC) of 92.6 meq/100 g was purchased from Southern Clay Products. As received clay powder was sifted through a 75 micron sieve, dried at 150°C under vacuum overnight, and stored over desiccant prior to use. The hydroxyl-functional dendritic (hyperbranched) polyester, Boltorn™ H40 (HBP4), was obtained from Perstorp Specialty Chemicals AB, Sweden, in the form of pellets. A schematic representation of the hyperbranched structure of HBP4 is shown in Figure 18.

The nanocomposites utilized in this study were created via a solution-intercalation method and were from the same batches investigated previously [28]. The required amount of Na^{+}MMT clay was first dispersed in deionized water at 50°C and stirred for at

least 8 hours to optimize clay delamination. The aqueous concentration of clay was kept below 1% (wt/wt) in order to ensure that individual clay layers were well dispersed. When sufficiently diluted, Na^{+}MMT particles are known to delaminate into single layers [45].

The required amount of Boltorn™ polyol was dissolved in boiling DI water. The concentration of polymer in water was kept at or below 10% (wt/wt), as this concentration was observed to effectively disperse and dissolve the HBP4. This solution was then quantitatively transferred into the clay dispersion. This combined solution was rapidly stirred in open air at 50°C until the dispersion approached the level of the stir bar but remained in a liquid state. It was then transferred to Teflon trays and dried for two days in a convection oven at 50°C. Two further days of drying followed, under vacuum, at 120°C. This temperature was demonstrated as optimal for removing water from Boltorn™ polyols [46]. The resulting nanocomposite films were stored over desiccant at room temperature.

One dimensional X-ray diffraction spectra were collected on a Rigaku Ultima III diffractometer (Cu Kα radiation, λ = 1.542Å) at room temperature using Bragg-Brentano parafocusing geometry (reflection mode XRD). XRD information was obtained from samples that were powdered in an analytical mill. The use of powdered samples ensured that the Debye-Sherrer diffraction rings were distributed evenly, thus eliminating any orientational effects of the HBP and silicate layers in the nanocomposite. These powdered samples also ensured an accurate representation of the entire bulk sample by XRD, and was the most accurate method for obtaining representative d-spacing behavior for the nanocomposite structures by this technique. In all cases, samples were analyzed

immediately after removal from the dessicator to reduce water uptake. For optimal consistency, the angular positions of peaks were resolved using the peak search algorithm of MDI Jade 7©.

For transmission electron microscopy (TEM) the nanocomposite films were embedded in epoxy resin and then trimmed so that the centers of the films could be microtomed. About 90 nm thick sections were cut at T = -30°C in the direction perpendicular to the film surface using a Leica cryo-ultramicrotome FC6 equipped with freshly cut glass knives. These sections were imaged using a Zeiss 109T TEM operated at 80 kV under bright field conditions. Since the silicate layers possess a higher electron density than the surrounding HBP matrix, they appear darker in the images. Image analysis of the intercalated samples was carried out using UTHSCSA Image Tool version 3.00.

Glass transition behavior was determined using a TA instruments Q2000 Differential Scanning Calorimeter. Heating and cooling scans were carried out at 10°C/min over a range of -50 to 150°C under a dry nitrogen atmosphere. Second heating scans were utilized for the analysis to eliminate any physical ageing effects. The glass transition temperature, T_g, and heat capacity change, ΔC_p, at T_g were determined according to established methodology [47,48]. The positron annihilation lifetime spectroscopy (PALS) experiments were conducted with a fast-fast coincidence system, as described in previous work, having a time resolution of 220 ps [49-51]. From each sample film, pieces were cut, each with a 1 x 1 cm^2 area. On each side of a 30 μCi ^{22}Na positron source, pieces of the sample films were stacked to a total thickness of 1 mm. The sample cell was kept under vacuum during the experiments. All measurements were

taken over an hour, for a total of 1 x 10^6 counts in each PALS spectrum. Temperature measurements were taken by first decreasing the temperature to -30°C then waiting for an hour to allow for equilibrium before beginning the experiment. The temperature was then sequentially increased in 10°C steps, collecting a spectrum each step, after waiting 10 min to allow for equilibration. Three temperature scans were averaged for each sample, with no differences detected in the PALS parameters between the heating cycles. The PALS spectra were tested against three and four component fits using the PATFIT 88 software package [52]. Optimal fits were obtained to three components with variances smaller than 1.1.

Results and Discussion

Intercalation Behavior Probed by XRD and TEM

Nanocomposite specimens of Na^+MMT in HBP4 were prepared with clay contents ranging from 0-95% wt/wt Na^+MMT. The morphological properties of these nanocomposites were thoroughly documented in a previous paper, utilizing various XRD techniques and TEM [28]. Intercalation related XRD peaks originate from a constructive interference of the X-ray beam diffracted from a set of parallel silicate layers constituting an ordered clay tactoid. Using Bragg's law the d-spacings can be calculated. The interlayer spacing, l, subsequently can be calculated by subtracting the crystalline silicate sheet thickness (0.96 nm, as determined from XRD analysis of dried Na^+MMT) from the d-spacing. The interlayer spacings, as determined from the observed first and second order diffraction peaks, are shown as a function of the weight fraction Na^+MMT (w_{MMT}) in Figure 19. The second order diffraction peaks often allowed us to elucidate the presence of multiple interlayer spacings even more accurately since these peaks were

angularly much better resolved, and exhibited less overlap, than the corresponding first order peaks. The powdered nanocomposite diffractograms for nanocomposites below 15 wt% showed no clear diffraction peaks, indicative of a transition from an ordered intercalated structure at larger clay concentrations to a less ordered intercalated structure followed by partial and perhaps eventual, complete clay exfoliation at progressively smaller clay concentrations. The XRD data from powdered samples is utilized in this discussion since it ensured an accurate representation of the bulk clay morphology and eliminated orientational effects that occurred during film formation.

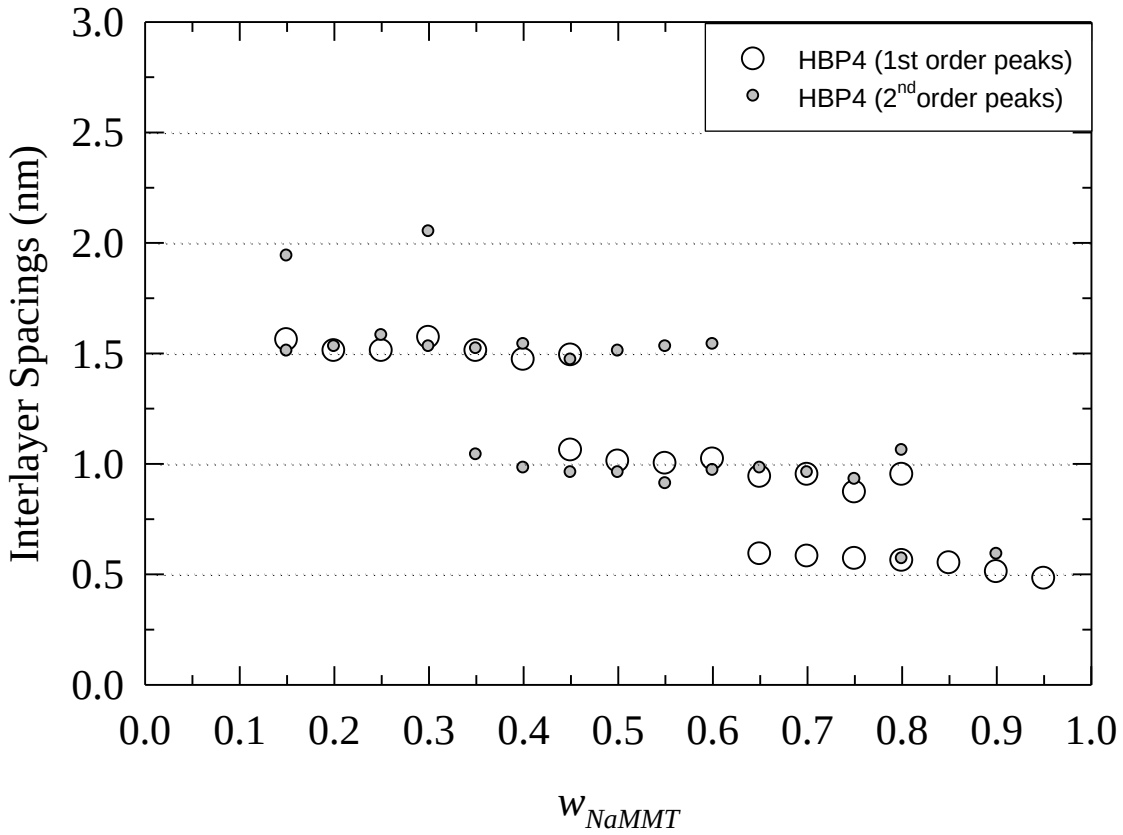

Figure 19. Interlayer spacing behavior observed in powdered HBP4 nanocomposites as a function of weight fraction Na^{+}MMT. Open and filled circles are the interlayer spacings calculated using the first and second order diffraction peaks, respectively, for the nanocomposite systems.

Probing the amorphous phase in HBP4 nanocomposites by DSC

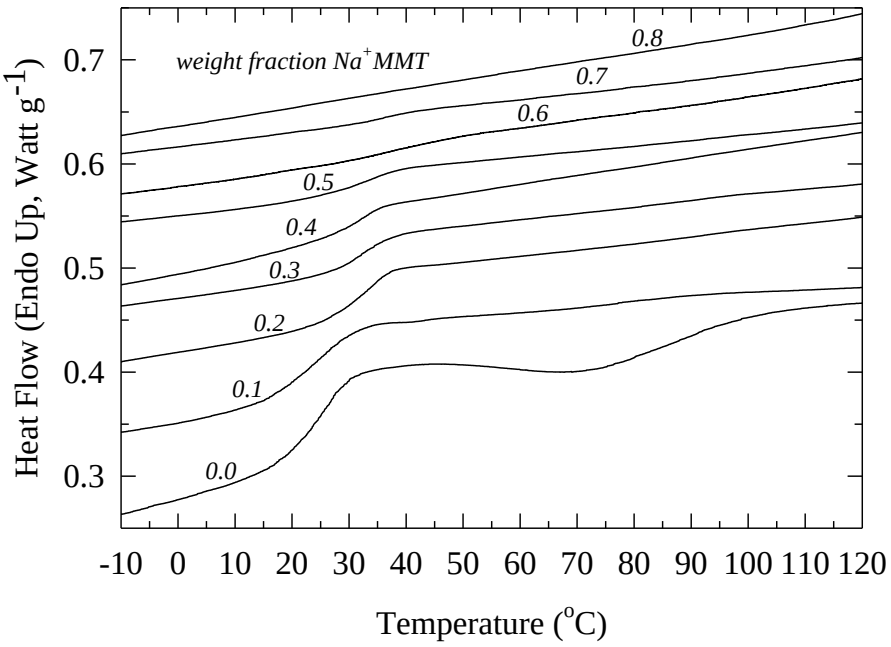

Figure 20. DSC thermograms of nanocomposites prepared from HBP4 labeled in terms of weight fraction Na^+MMT. Curves offset to aid the viewer.

Differential scanning calorimetry was used to analyze the glass transition behavior of the HBP4 with Na^+MMT nanocomposites prepared from clay loadings from 0 to 95% wt/wt Na^+MMT. The glass transition temperatures, T_g, of the nanocomposites and the changes in heat capacity, ΔC_p, at T_g were determined. Numerous discrete DSC measurements were made from each of the samples and error is reported as the standard deviation. The nanocomposites were taken directly from the dessicator and placed into sealed aluminum pans to prevent water uptake. Representative thermal scans of the nanocomposite systems are included in Figure 20.

The second heating scans were utilized to eliminate thermal history. Second and third heating scans were self consistent. The heat capacity change, ΔC_p, at T_g, was determined according to the methodology proposed elsewhere [47,48]. The glass transition temperature, T_g, was taken as the point when half of the polymer is devitrified

as determined from the heat capacity increase, where a line drawn median to the heat capacity lines for the glass and liquid behavior intersects the DSC curve. The observed glass transitions and the changes in heat capacity at T_g are included in Table 4.

Table 4

Glass Transition Temperatures (T_g) and Changes in Heat Capacity at T_g with Na^+MMT Content

Weight fraction Na^+MMT (w_{NaMMT})	Volume fraction Na^+MMT (φ_{NaMMT})	Glass transition temperature ± std deviation (T_g)	Heat capacity jump at T_g ± std deviation (ΔCp)
0.00	0.000	24.2 ± 1.2	0.497 ± 0.038
0.05	0.023	23.6 ± 1.2	0.453 ± 0.032
0.10	0.048	24.7 ± 0.5	0.391 ± 0.036
0.15	0.075	29.2 ± 1.2	0.342 ± 0.006
0.20	0.102	31.4 ± 1.0	0.294 ± 0.023
0.25	0.132	30.4 ± 0.7	0.252 ± 0.025
0.30	0.164	31.7 ± 1.2	0.203 ± 0.011
0.35	0.197	31.7 ± 0.7	0.193 ± 0.023
0.40	0.233	30.7 ± 0.6	0.158 ± 0.035
0.45	0.272	32.3 ± 1.6	0.110 ± 0.030
0.50	0.313	29.2 ± 1.4	0.134 ± 0.036
0.55	0.358	30.4 ± 1.1	0.105 ± 0.020
0.60	0.406	37.8 ± 2.8	0.077 ± 0.008
0.65	0.459	35.0 ± 1.4	0.027 ± 0.007
0.70	0.516	36.0 ± 0.8	0.040 ± 0.015
0.75	0.578	36.3 ± 2.3	0.014 ± 0.006
0.80	0.646	NA	0.000 ± 0.000

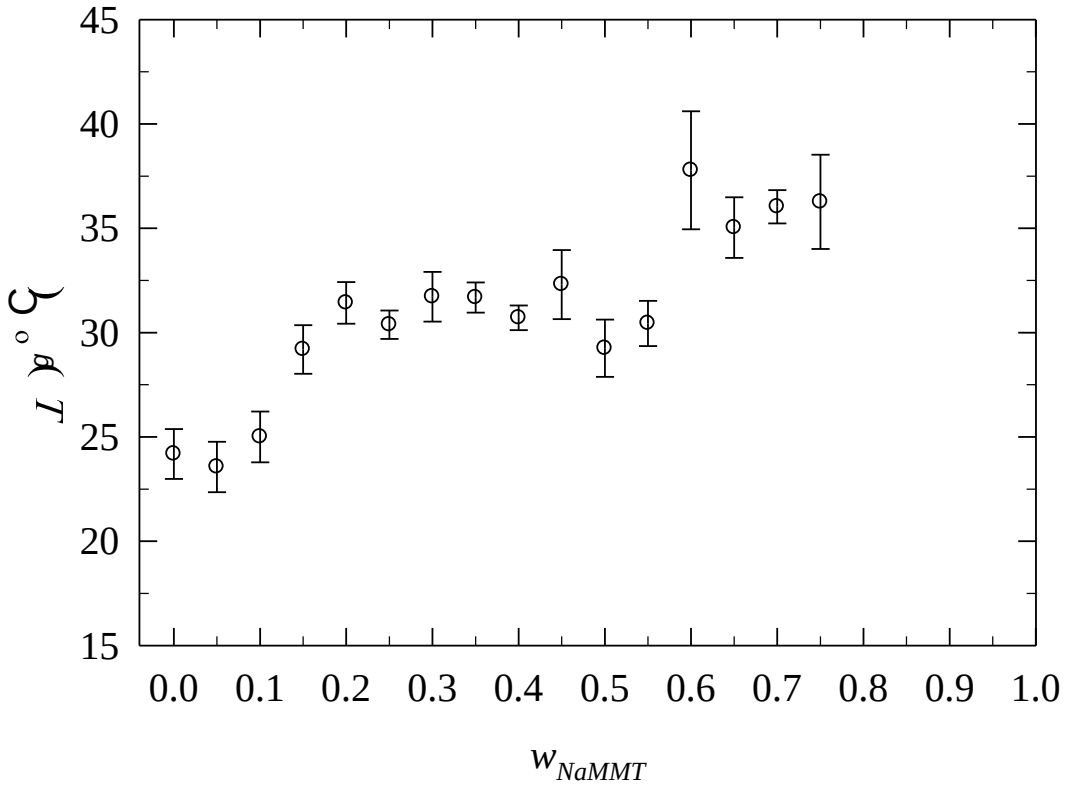

Figure 21. Glass transition temperature with weight fraction Na^+MMT for HBP4 nanocomposites.

The changes in T_g with clay content are shown in Figure 21. The glass transition temperatures of the nanocomposites remained near 24˚C until it sharply increased at 15% wt/wt Na^+MMT towards a relative plateau region at about 31˚C. The T_g remains around 31˚C up to 55 wt% Na^+MMT. From 60-75% wt/wt Na^+MMT, the T_g increased to 36˚C. At and above 80 wt% Na^+MMT, no T_g was detected.

The flattened conformations of the intercalated HBP4, as evidenced by XRD, indicate a strong interaction between the clay surface and the HBP. This suggested that the abrupt changes observed in the glass transition temperatures likely correlated with the clay morphology. Indeed, at 15% wt/wt Na^+MMT, powdered samples analyzed by XRD showed a clear diffraction pattern which was not present at either 5 or 10% by the same methodology. As seen in the TEM micrographs of Figure 22, at 15% wt/wt Na^+MMT the

clay has transitioned from discrete exfoliated layers and tactoids to a flocculated morphology. With additional clay content, this flocculation grows more pronounced and the connected clay tactoids form a network structure within the nanocomposite.

This increase in the glass transition clearly corresponded to the observed onset of the flocculated clay network, which must have influenced the significant hydrogen bonding network of the HBP4, which has been thoroughly investigated [53,54]. The hydrogen bonding network of the HBP4 is typically strong enough to prevent dissolution in solvent without thermal pretreatment [55]. The exotherm visible at ~70˚C in Figure 20, for the pure HBP is attributed to the formation of H-bonds between hydroxyl groups, and is followed by an endotherm that is attributed to the cleavage of these H-bonds [10]. Both the exotherm and endotherm rapidly decreased with clay content until they were completely undetectable above 20% wt/wt Na^+MMT. As the flocculated clay network surrounded the free polymer, its influence on the hydrogen bonding effect was clearly pronounced. Once this network structure had developed, the available surface area between the clay and the free HBP4 was maximized, which explained the leveling off of the observed glass transitions and the suppression of the hydrogen bond rearrangements by DSC. At the high clay content regime of 60-75% wt/wt Na^+MMT the volume fraction of the clay and intercalated polymer is high and the remaining free polymer may have been reduced to a very small scale between the intercalated regions, which could have lead to the final observed increase in the glass transition [56]. At 80wt% MMT and above, there was no measurable glass transition, indicating that the entire HBP4 polymer was restricted due to the presence of the clay layers.

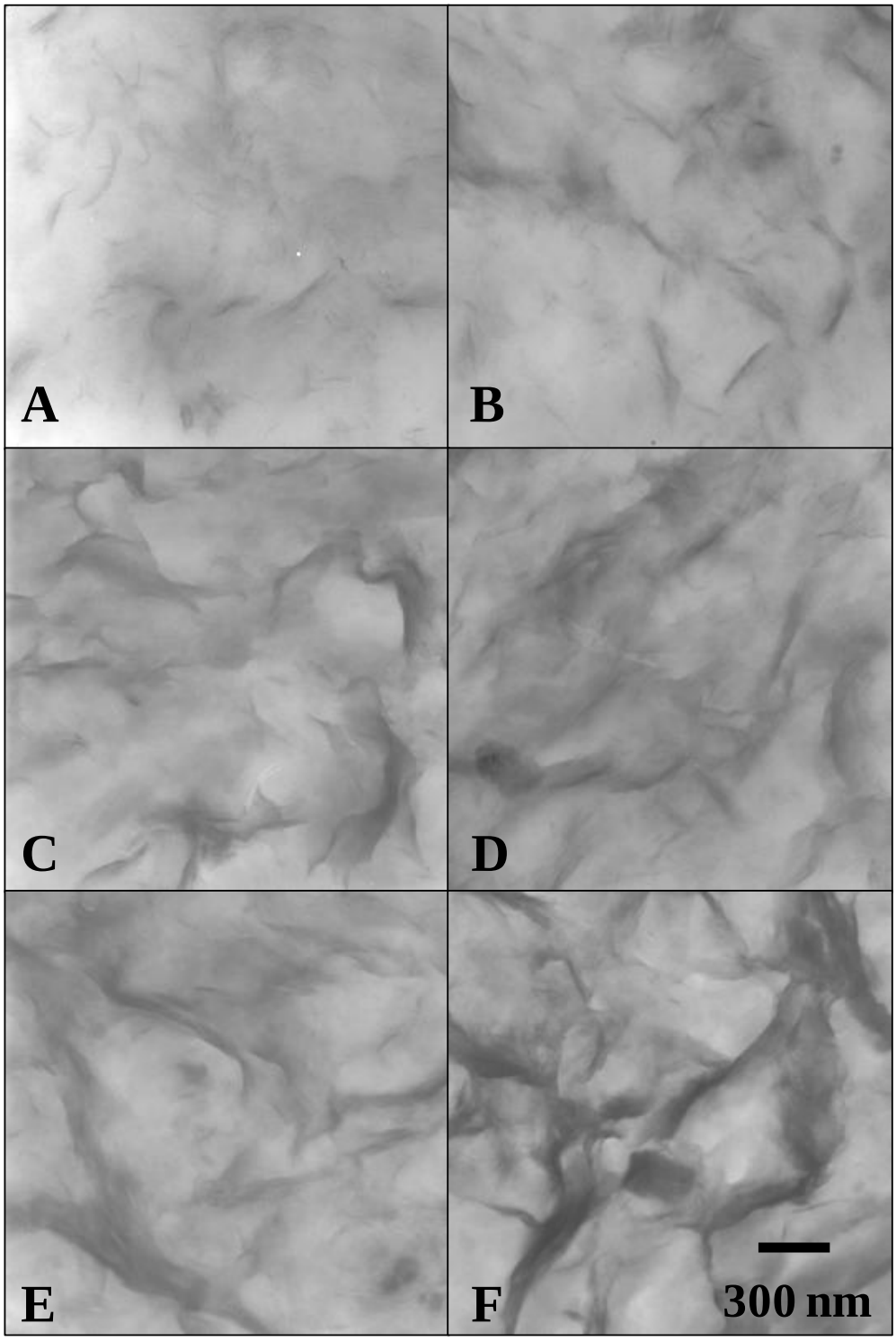

Figure 22. Representative TEM micrographs of HBP4/Na^{+}MMT nanocomposites with (A) 1, (B) 5, (C) 15, (D) 20, (E) 25, and (F) 40% wt/wt clay content.

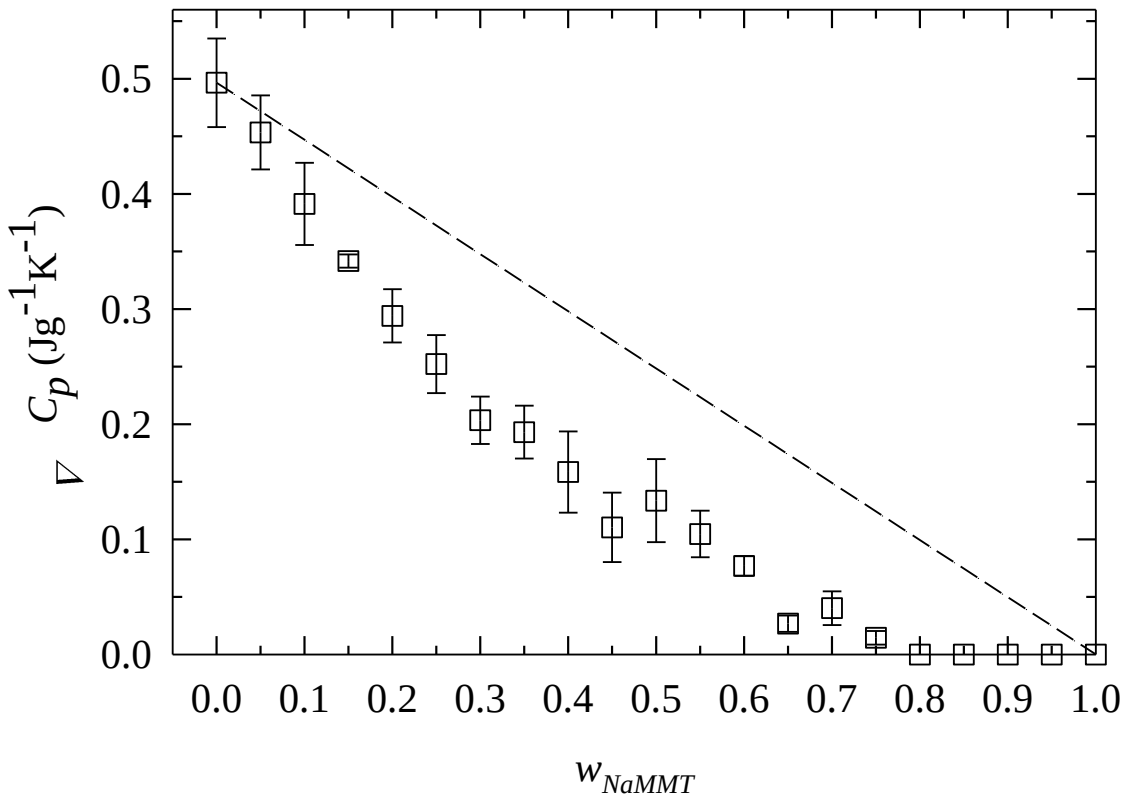

Figure 23. Heat capacity change ΔC_p at T_g for HBP4 nanocomposites as a function of weight montmorillonite fraction. Dashed line represents the standard two-phase model predictions.

Figure 23 shows heat capacity changes, ΔC_p, at T_g for the HBP4 nanocomposites as a function of weight fraction montmorillonite. The heat capacity change at T_g is an attribute of the mobile amorphous fraction (MAF) of HBP4 [29]. Since montmorillonite undergoes no thermal transitions over the studied temperature range, it does not contribute to the heat capacity jump at T_g. Assuming only the MAF and Na^+MMT to be present, the ΔC_p trend can be expected to decrease linearly with clay content, as depicted by the dashed line in Figure 23. However, the ΔC_p trend deviated significantly from this linear trend. The deviation in observed heat capacities from the two-phase prediction grew in significance as the clay content increased, until the glass transition was fully suppressed at w_{MMT} of 0.80. The suppression of the glass transition was attributed to the

formation of a rigid amorphous fraction (RAF) and the observed changes in ΔC_p at T_g were used to calculate the amount of RAF by the following relationship [29,57,58]:

$$w_{RAF} = 1 - w_{NaMMT} - \frac{\Delta C_p}{\Delta C_p^a} \quad (1)$$

Here, ΔC_p is the observed change in heat capacity at T_g, $\Delta C_p{}^a$ is the heat capacity change for the amorphous HBP4, and w_{NaMMT} is the weight fraction of Na^+MMT. The ratio $\Delta C_p / \Delta C_p{}^a$ is equivalent to the weight fraction of the mobile amorphous fraction (w_{MAF}), which contributes to the glass transition.

As detailed in the previous publication, no changes in density of the amorphous HBP4 were observed in the nanocomposites [28]. Since no HBP4 densification occurred, the densities of the MAF, ρ_{MAF}, and the RAF, ρ_{RAF}, were equivalent with a value of 1.306 g/cm^3. The density of the Na^+MMT, ρ_{MMT}, has been established as 2.86 g/cm^3.

Based upon the measurements of ΔC_p at T_g, the weight fraction of MAF, w_{MAF}, and RAF, w_{RAF}, were calculated and are plotted as a function of w_{NaMMT} in Figure 24. The fraction of MAF was seen to decrease with clay content until it reached zero at w_{NaMMT} of 0.80, where the glass transition was undetectable. This complete suppression of the glass transition was reasonable if one considered the system in terms of a hybridized structure. The component volume fractions for an ideal hybrid nanocomposite structure based upon the observed 0.5 nm interlayer spacings were calculated using the known component densities. Perfectly alternating layers of flattened HBP with a thickness of 0.5 nm, sandwiched within the silicate layers that are 0.96 nm thick, would exist at 81% wt/wt Na^+MMT (66% vol/vol). It was clear that this corresponded to the observed suppression of the glass transition at 80 wt% NaMMT since at and above this composition, the HBP

was fully incorporated into the clay tactoids, which left no free MAF to undergo the glass transition.

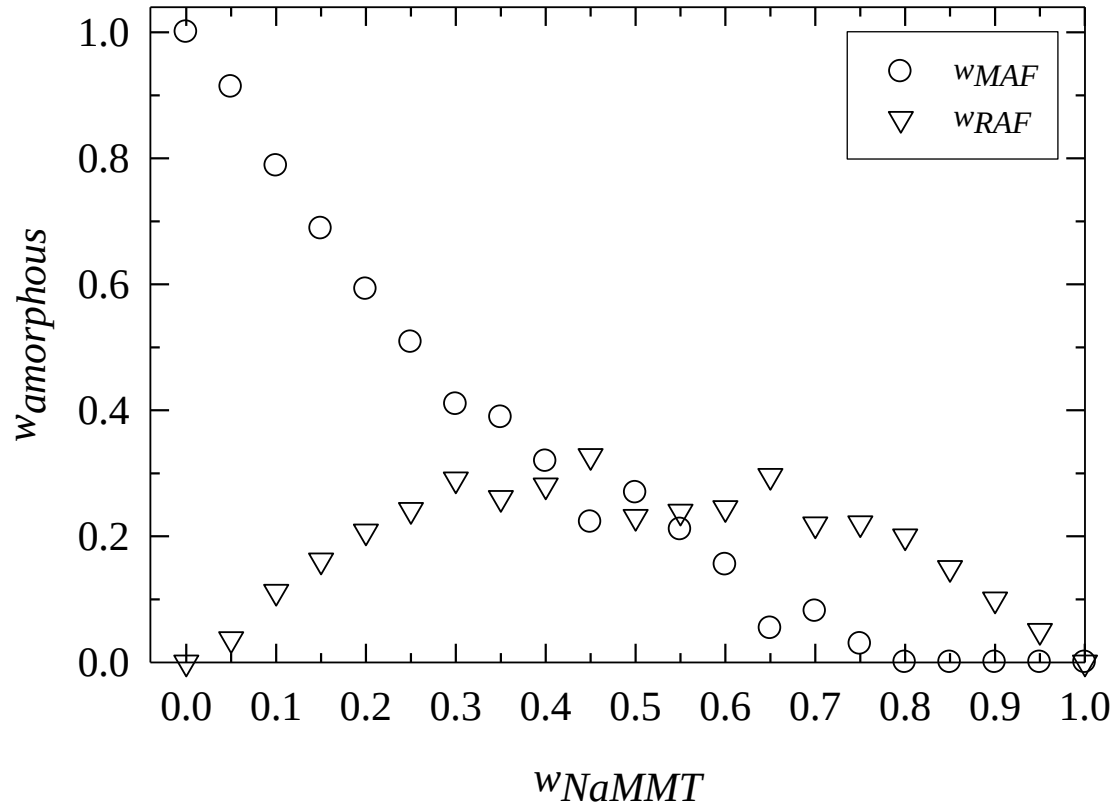

Figure 24. Weight fractions of MAF (○) and RAF (▽) as determined from ΔC_p at T_g for HBP4 nanocomposites as a function of weight fraction montmorillonite.

The weight fraction of RAF increased with clay content up to a w_{NaMMT} of 0.30 and then remained relatively constant until it began to decrease at the w_{NaMMT} of 0.80. As the clay content increased beyond this point, the RAF must have decreased linearly with clay content since the system was composed solely of RAF and Na^+MMT. It must be noted that as the content of clay increased in the nanocomposite systems, so too did the degree of clay ordering, as detailed in our previous paper. XRD and TEM showed that the systems progressed from a mixture of exfoliation and disordered intercalation at the lower clay loadings (0-30wt% Na^+MMT) to well ordered intercalation at higher clay

loadings. The effects of this ordering are clearly evident above 30wt%, where trends for the RAF and MAF with clay content begin to deviate from their apparent linear dependence vs. w_{NaMMT}. It is clear by comparing the changes in the RAF and MAF vs. clay content trends that RAF and MAF were dependent upon more than the fraction of clay within the systems. Indeed, an observation of Figure 19 reveals that at 35wt% Na^{+}MMT, the interlayer spacings began to change from populations at 1.5 nm to those composed of 1.0 nm interlayers. This indicated that the changing clay morphologies directly impacted RAF formation. This morphological progression, and its effect on RAF formation, will be addressed in further detail later in the discussion.

Probing the Amorphous Fractions by PALS

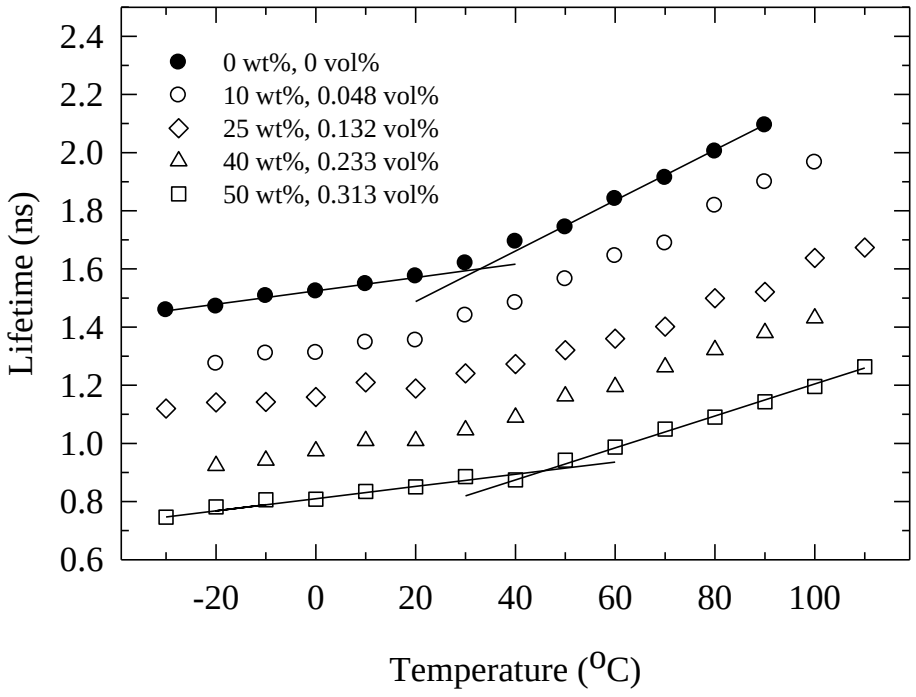

Figure 25. Orthopositronium lifetimes for HBP4 nanocomposites as a function of temperature.

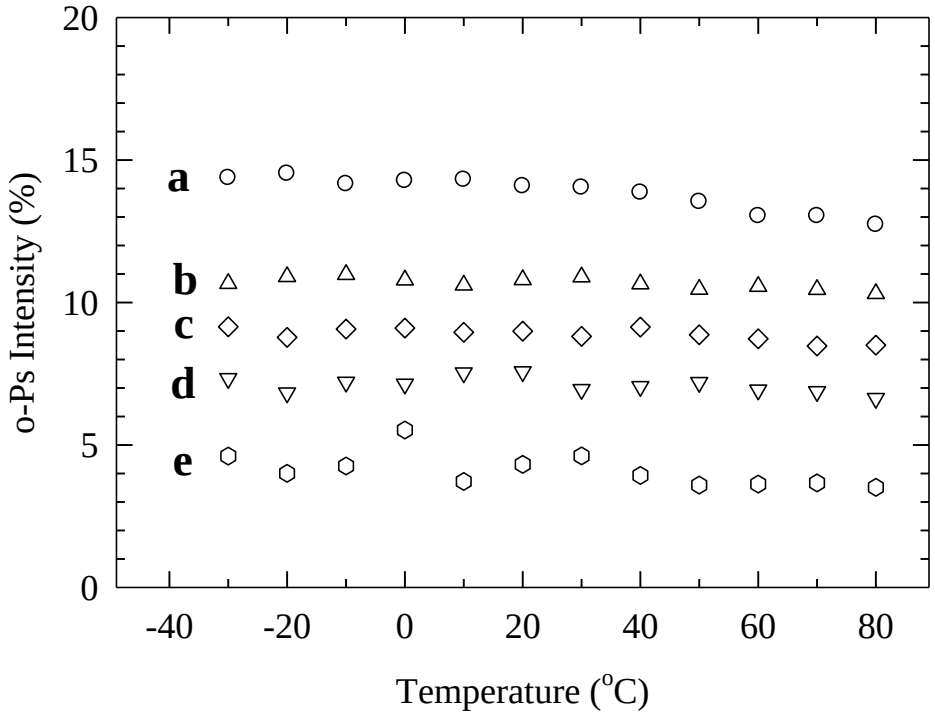

Figure 26. Orthopositronium intensities for HBP4 nanocomposites as a function of temperature at the following MMT fractions: (a) 0% MMT, (b) 23% vol/vol, (c) 31% vol/vol, (d) 52% vol/vol, (e) 65% vol/vol.

Having observed and quantified the rigid amorphous fraction by DSC, we proceeded to analyze the effects of the RAF formation upon the free volume properties of the nanocomposites. Positron annihilation lifetime spectroscopy (PALS) allowed for the exploration of confinement effects in the nanocomposite matrix by probing the free volume changes in the hyperbranched polymer phases. In Figures 25 and 26, we show the temperature dependence of the o-Ps lifetimes, τ_3, and the o-Ps intensities, I_3, for the HBP4 nanocomposites. The data sets are compilations of three heating scans on the same sample films. It has been well established that the size of free-volume holes is closely related to macromolecular mobility, and it was expected that the effects of nanoconfinement would be reflected in the free volume measurements. As evident in Figure 27, τ_3 increased with temperature, indicative of the expansion of hole sizes with

heating. As expected of a polymeric system, a distinct increase in the thermal expansivity of τ_3 was observed at the glass transition temperature. The thermal expansion of hole volume in the liquid state is greater than that of the glassy state and causes an increase of the slope of τ_3 with temperature above T_g. No apparent differences in τ_3 or I_3 were observed when comparing the first heating scan against the subsequent scans. The o-Ps intensity, I_3, exhibited a negligible temperature dependence, which is characteristic of the behavior of amorphous polymers, and indicated that changes in hole density were insignificant with temperature [59]. However, I_3 was observed to decrease in the nanocomposites with clay content, as illustrated in Figure 26. This was attributed to the decrease in available free volume for o-Ps formation in the nanocomposites due to the presence of the montmorillonite, which due to its crystalline nature and high density, was unlikely to allow o-Ps formation.

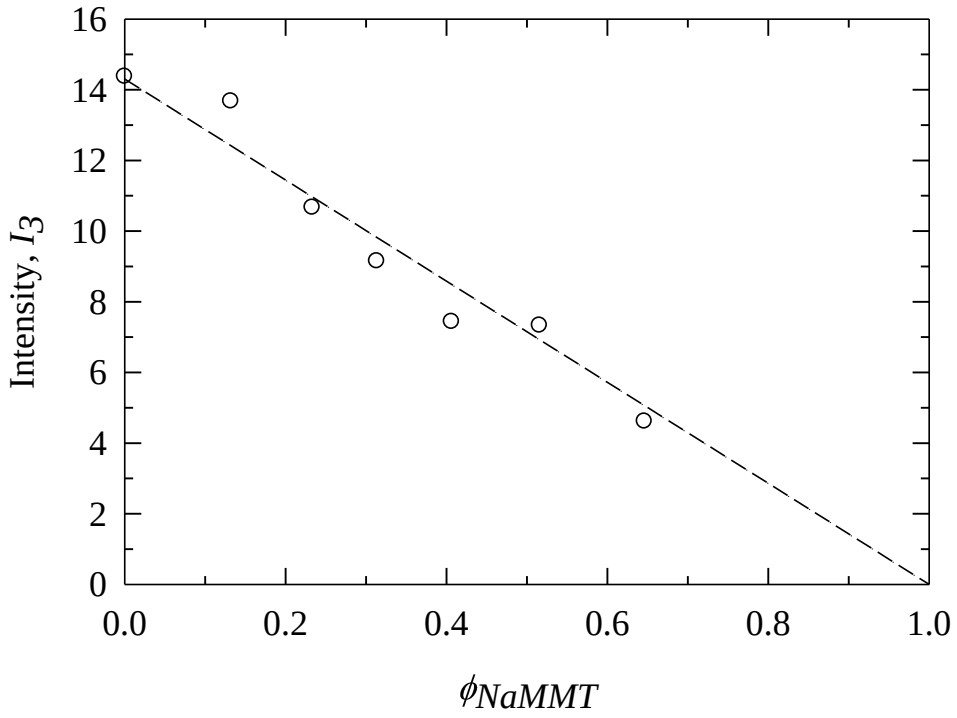

Figure 27. o-Ps intensity, I_3, at -30 °C vs. volume fraction Na^+MMT.

The reduction in o-Ps intensity, I_3, with the volume fraction of Na^+MMT are plotted in Figure 27. Similar reductions in I_3 have been observed in other nanocomposite systems [60-62]. Decreases in o-Ps intensities have also been observed in certain semicrystalline systems, such as poly(ether ether ketone) where the o-Ps could not form within the polymer crystallites [63,64]. It has been demonstrated that there is minimal positronium formation in the clay layers [65]. In order to verify that the contribution of o-Ps from the clay layers was indeed minimal, an analysis of the pure Na^+MMT was performed by PALS. The clay was dried for two days under vacuum at 120°C and then pressed in a mold to form 10 mm by 1 mm discs that were used for the PALS analysis. Ortho positronium lifetimes in the range of 1-10 *ns* were not observed from the PALS temperature scans of the clay.

The observed o-Ps lifetimes ranged from 1.5 *ns* to 2.2 *ns* over the temperature ranges studied. Upon close inspection of the τ_3 data with temperature it became apparent that the slope above T_g decreased in a non-linear fashion with clay content, whereas the slopes below T_g remained constant. Below T_g, the amorphous HBP4 is in a vitrified state and there were no apparent changes in slope with clay content below T_g. The observed negative deviation of the temperature coefficient, from pure HBP4, above T_g indicated that a fraction of the amorphous phase exhibited a lower thermal expansivity than the pure HBP4. Since the RAF consists of the amorphous polymer in a vitrified state, it was reasonable to assume that, based upon the consistency of the τ_3 slopes below T_g, the temperature coefficient of the RAF component was equal to that of the vitrified HBP4. We hypothesized that the decreases in the τ_3 slope of the nanocomposites above T_g, relative to the neat HBP4, were due to an additive effect of the RAF and MAF fractions

within the nanocomposites. By this reasoning, the volume fractions of RAF and MAF were quantifiable from the slopes of the hole free volume data with temperature.

To proceed with this analysis, we needed to individually characterize the PALS contributions from RAF and MAF. We assumed spherical holes and applied the Tao-Eldrup equation to calculate the free volume hole radius [66,67]:

$$\tau_3 = \frac{1}{2}\left[1 - \frac{R}{R_0} + \frac{1}{2\pi} Sin\left(\frac{2\pi R}{R_0}\right)\right]^{-1} \quad (2)$$

where R is the hole radius in Å. R_0 equals $R + \Delta R$ where ΔR is the fitted empirical electron layer thickness of 1.66 Å. The hole size, V_h, was calculated by $\langle V_h \rangle = (4/3)\pi R^3$ and is plotted in Figure 28.

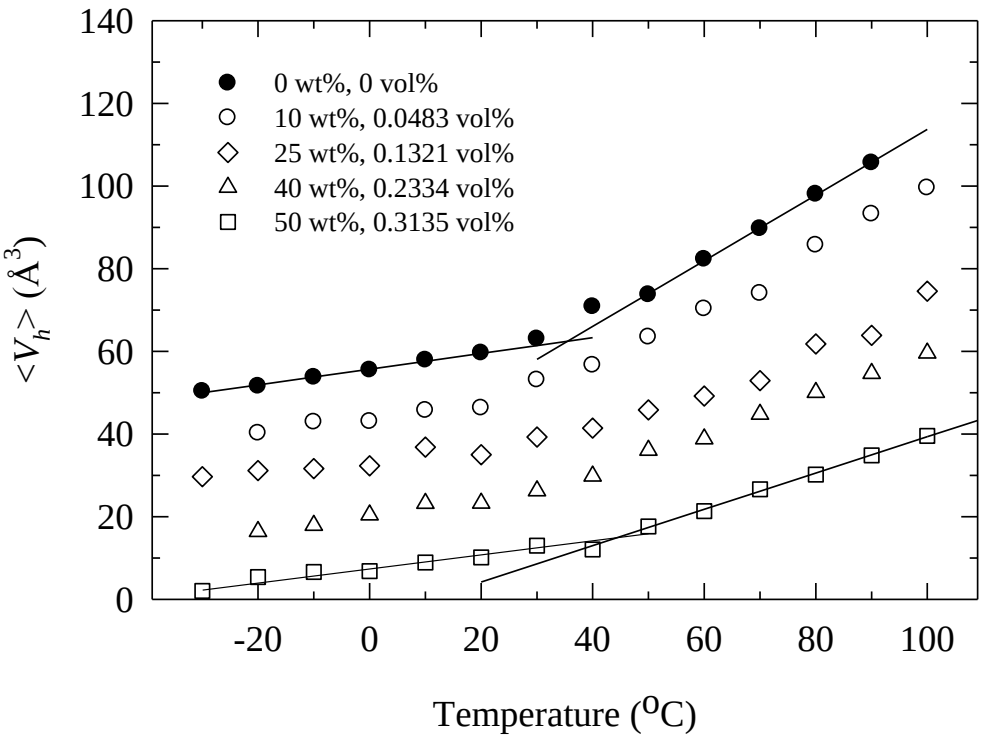

Figure 28. Hole free volume, V_h, plots for nanocomposites. Vertically offset for clarity.

V_h ranged from 50-120 Å^3 over the temperature range studied. We assumed that o-Ps formation occurred only in the amorphous HBP4 phases, and that the changes in V_h with temperature for the pure HBP4 above T_g only reflected the behavior of the HBP4 mobile amorphous fraction. The V_h temperature coefficient of the vitrified, neat, HBP4 below T_g was taken to be equal to the V_h temperature coefficient of the RAF, which remained vitrified by clay confinement above T_g. Since the contributions of RAF and MAF to V_h are considered additive we have the following relationship

$$V_h = \frac{N^{\mathrm{RAF}} V_h^{\mathrm{RAF}} + N^{\mathrm{MAF}} V_h^{\mathrm{MAF}}}{N^{\mathrm{RAF}} + N^{\mathrm{MAF}}} \tag{3}$$

where V_{h} is the average hole volume as measured for the composite, V_h^{RAF} is the average hole volume as measured for RAF, and V_h^{MAF} is the average hole volume as measured for MAF. N^{RAF} is the number of free volume holes for RAF, and N^{MAF} is the number of free volume holes for MAF. Since this analysis is dependent upon the V_h slopes with temperature, a linear regression of V_h in the glassy state and in the equilibrium melt was required, examples of which are included in Figure 28. For this linear regression the data points from 20-40°C are excluded, as they were very close to the glass transition. The linear slope of V_h versus T, e_h, for the nanocomposites were thusly defined as

$$e_h = \frac{dV_h}{dT} \tag{4}$$

Since the slope of the samples below T_g remained constant, the linear slope of the RAF below Tg were defined as

$$e_h^{\mathrm{RAF}} = \left.\frac{dV_h}{dT}\right|_{T<T_g} \tag{5}$$

As there was no hyperbranched polymer crystallinity evidenced by DSC or XRD, the pure HBP4 was considered composed entirely of MAF, above T_g, and thus the slope for the MAF was defined as

$$e_h^{\mathrm{MAF}} = \left.\frac{dV_h^{\mathrm{Polyol}}}{dT}\right|_{T \geq T_g} \tag{6}$$

Based upon the negligible changes of I_3, above and below T_g, we assume that the number density of holes, $n = N_i/V_i$, is the same for RAF and MAF. Since n is constant, Equation 3 can be rearranged as follows where $\varphi_{RAF} + \varphi_{MAF} + \varphi_{NaMMT} = 1$:

$$V_h = \frac{\varphi^{\mathrm{RAF}} V_h^{\mathrm{RAF}} + \varphi^{\mathrm{MAF}} V_h^{\mathrm{MAF}}}{\varphi^{\mathrm{RAF}} + \varphi^{\mathrm{MAF}}} \tag{7}$$

Taking the derivative of Equation 7 with respect to temperature yields the final equation for the slope of V_h with temperature, with no adjustable parameters:

$$e_h = \frac{\varphi^{\mathrm{RAF}} e_h^{\mathrm{RAF}} + \varphi^{\mathrm{MAF}} e_h^{\mathrm{MAF}}}{\varphi^{\mathrm{RAF}} + \varphi^{\mathrm{MAF}}} \tag{8}$$

Employing Equation 8 allowed for φ_{RAF} and φ_{MAF} to be extracted from the slope, e_h, of the o-Ps lifetime plots with temperature. For the pure HBP4, the average slope below T_g, e_h^{RAF}, was 0.185 and the average slope above T_g, e_h^{MAF}, was 0.790. The correlation coefficients were at or above 0.99 for the linear regression analysis, and the results from the τ_3 slope analysis are summarized in Table 3. The resulting φ_{RAF} and φ_{MAF} determined from the o-Ps lifetime experiments are plotted in Figure 29 relative to the volume fraction of Na^+MMT. The volume fractions of the amorphous phases as determined by the previous DSC analysis are included for comparative purposes.

Table 3

Amorphous volume fractions determined from the free volume temperature coefficients of HBP4 nanocomposites

w_{MMT}	φ_{MMT}	e_h	φ_{MAF}	φ_{RAF}
0	0	0.790	1.00	0
0.10	0.048	0.734	0.864	0.088
0.25	0.132	0.571	0.554	0.314
0.40	0.233	0.491	0.388	0.378
0.50	0.313	0.485	0.340	0.347

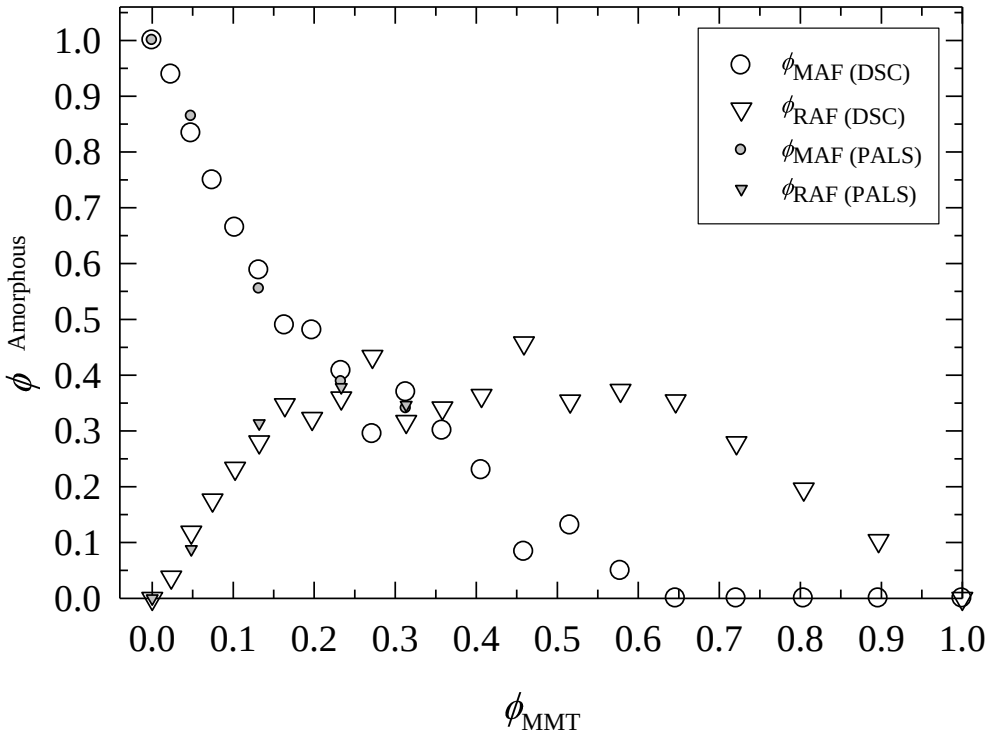

Figure 29. Volume fractions of RAF (▼) and MAF (●) vs. volume fraction montmorillonite, as determined from the τ_3 slope analysis (PALS). Volume fractions of MAF (○) and RAF (▽) determined from ΔC_p at T_g (DSC).

As can be seen in Figure 29, the volume fractions of amorphous HBP4 determined from the o-Ps lifetime analysis are very similar to those determined from analyzing the changes in heat capacity at T_g. This provided additional evidence that the RAF phase remained vitrified well above the glass transition temperature due to the constraints imposed by the surfaces of the montmorillonite clay layers. Therefore, it was clearly demonstrated by both the bulk thermal and bulk free volume techniques that the adsorption, flattening, and confinement of the HBP lead to the vitrification of a portion of the HBP, which remained vitrified well above the glass transition temperature. The nanocomposite morphology is correlated with the observed amorphous fractions in the following section.

Correlating Amorphous Fractions and Interlayer Spacings

Having quantified the rigid and mobile amorphous fractions from the DSC data, and having verified this by PALS, it was reasonable to attempt a correlation between the thoroughly investigated clay morphology and the observed changes in the amorphous fractions. The presence of the clay had a significant impact upon the amorphous fraction and caused the formation of the RAF. A reasonable assumption to make with regard to the RAF was that it formed within the clay galleries of the intercalated stacks. Based on this assumption, the amount of RAF could be calculated from the known content of clay and the observed interlayer spacings, as determined from the use of the powdered nanocomposite analyzed by XRD.

In order to correlate the morphology with the quantities of RAF observed, we formulated mathematical models, based upon the following assumptions. We assumed that the RAF corresponded directly to the intercalated polymer contained within the clay

tactoids. We also assumed that the clay surfaces were completely covered by available HBP4, with no gaps in the surface coverage, and that the density of the rigid amorphous fraction was the same as the mobile amorphous fraction, as previously determined. The large lateral dimensions of the clay far exceed the 1 nm layer thickness; therefore, any edge effects are neglected in this analysis. The change in heat capacity at the glass transition was due only to the weight fraction of the mobile amorphous fraction, w_{MAF}, where $w_{\text{Clay}} + w_{RAF +} w_{MAF} = 1$. A rearrangement of Equation 1 yields the following relationship:

$$\Delta C_p = \Delta C_p^0 \left[1 - \ w_{NaMMT} + w_{RAF} \ \right] \tag{9}$$

where ΔC_p is the change in heat capacity of the nanocomposite at T_g, $\Delta C_p°$ is the heat capacity of the amorphous polymer (pure HBP4) at T_g, w_{NaMMT} is the weight fraction of montmorillonite, w_{MAF} is the weight fraction of MAF, and w_{RAF} is the weight fraction of RAF. In Scheme 2, a basic outline of the polymer intercalated in the Na^+MMT layers and the representative terms are presented as applied to this analysis.

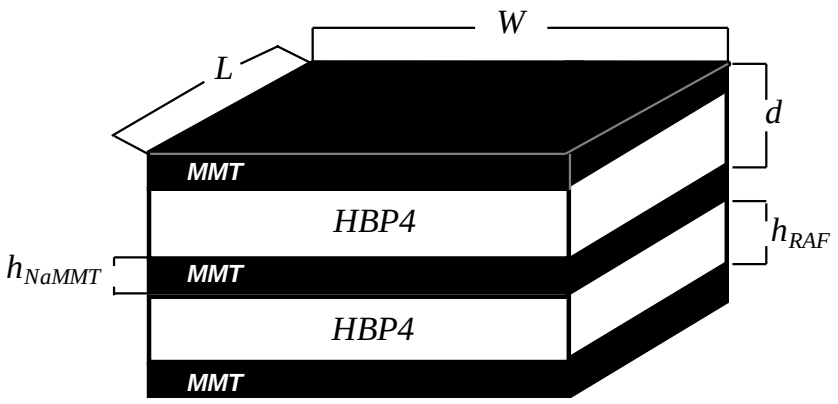

$$d = h_{RAF} + h_{NaMMT}$$

Scheme 2. HBP4 intercalated between Na^+MMT layers. Interlayer spacings correspond to h_{RAF}, d-spacings correspond to *d*, *L* and *W* denote stack length and width, and h_{NaMMT} corresponds to the clay layer thickness, determined to be 0.96 nm by XRD.

Interlayer spacings were determined from the X-ray diffraction peaks using Bragg's law by subtracting the thickness of the MMT layers, h_{NaMMT} (0.96 nm), from the determined *d*-spacings. Since we assumed that the interlayers were composed entirely of RAF, the thickness of these layers was designated as h_{RAF}. *W* and *L* represent the length and width of the clay stacks. The volume of the clay can be expressed as follows, $V_{NaMMT} = nL_{NaMMT}W_{NaMMT}h_{NaMMT}$, where *n* equals the number of MMT layers. Since the RAF is assumed to be only within the MMT stacks, the volume of RAF can be expressed as $V_{RAF} = (n\text{-}1)L_{RAF}W_{RAF}h_{RAF}$. As stated, complete surface coverage of the MMT layers by RAF is assumed within these stacks; thus, *L* and *W* for the RAF and MMT are equal and the ratio of V_{RAF}/V_{NaMMT}, which directly determines the heights of the RAF and MMT layers, can be expressed as follows:

$$\frac{V_{RAF}}{V_{NaMMT}} = \frac{(n-1)h_{RAF}}{nh_{NaMMT}} \tag{10}$$

From the analysis of the clay morphology by TEM, the thickness of these intercalated stacks was observed to increase with clay content as the system ordering increased. Although this relationship may not hold at the lower clay loadings where the clay morphology is more disordered, we make the assumption that *n* approaches large enough values that Equation 10 reduces to

$$\frac{V_{RAF}}{V_{NaMMT}} = \frac{h_{RAF}}{h_{NaMMT}} \tag{11}$$

Taking the mass of the nanocomposite as *x*, the following relationships apply:

$$V_{NaMMT} = \frac{xw_{NaMMT}}{\rho_{NaMMT}} \tag{12}$$

and

$$V_{RAF} = \frac{xw_{RAF}}{\rho_{RAF}} \tag{13}$$

The density of the RAF, ρ_{RAF}, is 1.306 g/cm^3 and ρ_{NaMMT} is 2.86 g/cm^3. Combining Equations 11, 12, and 13 yields the following relationship for w_{RAF}:

$$w_{RAF} = \frac{h_{RAF}\rho_{RAF}w_{NaMMT}}{h_{NaMMT}\rho_{NaMMT}} \tag{14}$$

Combining Equation 14 with Equation 9 allowed for the prediction of heat capacity based upon the observed interlayer spacings:

$$\Delta C_p = \Delta C_p^{\,o}\left[1 - w_{NaMMT}\left(1 + \frac{h_{RAF}\rho_{RAF}}{h_{NaMMT}\rho_{NaMMT}}\right)\right] \tag{15}$$

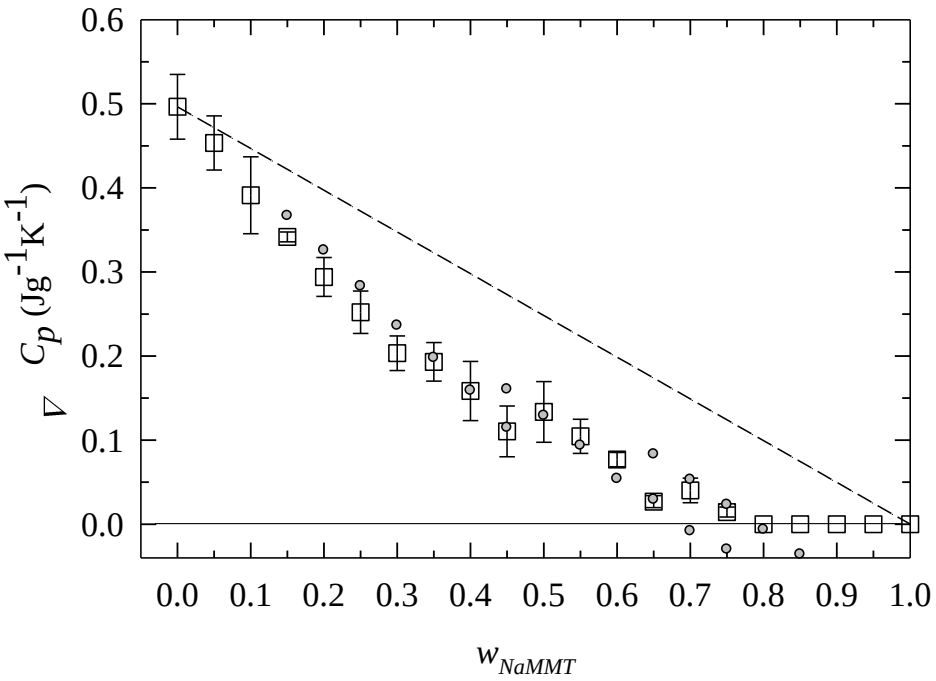

Figure 30. (●) Predictions of heat capacity change ΔC_p at T_g for HBP4 nanocomposites based upon clay content and observed first order diffraction (XRD) peaks. (□) Observed heat capacity change ΔC_p at T_g for HBP4 nanocomposites. Plotted as a function of weight fraction Na^+MMT.

By utilizing Equation 15 with the observed first order peaks from the XRD analysis of the powdered nanocomposite samples (Figure 19), the expected changes in heat capacity, ΔC_p, at T_g were calculated and are shown in Figure 30. A strong correlation existed between ΔC_p predicted by this methodology and the values observed by the DSC analysis. Where two prominent first order peaks were observed by XRD, each was applied to Equation 15. The larger of the interlayer spacings necessarily gave the lower predicted value for ΔC_p, since more HBP4 was confined in these interlayers. A close inspection of Figure 30 shows that the correlation between the observed and predicted ΔC_p is best when the weight fraction of Na^+MMT exceeds 30 wt%. This is not surprising since, at the higher clay loadings, intercalation was dominant and the stack sizes were large enough that the number of layers, *n*, could be overlooked. Figure 31 shows the extent of exfoliation and the average number of observed clay layers per clay stack vs. w_{NaMMT} from the image analysis of TEM micrographs for the HBP4 nanocomposite systems. The morphological transition, with increasing clay content, from a mixture of exfoliated and disordered intercalated clay layers to more highly ordered and flocculated intercalated clay tactoids can be observed in Figure 32, and is indicative of the morphological transition from a disordered to highly intercalated state.

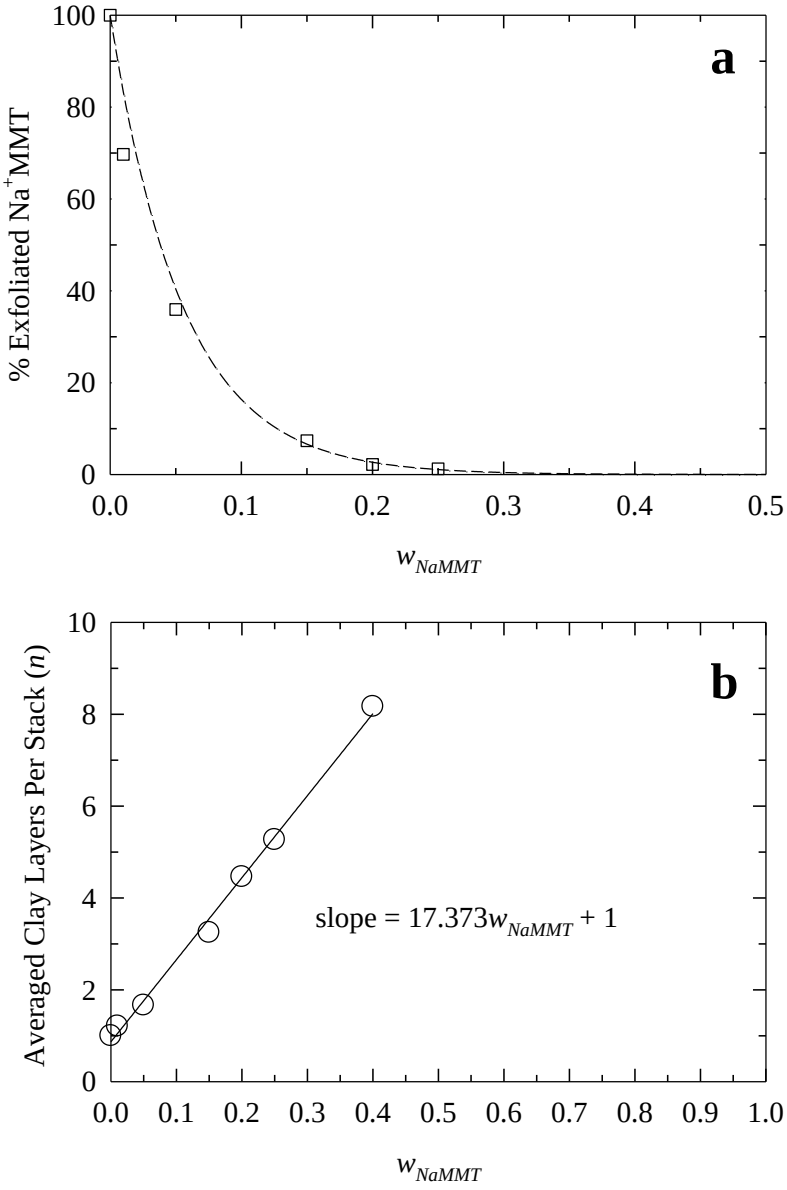

Figure 31. (a) Observed percentage of exfoliated clay layers with clay content by TEM. (b) Average number of MMT layers in individual clay stacks as determined by TEM analysis.

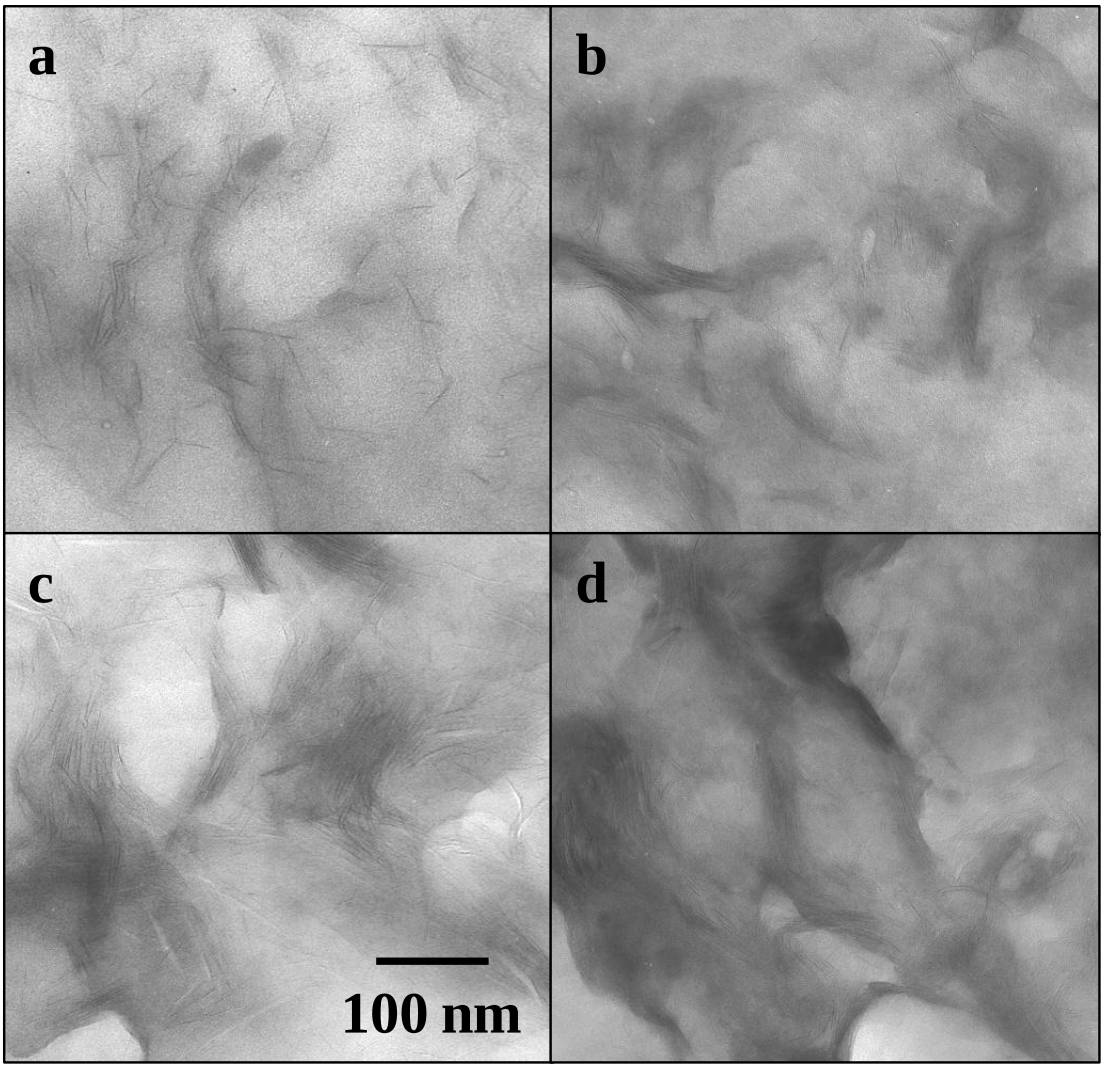

Figure 32. Representative high magnification TEM micrographs of HBP4/Na^{+}MMT nanocomposites (A) 5, (B) 15, (C) 25, and (D) 40% wt/wt clay content.

Considering the close correlation between the observed ΔC_p and that predicted by Equation 15, it was equally reasonable to predict the interlayer spacings for the nanocomposite structures based upon the observed changes in heat capacity. Indeed, Equation 15 can be rearranged so that h_{RAF} may be calculated from observed ΔC_p values determined by DSC and the known clay compositions:

$$h_{RAF} = \frac{(1 - w_{NaMMT} - \Delta C_p / \Delta C_p^o) h_{NaMMT} \rho_{NaMMT}}{\rho_{RAF} w_{NaMMT}} \quad (16)$$

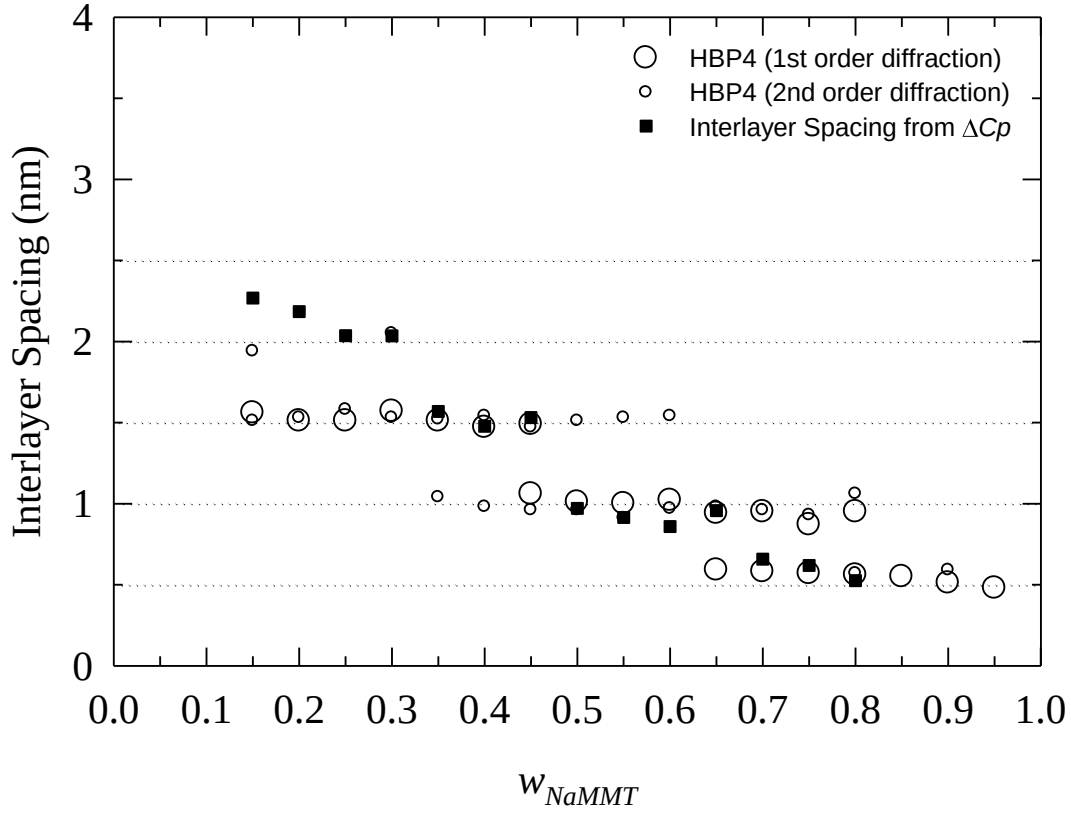

Figure 33. Interlayer spacings predicted using eqn. 14 (■), calculated from the experimentally determined values for ΔC_p at T_g. Interlayer spacings observed directly by XRD for the powdered HBP4 nanocomposites (○). Plotted as a function of weight fraction Na^+MMT.

Utilizing the experimentally determined values for ΔC_p at T_g, the interlayer spacings predicted by Equation 16 are plotted alongside the interlayer spacings observed by XRD in Figure 33. There was an excellent correlation of the interlayer spacings calculated utilizing the measured ΔC_p at T_g with those observed by XRD above 30 wt% Na^+MMT. As discussed in the previous publication regarding these nanocomposites, there existed multiple, discrete, interlayer populations for many of the compositions, which made pinning down a single value for each of the nanocomposite's interlayer

spacing difficult [28]. However, in the higher clay content regimes above 30 wt% Na^{+}MMT, there was a strong correspondence between the observed first order interlayer spacings and the values predicted by analysis of the ΔC_p. For example, in the range of nanocomposites from 65-80 wt% Na^{+}MMT, the presence of multiple population states are shown in the XRD diffractograms shown in Figure 34. Within this range, as the concentration of clay increased, the observed interlayer spacings changed incrementally from a predominant interlayer spacing of ~1 nm to ~0.5 nm, demonstrated by the shift of the first order peaks to higher diffraction angles. This change in interlayer spacings was also seen in the prediction from the ΔC_p measurements in Figure 33, where the predicted interlayer spacings changed from ~ 1nm to ~ 0.5 nm, representative of the changes observed by XRD.

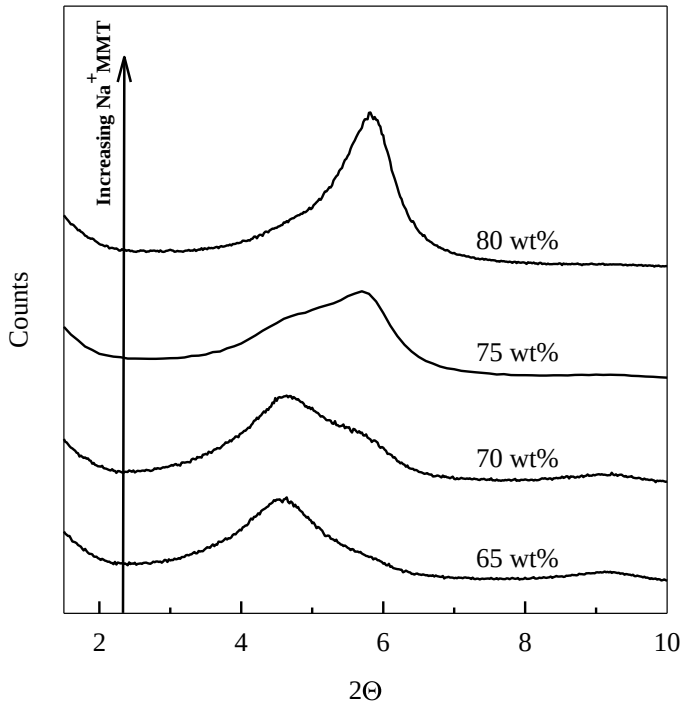

Figure 34. XRD diffractograms of HBP4 nanocomposites over the range of 65-80 wt% Na^{+}MMT. Scans vertically offset for clarity.

The spacing trends observed by XRD indicated step-wise changes in increments of ~0.5 nm, and, indeed, the calculated interlayer spacings based upon DSC measurements also trended in a similar fashion but were determined by a very different technique. Based upon the trends observed between the predicted interlayer spacing values and the diffraction peaks observed by XRD, it appears that with amorphous polymers intercalated in clay layers, DSC gave a reasonable indication of the interlayer spacings, based upon the ΔC_p at T_g. In an amorphous clay nanocomposite system with narrow d-spacing distributions, one could expect this methodology to yield even clearer agreement between predicted interlayer spacings by DSC and those observed by X-ray techniques. Despite the large correlation between the DSC data and the XRD data, there existed a strong deviation between the observed and predicted interlayer spacings at and below 30 wt% Na^+MMT, which cannot reasonably be overlooked.

The deviation in the calculated interlayer spacings from those observed by XRD at the lower clay loadings was a strong indication that RAF formation was not restricted solely to the interlayer domains. The clay stacks were small (1-5 clay layers per stack) in this low compositional range, with exfoliated and disordered intercalated states also present. At the higher clay loadings, due to the larger stack sizes, the amount of external RAF relative to that between the clay layers was less significant.

To address these smaller stack sizes Equation 16 was modified to include the number of clay layers, n. In this case h_{RAF} was determined by the following relationship:

$$h_{RAF} = \frac{(1 - w_{NaMMT} - \Delta C_p / \Delta C_p^o) n h_{NaMMT} \rho_{NaMMT}}{(n-1)\rho_{RAF} w_{NaMMT}} \tag{17}$$

The number of clay layers, *n*, was taken as equal to the average number of clay layers per stack and was extrapolated from the slope of the average number of clay layers per stack in Figure 31b. The interlayer spacings determined by Equation 17 are shown in Figure 35. The compositional range from the weight fraction of clay from 0.15 to 0.30 was analyzed since the interlayer spacings of the powdered nanocomposites were observed by XRD, in this compositional range. As can be seen, there was a significant deviation from the observed XRD interlayer spacings and those predicted by Equation 17. This strongly indicated that the RAF must also have formed exterior to the intercalated stacks. In an attempt to quantify the additional RAF formed outside the stacks we modified Equation 10 as follows:

$$\frac{V_{RAF}}{V_{NaMMT}} = \frac{(n-1)h_{RAF} + 2h_{EXTRAF}}{nh_{NaMMT}} \tag{18}$$

where h_{EXTRAF} represents the thickness of the RAF on each face of the clay stacks. Following the previous logics and Equation 18 yielded the following relationship for h_{RAF}:

$$h_{RAF} = \frac{(1 - w_{NaMMT} - \Delta C_p / \Delta C_p^o) n h_{NaMMT} \rho_{NaMMT} - \rho_{RAF} w_{NaMMT} 2h_{EXTRAF}}{(n-1)\rho_{RAF} w_{NaMMT}} \tag{19}$$

In Figure 35, Equation 19 was used to determine h_{RAF} assuming values for h_{EXTRAF} of 1.5, 2.0, and 2.5 nm. An analysis of these plots indicates that the predicted interlayer spacings most closely matching those observed from the WAXD possessed a value for h_{EXTRAF} of 2 nm. This implied that the clay layers hindered the mobility of the amorphous phase for about 2 nm on each side of the clay stacks, in addition to the confinement of the HBP4 within the clay galleries. This value of 2 nm for the immobilized polymer layer

was also observed in SiO_2 nanoparticle composites prepared with PMMA [33]. Dielectric relaxation spectroscopy of PDMS nanocomposites containing silica nanoparticles has also indicated that an interfacial region of ~2 nm surrounded the nanoparticles and inhibited the molecular mobility of the polymer [68]. However, the interfacial thicknesses in nanocomposite systems does show a dependence upon the interaction of the polymer with the filler surface and 2 nm is not always assured. With nanocomposites prepared from PEO and Na^+MMT the suppression of crystallinity in the polymer matrix was attributed to PEO confined in the intercalated stacks and this external PEO ordered layer was estimated at 5-10 nm in thickness [69].

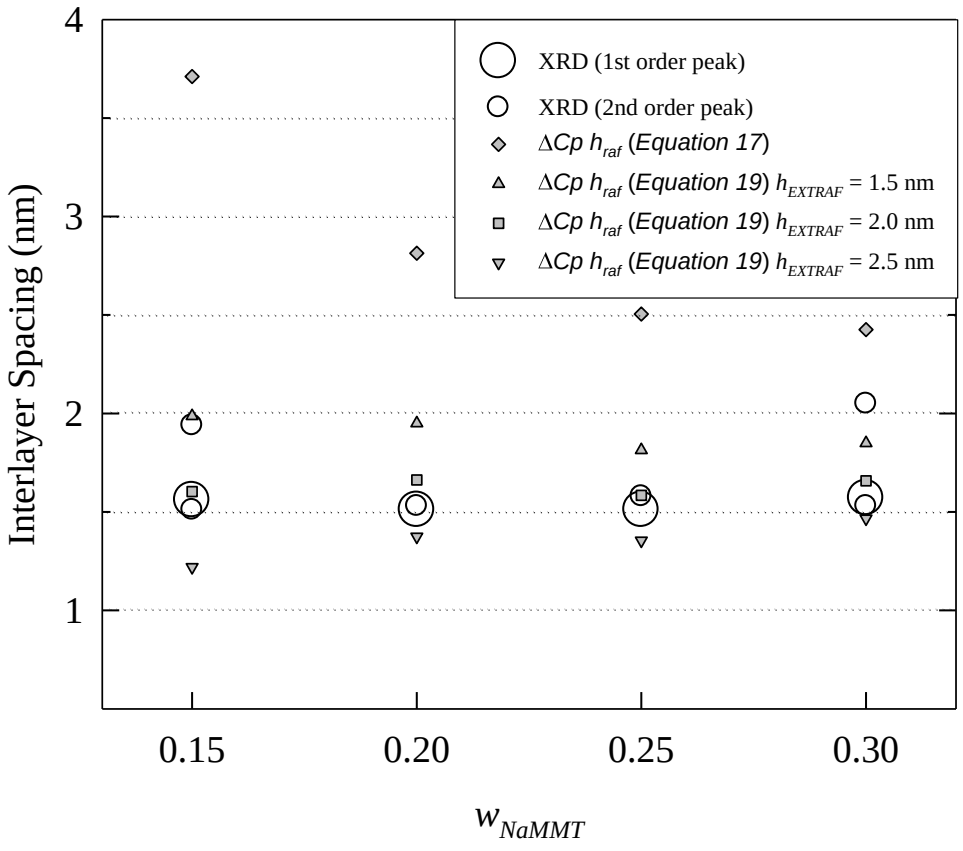

Figure 35. Interlayer spacing predicted from Equations 17 and 19 that utilize the number of layers per stack, n, as determined from TEM. Included are the interlayer spacings observed by XRD for the powered HBP4 nanocomposites.

At the lower clay loadings the nanocomposites were populated by a mixed morphology of exfoliated, intercalated, and disordered intercalated clay layers, so it was appropriate to look at the interaction of the clay layers with the HBP4 without consideration of the intercalation state. At these lower clay contents (up to w_{NaMMT} of 0.3, φ_{NaMMT} of 0.16) the trend of amorphous fractions with clay content was linear in nature, as shown in Figure 36. This indicated that in this compositional range, the amount of clay directly correlated to the amount of RAF formed. An analysis of the linear slope of φ_{RAF} with φ_{NaMMT} yielded the following relationship: $\varphi_{RAF} = 2.175\ \varphi_{NaMMT}$. Maintaining the assumption of complete surface coverage of the clay layers by RAF, an estimation of h_{RAF} can be determined by multiplying the slope of 2.175 by h_{NaMMT} (0.96 nm), which yields a value of 2.09 for h_{RAF}. This simple interpretation implies a total of 2.09 nm of RAF formed on the surfaces of each layer of clay. If one assumed that the RAF was evenly distributed on the clay layers, irrespective of the actual intercalation state, then this would imply that the intercalated structures would have possessed an interlayer of 2.09 nm, with 1.045 nm of RAF on either side of the clay stacks. Of course, the relationship derived this way does not hold past 30 wt% Na^+MMMT (0.164% vol/vol), and, indeed, if it did a complete suppression of the glass transition at slightly over 50 wt% clay (0.315% vol/vol) would have been observed.

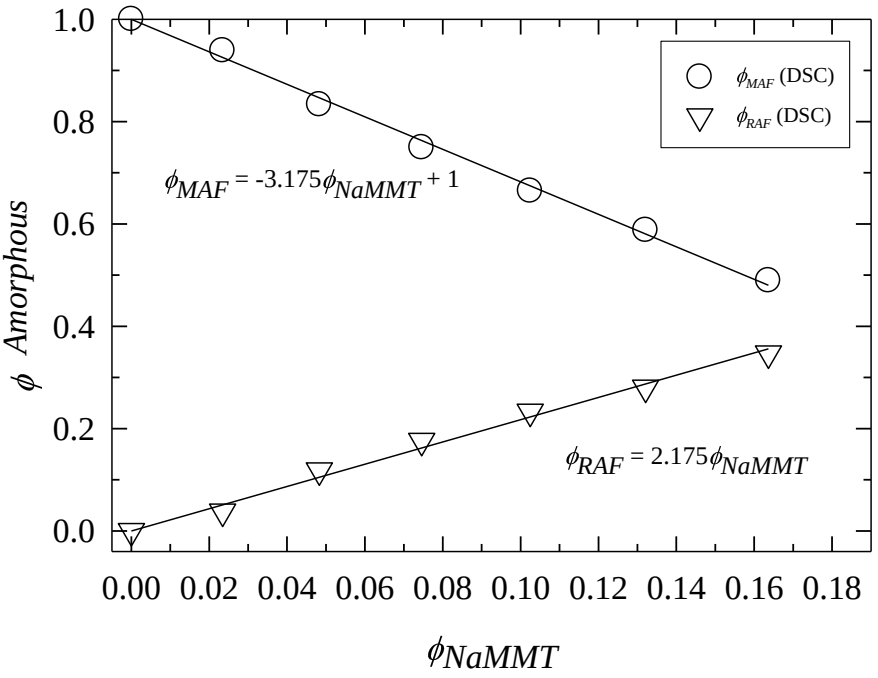

Figure 36. Slopes of volume fractions of RAF and MAF with volume fraction Na^{+}MMT from ΔC_p at T_g.

The results from the two analyses in the low clay content regime are not significantly different, and may indeed be complimentary, since below 15 wt% Na^{+}MMT, the clay layers were possessed of a higher degree of both exfoliated and disordered intercalated states. Indeed, what this analysis does demonstrate is that there was certainly a contribution from the clay surfaces to the formation of RAF, irrespective of whether the HBP4 was inside an intercalated stack. As stated, this lower clay content regime presented a mixed morphology; therefore, a true determination of interlayer spacings may not be possible from the changes in heat capacity at T_g. It is apparent that the effect of the clay on the polymer matrix extends, at least to some extent, beyond that of the intercalated HBP4 trapped between the stacked silicate sheets. However, the relative contribution from RAF external to the clay aggregates grew less significant as the stacks increased in size, which was demonstrated by the excellent correspondence, above

30 wt% Na^+MMT, of the heat capacity changes at the glass transition temperature with the interlayer spacings obtained from X-ray analysis.

Conclusions

The fourth generation of hydroxylated dendritic polyester based on 2,2-bis-methylopropionic acid (bis-MPA) with an ethoxylated pentaerythritol (PP50) core, HBP4, was combined with unmodified sodium montmorillonite clay (Na^+MMT) using water as a solvent to generate a broad range of polymer clay nanocomposite films covering compositions from 0 to 100% wt/wt Na^+MMT. X-ray diffraction (XRD) and transmission electron microscopy (TEM) were used to investigate the intercalation of these hyperbranched polymers (HBPs) into clay galleries. It was shown that the intercalated state was the predominant state in these nanocomposites and interlayer spacings changed with 0.5 nm increments, which corresponded to a flattened conformation of the confined HBPs. Both XRD and TEM revealed the presence of several coexisting intercalated populations exhibiting different interlayer spacings in multiples of 0.5 nm.

Differential Scanning Calorimetry, DSC, showed the glass transition temperature, T_g, to increase from 24°C to about 30°C at 15 wt% Na^+MMT, which corresponded to the onset of a flocculated network of intercalated clay stacks, as evidenced by TEM. The T_g then remained relatively constant, at 30°C, up to 55 wt% Na^+MMT. From 60-75 wt% Na^+MMT, the glass transition plateaued again at around 36°C, which may have been due to additional constraints imposed by the small mobile amorphous fractions, MAF, of free HBP4 wedged between the flocculated clay tactoids. The changes in heat capacity, ΔC_p, at T_g were observed to decrease as the amount of clay in the system increased, until they

were completely suppressed at and above 80 wt% Na^+MMT. This was attributed to the formation of a rigid amorphous fraction, RAF, which consisted of HBP4 that remained vitrified due to the strong attraction to, and confinement by, the clay layers. The fractions of RAF and MAF were quantified from the changes in heat capacity with clay content, and the trends of RAF and MAF formation in the nanocomposites were verified by the analysis of o-Ps lifetime trends with temperature using positron annihilation lifetime spectroscopy (PALS). This served to verify the glassy nature of the RAF constrained by the montmorillonite layers at elevated temperatures.

The observed interlayer spacings determined from the analysis of the powdered nanocomposite samples by XRD and the observed changes in heat capacity by DSC were correlated through mathematical models. It was found that, for the more highly ordered clay regimes above 30 wt% Na^+MMT, the observed interlayer spacings from XRD could be used to closely predict the changes in heat capacity observed at T_g by DSC. The same mathematical procedures allowed for a close prediction of the interlayer spacings observed by XRD using the changes in heat capacity observed by DSC. For the lower clay content regimes, at and below 30wt% Na^+MMT, the interlayer spacings were approximated from the DSC data trends utilizing modifications of the mathematical models, which indicated that RAF formation was not confined only to the intercalated HBP4, but also extended from both sides of the intercalated clay stacks. This investigation verified the strong confinement effect of the clay upon the hyperbranched hydroxylated polyesters, which was expected to occur based upon the observed flattened conformations of the hyperbranched polymers incorporated into the intercalated clay stacks.

References

[1] Alexandre M, Dubois P. Polymer-layered silicate nanocomposites: preparation, properties, and uses of a new class of materials. Mater Sci Eng 2000; 28: 1-63.

[2] Ray SS, Okamoto M. Polymer/layered silicate nanocomposites: a review from preparation to processing. Prog Polym Sci 2003; 28: 1539-1641.

[3] Tjong SC. Structural and mechanical properties of polymer nanocomposites. Mater Sci Eng 2006; 53: 73-197.

[4] Strawhecker KE, Manias E. Structure and properties of poly(vinyl alcohol)/Na Montmorillonite Nanocomposites. Chem Mater 2000; 12: 2943-2949.

[5] Jikei M, Kamimoto M. Hyperbranched polymers: a promising new class of materials. Prog Polym Sci 2001; 26: 1233-1285.

[6] Zhu PW, Zheng S, Simon G. Dielectric relaxations in a hyperbranched polyester with terminal hydroxyl groups: effects of generation number. Macromol Chem Phys 2001; 202: 3008-3017.

[7] Luciani A, Plummer CJG, Nguyen, T, Garamszegi L, Manson JE. Rheological and physical properties of aliphatic hyperbranched polyesters. J Polym Sci Part B Polym Phys 2004; 42: 1218-1225.

[8] Žagar E, Žigon M. Characterization of a commercial hyperbranched aliphatic polyester based on 2,2-bis(methylol)propionic acid. Macromolecules 2002; 35: 9913-9925.

[9] Žagar E, Huskić M, Žigon M. Structure-to-Properties Relationship of Aliphatic Hyperbranched Polyesters. Macrom Chem Phys 2007; 208: 1379-1387.

[10] Žagar E, Huskić M, Grdadolnik J, Žigon M, Zupančić-Valant A. Effect of annealing on the rheological and thermal properties of aliphatic hyperbranched polyester based on 2,2-bis(methylol)propionic acid. Macromolecules 2005; 38: 3933-3942.

[11] Žagar E, Žigon M, Podzimek S. Characterization of commercial aliphatic hyperbranched polyesters. Polymer 2006; 47: 166-175.

[12] Tanis I, Karatasos K. Local dynamics and hydrogen bonding in hyperbranched aliphatic polyesters. Macromolecules 2009; 42: 9581-9591.

[13] Malmström E, Johansson M, Hult A. Hyperbranched aliphatic polyesters. macromolecules 1995; 28: 1698-1703.

[14] Burgath A, Sunder, A, Frey H. Role of cyclization in the synthesis of hyperbranched aliphatic polyesters. Macromol Chem Phys 2000; 201: 782-791.

[15] Malmström E, Hult A. Kinetics of formation of hyperbranched polyesters based on 2,2-bis(methylol)propionic acid. Macromolecules 1996; 29: 1222-1228.

[16] Magnusson H, Malmström E, Hult A. Structure buildup in hyperbranched polymers from 2,2-bis(hydroxymethyl)propionic acid. Macromolecules 2000; 33: 3099-3014.

[17] Zeiner T, Shrader P, Enders S, Browarzik DJ. Phase and interfacial behavior of hyperbranched polymer solutions. Phase Equilib 2011; 302: 321-330.

[18] Peleshanko S, Tsukruk VV. The architectures and surface behavior of highly branched molecules. Prog Polym Sci 2008; 33: 523-580.

[19] Tsukruk VV. Dendritic macromolecules at interfaces. Adv Mater 1998; 10(3): 253-257.

[20] Tsukruk VV, Rinderspacher F, Bliznyuk VN. Self-assembled multilayer films from dendrimers. Langmuir 1997; 13: 2171-2176.

[21] Bakshi MS, Sood R, Kaur G, Sakai K, Yoshimura T, Esumi K. Characterization of aliphatic and aromatic polyester hyperbranched dendrimers by AFM imaging. Colloid Polym Sci 2005; 284: 74-79.

[22] Sheiko SS, Musafarov AM, Winkler RG, Getmanova EV, Eckert G, Reineker P. Contact angle microscopy on a carbosilane dendrimer with hydroxyl end groups: method for mesoscopic characterization of the surface structure. Langmuir 1997; 13: 4172-4181.

[23] Mansfield ML. Surface adsorption of model dendrimers. Polymer 1996; 37(17): 3835-3841.

[24] Plummer CJG, Gramszegi L, Leterrier Y, Rodlert M, Månson JE. Hyperbranched polymer layered silicate nanocomposites. Chem Mater 2002; 14: 486-488.

[25] Rodlert M, Plummer CJG, Grünbauer HJM, Månson, JE. Hyperbranched polymer/clay nanocomposites. Adv Eng Mater 2004; 6(9): 715-719.

[26] Rodlert M, Plummer CJG, Gramszegi L, Leterrier Y, Grunbauer HJM, Månson JE. Hyperbranched polymer/montmorillonite clay nanocomposites. Polymer 2004; 45: 949-960.

[27] Rodlert M, Plummer CJG, Leterrier Y, Månson JE. Rheological Behavior of Hyperbranched polymer/montmorillonite clay nanocomposites. J Rheol 2004; 48(5): 1049-1065.

[28] Decker JJ, Chvalun SN, Nazarenko S. Intercalation behavior of hydroxylated dendritic polyesters in polymer clay nanocomposites prepared from aqueous solution. Polymer 2011; 52: 3943-3955.

[29] Wunderlich B. Reversible crystallization and the rigid–amorphous phase in semicrystalline macromolecules. Prog Polym Sci 2003; 28: 383-450.

[30] Wunderlich B. Calorimetry of nanophases of macromolecules. Int J Thermophys 2007; 28: 958-967.

[31] Lin J, Shenogin S, Nazarenko S. Oxygen solubility and specific volume of rigid amorphous fraction in semicrystalline poly(ethylene terephthalate). Polymer 2002; 43: 4733-4743.

[32] Olson BG, Lin J, Nazarenko S, Jamieson AM. Positron annihilation lifetime spectroscopy of poly(ethylene terephthalate): contributions from rigid and mobile amorphous fractions. Macromolecules 2003; 36: 7618-7623.

[33] Sargsyan A, Tonoyan A, Davtyan S, Schick C. The amount of immobilized polymer in PMMA SiO_2 nanocomposites determined from calorimetric data. Eur Polym J 2007; 43: 3113-3127.

[34] Corcione EC, Maffezzoli A. Glass transition in thermosetting clay-nanocomposite polyurethanes. Thermochim Acta 2009; 485: 43-48.

[35] Wurm A, Ismail M, Kretzschmar B, Pospiech D, Schick C. Retarded crystallization in polyamide/layered silicates nanocomposites caused by an immobilized interphase. Macromolecules 2010; 43: 1480-1487.

[36] Fotiadou S, Chrissopoulou K, Frick B, Anastasiadis SH. Structure and dynamics of polymer chains in hydrophilic nanocomposites. J Polym Sci Part B Polym Phys 2010; 48: 1658-1667.

[37] Fotiadou S, Karageorgaki C, Chrissopoulou K, Karatasos K, Tanis I, Tragoudaras D, Frick B, Anastasiadis SH. Structure and dynamics of hyperbranched polymer/layered silicate nanocomposites. Macromolecules 2013; 46: 2842-2855.

[38] Pethrick RA. Positron annihilation-a probe for nanoscale voids and free volume? Prog Polym Sci 1997; 22: 1-47.

[39] Higuchi H, Yu Z, Jamieson AM, Simha R, McGervey JD. Thermal history and temperature dependence of viscoelastic properties of polymer glasses: relation to free volume quantities. J Polym Sci Polym Phys 1995; 33(17): 2295-2305.

[40] Simha R, Somcynsky T. On the statistical thermodynamics of spherical and chain molecule fluids. Macromolecules 1969; 2: 342-350.

[41] Dlubek G, Stejny J, Alam MA. Effect of cross-linking on the free-volume properties of diethylene glycol bis(allyl carbonate) polymer networks: a positron annihilation lifetime study. Macromolecules 1998; 31: 4574-4580.

[42] Srithawatpong R, Peng ZL, Olson BG, Jamieson AM, Simha R, McGervey JD, Maier TR, Halasa AF, Ishida H. Positron annihilation lifetime studies of changes in free volume on cross-linking cis-polyisoprene, high-vinyl polybutadiene, and their miscible blends. J Polym Sci Polym Phys 1999; 37: 2754-2770.

[43] Schmidt M, Maurer FHJ. Relation between free-volume quantities from PVT–EOS analysis and PALS. Polymer 2000; 41: 8419-8424.

[44] Dlubek G, Bamford D, Rodriguez-Gonzalez A, Bornemann S, Stejny J, Schade B, Alam MA, Arnold M. Free volume, glass transition, and degree of branching in metallocene-based propylene/α-olefin copolymers: positron lifetime, density, and differential scanning calorimetric studies. J Polym Sci Polym Phys 2002; 40: 434-453.

[45] Lagaly G, Ziesmer S. Colloid chemistry of clay minerals: the coagulation of montmorillonite dispersions. Adv Colloid Interface Sci 2002; 100: 105-128.

[46] Carmezini G, Mackay ME, Sauer BB, Kampert W. Manipulation of hyperbranched polymers' conformation. Chem Mater 2002; 14: 819-825.

[47] Cheng SZD, Cao M-Y,Wunderlich B. Glass transition and melting behavior of poly(oxy-1,4-phenyleneoxy-1,4-phenylenecarbonyl-1,4-phenylene) (PEEK). Macromolecules 1986; 19: 1868-1876.

[48] Richardson MJ. In: Mathot VBF, editor. Calorimetry and thermal analysis of polymers. Munich: Hanser; 1993. 170-181.

[49] Kobayashi Y, Zheng W, Meyer EF, McGervey JD Jamieson, AM. Free volume and physical aging of poly(viny1 acetate) studied by positron annihilation. Macromolecules 1989; 22: 2302-2306.

[50] Kluin JE, Yu Z, Vleeshouwers S, McGervey JD, Jamieson AM, Simha R. Ortho-positronium lifetime studies of free volume in polycarbonates of different structures: influence of hole size distributions. Macromolecules 1993; 26: 1853-1861.

[51] Chang, G. W.; Yu, Z.; Jamieson, A. M.; McGervey, J. D. Physical aging in the mechanical properties of miscible polymer blends. J Appl Polym Sci 1997; 63: 483-495.

[52] Kirkegard P.; Eldrup M.; Morgesen, OE.; Pedersen, NJ. Program system for analysing positron lifetime spectra and angular correlation curves. Comput Phys Commun 1981; 23: 307-335.

[53] Zagar E, Grdadolnkik J. An infrared spectroscopic study of H-bond network in hyperbranched polyester polyol. J Mol Struc 2003; 658: 143-152.

[54] Mackay ME, Carmezini G. Manipulation of hyperbranched polymers' conformation. Chem Mater 2002; 14: 819-825.

[55] Zagar E. Zigon M. Molar mass distribution of a commercial aliphatic hyperbranched polyester based on 2,2-bis(methylol)propionic acid. J Chromatogr A 2004; 1034: 77-83.

[56] McKenna GB. Ten (or more) years of dynamics in confinement: perspectives for 2010. Eur Phys J-Spec Top 2010; 189: 285-302.

[57] Grebowicz J, Lau SF, Wunderlich BJ. The thermal properties of polypropylene. J Polym Sci Polym Symp 1984; 71: 19-37.

[58] Suzuki H, Grebowicz J, Wunderlich BJ. Heat capacity of semicrystalline, linear poly(oxymethylene) and poly(oxyethylene). Macromol Chem 1985; 186: 1109-1119.

[59] Yu Z, Yahsi U, McGervey JD, Jamieson AM, Simha R. Molecular weight-dependance of free volume in polystyrene studied by positron annihilation measurements. J Polym Sci Pol Phys 1994; 32: 2637-2644.

[60] Choudalakis G, Gotsis AD. Free volume and mass transport in polymer nanocomposites. Curr Opin Colloid Interface Sci 2012; 17: 132-140.

[61] Wang Y-Q, Wu Y-P, Zhange H-F, Zhang L-Q, Wang B, Wang Z-F. Free volume of montmorillonite/styrene-butadiene rubber nanocomposites estimated by positron annihilation lifetime spectroscopy. Macromol Rapid Commun 2004; 25: 1973-1978.

[62] Wang ZF, Wang B, Qi N, Zhang HF, Zhang LQ. Influence of fillers on free volume and gas barrier properties in styrene-butadiene rubber studied by positrons. Polymer 2005; 46: 719-724.

[63] Nakanishi H, Jean YC. Dynamics of excess free volume in semicrystalline peek studied by positron annihilation. Macromolecules 1991; 24: 6618-6621.

[64] Nakanishi H, Jean YC. Positronium formation at free-volume sites in the amorphous regions of semicrystalline PEEK. J Polym Sci B 1989; 27: 1419-1424.

[65] Sano M, Murakami H, Ichimura K. Positronium in a layered-structure material: montmorillonite. J Radioanal Nucl Chem 1999; 239(2): 325-328.

[66] Eldrup M, Lightbody D, Sherwood NJ. The temperature dependence of positron lifetimes in solid pivalic acid. Chem Phys 1981; 63: 51-58.

[67] Tao SJ. Positronium annihilation in molecular substances. J Chem Phys 1972; 56: 5499-5510.

[68] Klonos P, Panagopoulou A, Bokobza L, Kyritsis A, Peoglos V, Pissis P. Comparative studies on effects of silica and titania nanoparticles on crystallization and complex segmental dynamics in poly(dimethylsiloxane). Polymer 2010; 51: 5490-5499.

[69] Chrissopoulou K. Andrikopoulos KS, Fotiadou S, Bollas S, Karageorgaki C, Christofilos D, Voyiatzis GA, Anastasiadis SH. Crystallinity and chain conformation in peo/layered silicate nanocomposites. Macromolecules 2011; 44: 9710-9722.

CHAPTER V

CONCENTRATION OF NANOSILICATE PLATELETS VIA INTERDIFFUSION IN POLYETHYLENE MULTILAYERS: EFFECTS ON CLAY MORPHOLOGY AND GAS BARRIER

This chapter was co-authored by Jeremy J. Decker, Kevin P. Meyers, Donald R. Paul, Anne Hiltner, and Sergei Nazarenko

Abstract

Interdiffusion of a polymer pair in microlayers was exploited to increase the concentration of nanoclay particles. When microlayers of a nanocomposite composed of organically modified montmorillonite ($M_2(HT)_2$) inside maleic anhydride grafted linear low-density polyethylene (LLDPE-g-MA) and low-density polyethylene (LDPE) were taken into the melt, the greater mobility of the linear LLDPE-g-MA chains compared to the branched LDPE chains caused shrinkage of the nanocomposite microlayers, concentrating the $M_2(HT)_2$ contained within. Analysis of the clay morphology within these layers demonstrated an increase in clay particle lengths and aspect ratios, which was attributed to the growth of skewed aggregates during concentration. The melt induced clay concentration and increased clay particle dimensions caused significant decreases in permeability of the nanocomposite microlayers and reduced the overall permeability of the multilayered films. Morphology and transport behavior of these microlayered films were compared to a series of bulk nanocomposites using a second LLDPE-g-MA containing $M_2(HT)_2$ with varying clay content.

Introduction

It is well established that the barrier properties of polymers can be increased by the inclusion of high aspect ratio inorganic platelets which alter the diffusion path of penetrant molecules. Various continuum models have been proposed to predict the permeability of platelet filled composites [1]. High aspect ratio fillers in nanocomposites (such as exfoliated clay) significantly decrease penetrant permeability both in theory and in practice dependent upon filler volume fraction and aspect ratio. In general, these models are based on random, parallel platelets oriented perpendicular to the permeation direction.

Theoretical predictions of gas diffusion through polymer composites containing disk shaped fillers suggest that the characteristic distance between the particles [2] will control barrier properties. Two possible filler concentration regimes are characterized by very different diffusion behavior. Under dilute particle conditions, the disks are spaced at a distance much exceeding the disk radius *R* and their volume fraction is much less than one. Here the contribution of the disks to the effective diffusivity of permeant are nearly independent and are best described by a tortuosity dependant model such as that derived by Nielsen [3].

At semidilute concentrations, the volume fraction of the disks is still much less than one, but they are spaced at distances comparable to or smaller than *R*. In this semidilute regime the physics of diffusion is dominated by the significant contribution of repeated multiple scatterings of penetrant molecules between the close pairs of disks. This adds considerably to the decrease in overall diffusivity of the composite in the

semidilute regime [2]. These changes in diffusivity in the semidilute regime diffusion are best described by the models derived by Cussler [4,5]

A typical high aspect ratio filler employed in composites is clay. The clay known as montmorillonite is a naturally occurring layered silicate consisting of platelets with an inner octahedral layer sandwiched between two silicate tetrahedral layers. In their natural state these platelets are water soluble, but the addition of surfactant molecules to the platelets through ion exchange creates organoclays which improves compatibility with a range of polymers. The use of layered silicates as fillers in polymers has attracted considerable interest due to the ability to achieve exceptional property enhancements at low loading levels [6].

For melt-processed polymer layered silicate nanocomposites, the stress field within the mixing device creates smaller particles from larger ones. It is expected in nanocomposites, where the polymer has an affinity for the organoclay, that higher clay loadings will increase the mixture viscosity and, therefore, the shear stresses during mixing [7]. These increased shear forces can induce clay platelets to peel apart in the nanocomposite melt [8]. In addition, these higher loadings increase the particle–particle interactions during mixing. The consequence of these combined effects is a decrease in particle length and often increased particle thicknesses, with the net effect of decreased particle aspect ratios. This means that property enhancements are not as large at higher loadings as would be expected from the trends observed at lower loadings. It would therefore be useful to find a means to increase clay concentration in nanocomposite systems without sacrificing particle lengths and aspect ratios.

A methodology exists to concentrate particulates under low shear conditions and is available through the use of multilayered miscible polymer films. Coextrusion processes exist that make it possible to form two (or more) polymers into microlayered arrays with hundreds, sometimes thousands, of alternating layers with individual layer thicknesses on the order of microns or less. Microlayering is an attractive approach for creating designed architectures from particulate-filled polymers [9-10]. If the particles are anisotropic, for example, platelets, flakes, tubes, or short fibers, then geometric constraints imposed by layer multiplying will orient the particles in the plane of the layers.

The stringent flow conditions required for microlayer coextrusion provide the opportunity to combine miscible polymers on a small scale with little or no mixing. Heating these multilayered structures into the melt state will activate interdiffusion between the miscible layers [11-12]. Work with microlayered polyethylene systems has demonstrated how the interdiffusion of the layers can produce convective flow similar to the Kirkendall effect in metals and cause alternating layers to shrink, if a mismatch in diffusion coefficients exists [13-14]. This occurs when highly mobile chains diffuse into a region of less mobile chains. The resulting osmotic pressure drives the bulk flow, causing the layer boundaries to move in the opposite direction of faster diffusing chains [15,16]. This shrinkage is caused by the conservation of density in the melt, as voids created from polymer migration into adjacent layers collapse. In addition, this process has been demonstrated to concentrate particulates trapped in the faster diffusing polymer layers. Microlayered systems consisting of layers of linear low density polyethylene (LLDPE) containing inorganic particulates and alternating unfilled low density

polyethylene (LDPE) layers demonstrated that the LLDPE preferentially diffused into the neighboring LDPE layers due to a mismatch in diffusion coefficients. This lead to the shrinkage of these LLDPE layers and the concentration of the particulates contained therein [17].

It should therefore be possible to create a layered film structure where composite layers containing flakes (nanoclay) in a concentrated regime are alternated with layers of an unfilled polymer. Layer interdiffusion could concentrate the nanoclay in microlayers under low shear conditions, thus also avoiding the decreases in aspect ratio typically observed with melt processing. Such a system may even offer superior barrier properties to a single evenly dispersed nanocomposite film with the same filler content if the clay concentrates significantly enough to reach the semi-dilute diffusion regime.

The purpose of this study is to examine the effects of layer interdiffusion upon a multilayered system containing nanocomposite layers generated using a maleic anhydride grafted LLDPE (LLDPE-g-MA) and surfactant modified montmorillonite (MMT) that are alternated with a conventional low-density polyethylene (LDPE). A detailed analysis of the effects of layer interdiffusion upon the organoclay filler particle morphology and oxygen barrier behavior is presented. For comparative purposes nanocomposites were generated utilizing a secondary LLDPE-g-MA with a broad range of clay loadings. Interdiffusion of the multilayers lead to concentration of the clay particles and an increase in barrier properties. Unexpectedly, this clay concentration through interdiffusion lead to an increase in clay particle aspect ratios, unlike the nanocomposite controls that were processed by twin-screw extrusion, where the aspect ratios decreased with increasing clay content.

Experimental

Materials

Table 6 summarizes the materials used in this study. The maleic anhydride grafted linear low density polyethylene (LLDPE-g-MA), designated herein as PEMA110 (Fusabond® E MX110D, donated by Du Pont), was chosen because of the high melt flow rate (MFI, 16.8g/10 min at 200°C, 2.16 kg), which decreased (to 4.9g/10 min at 200°C, 2.16 kg) with addition of nanoclay Cloisite 20A® (Southern Clay Products). This organoclay is prepared by a cation exchange reaction between sodium montmorillonite (Na^+MMT) and a two-tailed quaternary ammonium surfactant, dimethyl-bis(hydrogenated-tallow) ammonium chloride, and is designated herein as $M_2(HT)_2$. The low density polyethylene (Huntsman PE2030) was chosen for a MFR (5.2g/10 min at 190°C, 2.16 kg) similar to the PEMA110 nanocomposite. It was expected that the LDPE and the LLDPE-g-MA (PEMA110) used were miscible with each other based upon prior work with related polyolefins [18]. A second LLDPE-g-MA, designated as PEMA528 (Fusabond® E MB528D, donated by Du Pont), was chosen for its capacity to disperse larger loadings of $M_2(HT)_2$, and was used for comparative analysis. $M_2(HT)_2$ was selected based upon previous studies showing excellent dispersion with maleated polyolefins [19,20]. Much of the discussion will focus upon the inorganic montmorillonite layers, which will be designated as MMT, and any references to volume fractions of MMT must be understood to apply only to the inorganic portion.

Table 6

Materials Used in This Study

Material	Commercial designation	Specifications	Supplier	Utilized in this study for
Polymer				
LDPE	PE2030	MFR = 5.2 g/10 min at 200°C Density = 0.92 g/cm^3	Huntsman	Multilayer Films
LLDPE-g-MA (PEMA110)	Fusabond® E MX110D	MFR = 16.8 g/10 min at 200°C Density = 0.93 g/cm^3	DuPont	Multilayer Films
LLDPE-g-MA (PEMA528)	Fusabond® E MB528D	MFR = 4.2 g/10 min at 200°C Density = 0.92 g/cm^3	DuPont	Nanocomposite Films (bulk)
Nanoclay				
$M_2(HT)_2$	Cloisite®20A bis(hydrogenate-tallow) ammonium Montmorillonite	Organic content = 38 wt% d_{0001} = 25.1 Å Density (MMT) = 2.86 g/cm^3	Southern Clay Products	Nanocomposites bulk and microlayered

Melt Processing

The organoclay and the LLDPE-g-MA were dried for a minimum of 24 hours in a vacuum oven at 80°C and were cooled to room temperature under vacuum prior to melt

processing. Nanocomposites were melt compounded in a Prism TSE 16TC twin screw extruder using a barrel temperature of 200°C, a screw speed of 70 rpm, and maximal feed rate to generate kilogram quantities of pellets. For all nanocomposites generated, the LLDPE-g-MA and $M_2(HT)_2$ were hand-mixed and introduced into the extruder by a single hopper, which was blanketed in nitrogen gas to prevent water uptake. The extrudate was cooled in an ice water bath, pelletized, and dried at 80°C under vacuum for 2 hours. The dried pellets were reintroduced to the hopper and extruded again under the same conditions. This process was carried out four times for each nanocomposite generated, as it was found to optimize clay dispersion and provide consistent nanoclay content control. After final drying, the nanocomposite pellets were stored over desiccant. Film specimens were generated by melt pressing at 200°C and 3000 psi on a non-stick surface in a 1 mm thick mold for oxygen transport, WAXD, and TEM analysis. Montmorillonite content of the samples was confirmed by placing pre-dried nanocomposite films or pellets in a furnace at 900°C for one hour and weighing the remaining MMT ash, correcting for loss of structural water [8]. A series of compositional blends of PEMA110 and LDPE were also prepared (at varying volume fractions of PEMA110 in LDPE) by twin screw extrusion.

Microlayered Film Processing

Microlayer films composed of LDPE and PEMA110 nanocomposite (1.03% vol/vol MMT) with 65 alternating layers (exterior film layers of LDPE) were extruded in a 1:1 feed ratio using the microlayer coextrusion system described previously [21,22]. A sacrificial polystyrene layer was extruded on the outer surfaces of the multilayered films to prevent deformation of the polyethylene layers from internal stresses during cooling,

and was thereafter removed. The LDPE was chosen to prevent viscosity mismatch with the PEMA110 nanocomposite during processing, as they have similar MFR (5.7 and 5.3g/10 min at 200°C, respectively). The final microlayers films possessed an average thickness of 334 microns (after removal of the sacrificial layer), and were stored over desiccant. Layer composition was confirmed from MMT ash, OM, and TEM.

Annealing of Multilayers

The microlayer films composed of LDPE and PEMA110 nanocomposite were annealed at 200°C under nitrogen atmosphere in a melt press. Film specimens were annealed on non-stick surfaces and confined in a mold specifically fabricated to match the film thickness. Films were carefully cut to fit these molds in order to prevent distortion of the film dimensions during annealing. Pressure applied was under 50 psi, as confinement, not compression, was the objective. A constant nitrogen flow was provided around the melt press platens to reduce oxidative degradation. After annealing, the films were quenched in ice water, dried, and stored over desiccant.

Characterization

One dimensional X-ray diffraction spectra were collected on a Rigaku Ultima III diffractometer (Cu Kα radiation, $\lambda = 1.542$Å) at room temperature using Bragg-Brentano parafocusing geometry (reflection mode XRD) on the sample films. Melt flow rates were determined according to ASTMD1238 using a Dynisco melt indexer at 200°C with applied weights of 2.16 kg and 5.0 kg.

Oxygen barrier of nanocomposite films and controls were measured at 25°C, 0% RH, and 1 atm partial oxygen pressure difference using a commercially manufactured diffusion apparatus OX-TRAN® 2/21 ML (MOCON). This instrument employs a

continuous-flow method (ASTM D3985-81 and ASTM F1249-01) with nitrogen as the carrier gas to measure oxygen flux, J(t), through polymeric films. The film specimens were carefully conditioned in the instrument, as described previously [23]. The permeability coefficient, P, was calculated directly from the steady-state flux, J_∞, value as $P = J_\infty l/\Delta p$.

For the optical microscopy (OM) analysis of the multilayered films, 5 μm thick sections were microtomed perpendicular to the film surface using a glass knife. Phase contrast images were captured on film and the layer thicknesses were determined by image analysis utilizing Digimizer Version 4.2.4.0. Changes in layer thickness of the annealed microlayered samples were quantified utilizing the image analysis of OM data.

For transmission electron microscopy (TEM) 90 nm thick sections were cut at T = -100°C in the direction perpendicular to the film surface using a Leica cryo-ultramicrotome FC6 and a cryogenic diamond knife, where they were deposited on a copper grid. The sections were imaged using a Zeiss 109T TEM operated at an accelerating voltage of 80 kV under bright field conditions. Since the MMT layers have a higher electron density than the surrounding polymer matrix, they appear darker in the images.

Particle Analysis

Particle analysis was used to confirm and quantify clay layer concentration with annealing and to measure the length and width of the observed MMT particles dispersed in the matrix. For both methods of TEM image analysis, micrographs were chosen at 20K magnification, which allowed sufficient resolution to observe individual clay sheets as well as providing a suitable area from which to extract a large population sampling.

Clearly focused and well stigmated micrographs were utilized since image clarity and resolution were critical to this analysis, especially for individual sheets of MMT, which due to their nanoscale dimensions, can be difficult to discriminate from the polymer matrix.

For the analysis of MMT concentration Adobe Photoshop® was utilized. For multilayered sample images, thin lines were drawn straight from one nanocomposite layer boundary to the other, perpendicular to the microlayer edge. Since the clay particles were largely aligned in the flow direction, this prevented the measuring lines from crossing the same particles repeatedly. For the bulk nanocomposites, these lines were drawn such that they were as perpendicular as possible to the primary alignment of the clay particles. These lines were then measured in microns, and every resolvable clay layer (sheet) that intersected the line was counted. This analysis provided a linear particle density expressed in terms of MMT sheets per micron (S/μm). To ensure statistical validity of the analysis, 323-1176 particles were counted over distances of 11-51 μm.

The individual clay particle dimensions were determined using the following methodology. A high resolution rectangular area of the micrograph was chosen from the edge of the clay containing microlayer to the middle of the same microlayer. Within this designated area, each and every discernible clay layer was traced using Adobe Photoshop. These tracings were saved separately in bitmap format and imported into the image analysis program, Digimizer 4.2.4.0, where the clay particle characteristic dimensions were measured. Particle length was determined as the end to end distance. Particle thickness was determined by dividing the particle into six equidistant sections,

and five thickness measurements were taken at these divisions to average the particle thickness. For clay particle sections consisting of a single MMT layer, the thickness could not accurately be measured due to resolution limitations and were assigned a thickness of 1 nm, corresponding to the thickness of an individual MMT sheet [24]. To achieve statistical validity in this analysis, 476-975 particles were measured for length and thickness per sample.

Results and Discussion

Bulk PEMA528 Nanocomposite Morphology

The degree of clay dispersion, e.g., exfoliated, agglomerated (or both), and the dimensions of the clay particles have a significant effect on the properties of polymer-clay nanocomposites. The morphology of the clay in the PEMA528 bulk nanocomposites, prepared by direct twin screw extrusion, was explored by TEM as discussed in the experimental section.

Representative TEM micrographs of the PEMA528 nanocomposites with increasing clay content are shown in Figure 37. As can be seen from these micrographs, the organoclay dispersed well in the LLDPE-g-MA and highly delaminated clay layers are present at all clay loadings. With increasing MMT content, a decrease in particle length (2R) was observed and the particle thickness, a, was observed to vary with each composition. These decreases in particle length with increasing MMT content were consistent with previous work utilizing maleated polyolefin/organoclay nanocomposites [7,25,26]. The results from the image analysis of the clay particle lengths and thicknesses are shown in Table 7 in terms of volume fraction MMT.

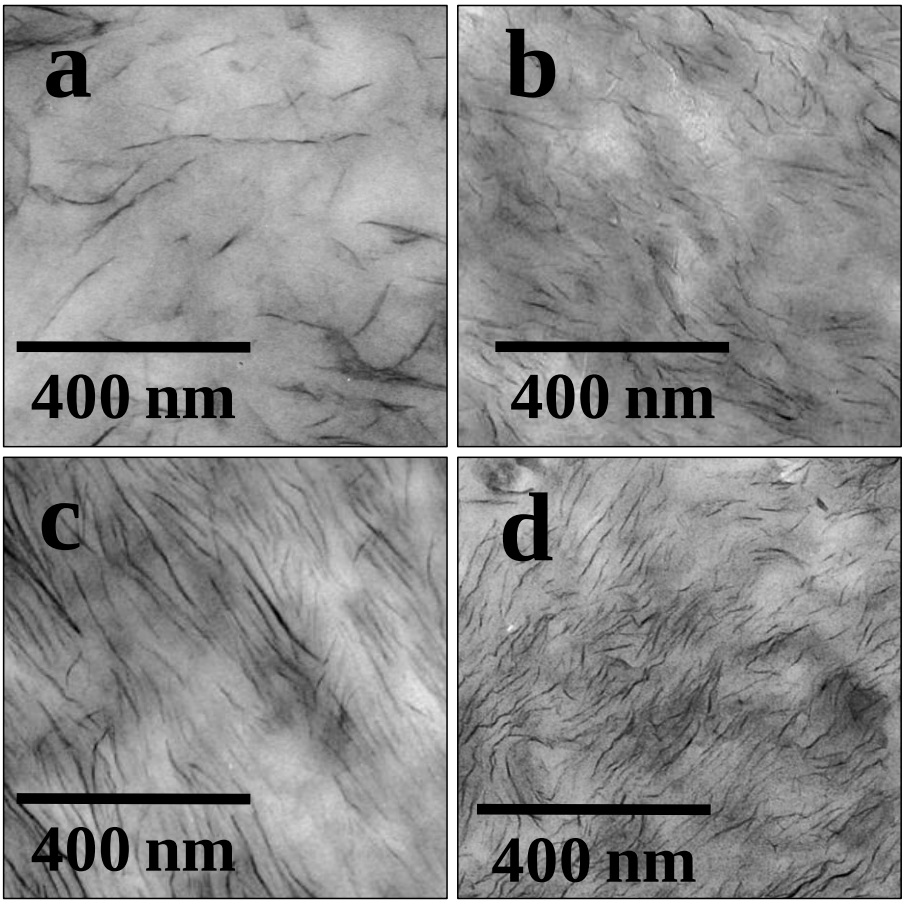

Figure 37. Representative TEM micrographs of clay morphologies in bulk nanocomposite films with the following concentrations: (a) 1.02% vol/vol MMT, (b) 2.08% vol/vol MMT, (c) 3.19% vol/vol MMT, (d) 4.35% vol/vol MMT.

A series of histograms generated from the particle analysis data for the PEMA528 nanocomposites are shown in Figure 38. As can be seen from these histograms, the individual ½ particle length, R_i, decreased with increasing MMT content, and the distribution of R_i also narrowed. The individual particle thickness, a_i, did not change significantly with MMT content. Individual particle aspect ratios, α_i, decreased with increasing MMT content, and the distribution narrowed. The decrease in particle aspect ratios with increasing clay content is consistent with previous findings and is attributed to

both the viscosity increases and increased particle-particle interactions during processing [7].

Table 7

PEMA528 Nanocomposites TEM Image Analysis Data

MMT volume fraction (vol/vol)	Total number of particles measured	Number average ½ particle length and standard deviation (*R*, nm)	Average particle thickness and standard deviation (*a*, nm)	Number average aspect ratio and standard deviation (α)
0.0102	686	45.7 ± 29.9	1.7 ± 0.7	28.5 ± 15.7
0.0208	476	33.5 ± 21.8	1.4 ± 0.5	24.0 ± 13.7
0.0319	975	37.0 ± 26.8	1.8 ± 0.6	20.6 ± 13.4
0.0435	908	24.3 ± 15.9	1.7 ± 0.6	13.5 ± 7.3

It has been demonstrated with maleated polyolefin systems that as the content of (well dispersed) nanoclay is increased the melt viscosity of the nanocomposite increases [7,27]. Indeed, with the PEMA528 systems employed in this study, this MFR decreased dramatically with clay content, indicating large increases in viscosity, from 10.8 g/10 min for the pure PEMA528 to 2.3 g/10 min at 0.0101 vol/vol MMT, to 0.3 g/10 min at 0.0208 vol/vol MMT, with an applied weight of 5.0 kg at 200°C. At the higher clay contents, the viscosity was too high to measure MFR at this temperature. Increased melt viscosities transfer more stress, during processing, helping to achieve the separation of organoclay platelets, which also reduces clay particle lengths, whereas lower melt viscosities may serve to merely skew stacks of platelets, leading to longer clay particles. [8]. In these PEMA528 systems, increases in clay content lead to much higher viscosities, which caused additional shear, and the skewed aggregates typically observed became shorter with increased clay content, decreasing the aspect ratios.

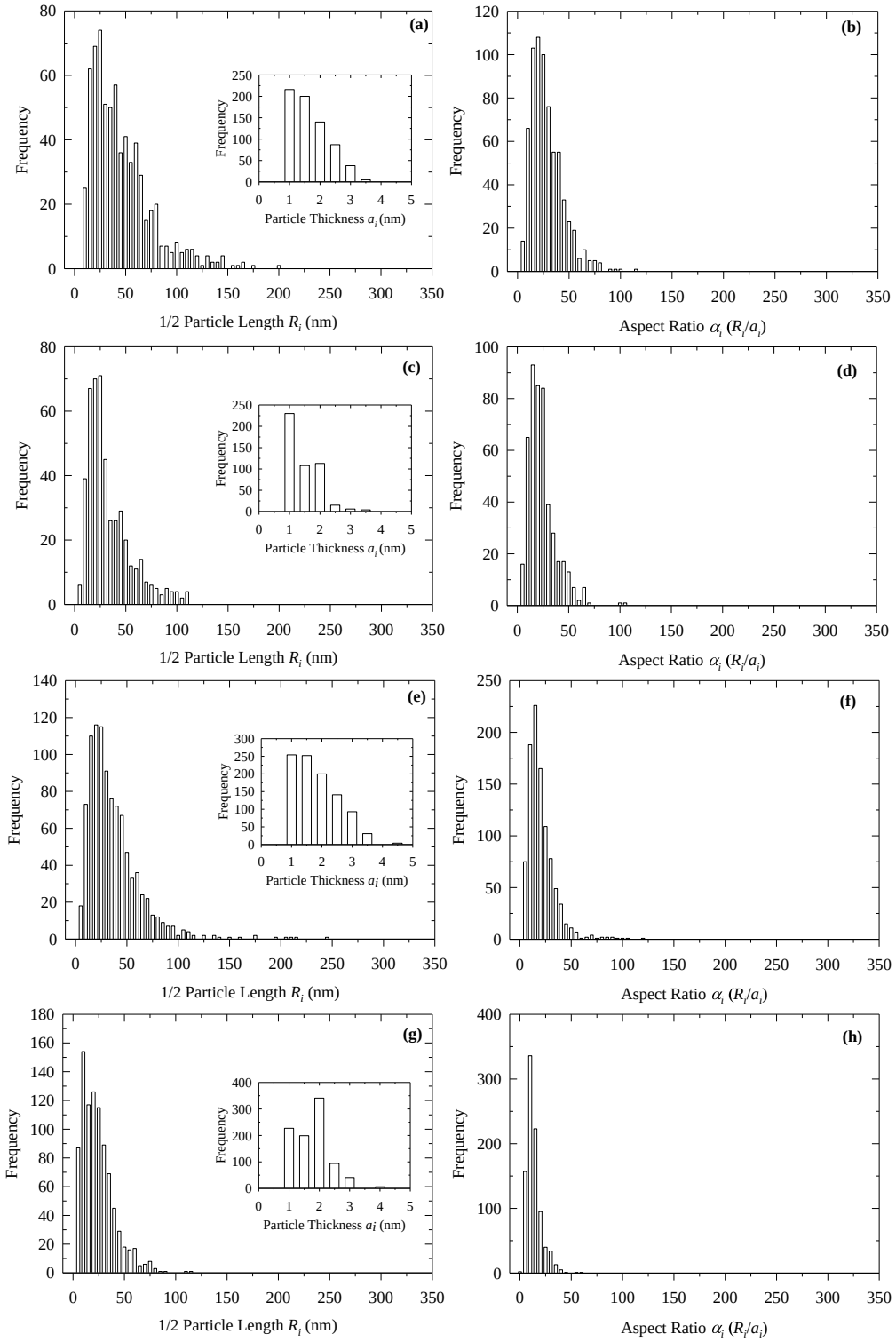

Figure 38. Histograms from TEM analysis of individual MMT particles in PEMA528 nanocomposites. Frequency plots represent ½ particle length R_i with particle thickness a_i, and the individual particle aspect ratios α_i. Plots arranged as follows: (a,b) 1.02 % vol/vol MMT, (c,d) 2.08% vol/vol MMT, (e,f) 3.19% vol/vol MMT, (g,h) 4.35% vol/vol MMT.

X-ray diffraction is commonly used to characterize the exfoliation structure in nanocomposites. WAXD scans of the bulk nanocomposite samples generated with PEMA528 are shown in Figure 39. For comparative purposes, virgin PEMA528 and dry $M_2(HT)_2$ are included in the figure. The lack of any clear d_{001} peak in the PEMA528 nanocomposites is in agreement with the largely exfoliated state observed by TEM.

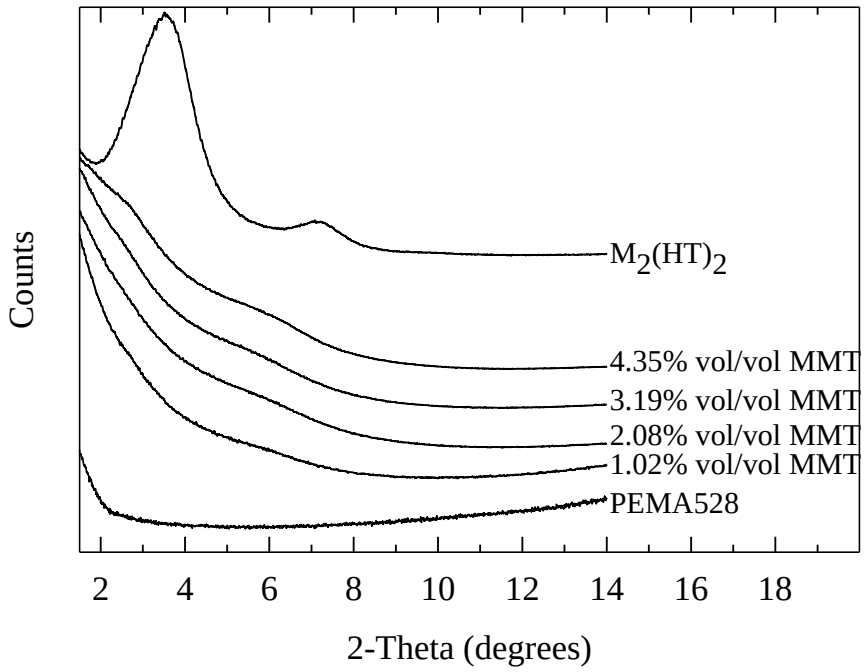

*Figure 39.*WAXD scans of pristine dried organoclay $M_2(HT)_2$ and bulk nanocomposites generated with $M_2(HT)_2$ in PEMA528. Curves vertically offset for clarity.

Although these nanocomposite systems do possess very well dispersed clay particles, even for the best dispersed nanocomposites (such as nylon6), exfoliation is generally never complete, and one can see clay particulates which consist of two or more platelets [28]. Indeed, clay platelets may be skewed relative to one another with face-to-face interactions so that the clay particle lengths are longer than the individual MMT platelet lengths as shown in Figure 40 [29]. This face-to-face behavior is evident in the high magnification micrographs for both the PEMA528 nanocomposite (1.02% vol/vol

MMT) and the PEMA110 nanocomposite layers (1.03% vol/vol MMT) of the pre-annealed multilayered films. The clay particulates possessed a variety of lengths, and the skewed behavior of the individual MMT platelets, which comprise the clay particles, was observed.

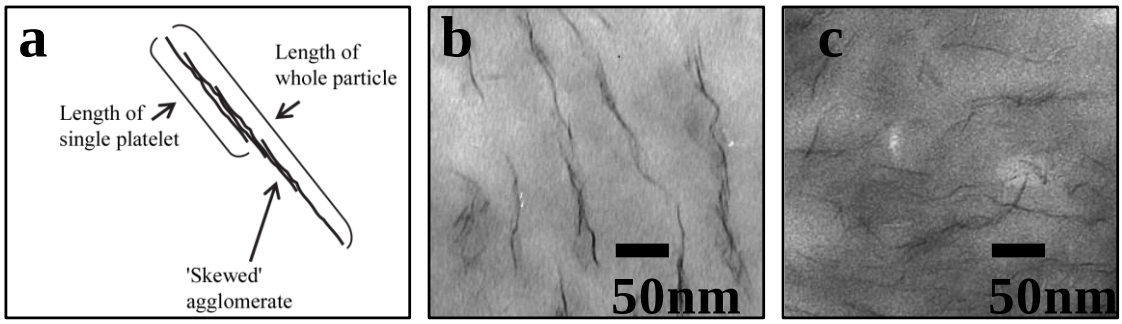

Figure 40. Examples of clay particle distributions at higher TEM magnifications. (b) 1.02% vol/vol MMT in bulk composite. (c) 1.03% vol/vol MMT in nanocomposite layer of pre-annealed multilayer film.

Indeed, this skewing behavior was present to some degree for each nanocomposite analyzed. With the PEMA528 nanocomposites, these skewed aggregates grew shorter as MMT content increased. In the following sections, we address how the induced particle concentration effect from annealing of the multilayered nanocomposite films affected the clay particle morphology in the PEMA110 nanocomposite microlayers.

Changes in Layer Thicknesses of Multilayered Nanocomposites with Annealing

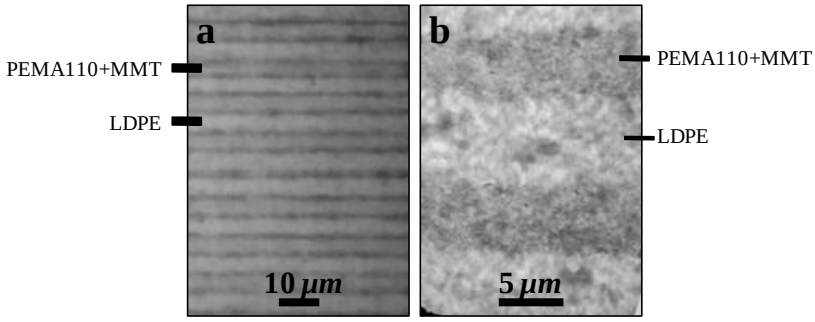

Figure 41. Representative micrographs of as received multilayered films from microlayer coextrusion: (a) by OM and (b) by TEM.

Creating a net flux of polymer out of the particle filled microlayers, in order to shrink these layers and concentrate the clay particulates within, required a polymer pair with specific processing characteristics. The microlayered pair of the PEMA110 nanocomposite with unfilled LDPE met the requirements that the polymers be miscible in the melt (in order to interdiffuse) and have melt viscosities close enough to process into well ordered microlayers. Incorporating $M_2(HT)_2$ into the PEMA110 caused the MFR to decrease from 16.8 g/10 min to 4.9 g/10 min, which was very close to the MFR of 5.2 g/10 min possessed by the LDPE at 200ºC, with 2.16 kg applied weight. An optical and TEM micrograph of the as received multilayered nanocomposite films are shown in Figure 41. Initial PEMA110 nanocomposite layer thicknesses were 5.25 ± 1.42 μm and initial LDPE layer thicknesses were 5.03 ± 1.50 μm in the as received multilayered films.

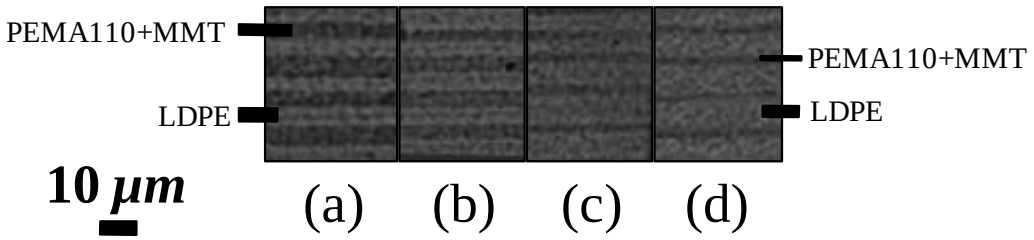

Figure 42. Optical Micrographs of the multilayered films after annealing at 200°C for the time indicated: (a) 0 min, (b) 5 min, (c) 15 min, (d) 25 min.

Being a nanoscale filler, the MMT was not visible by OM, but the microlayers could themselves be distinguished. Upon annealing it was observed that the filled PEMA110 layers thinned and the LDPE layers expanded, indicating that PEMA110 chains had diffused preferentially into the LDPE layers. The net outward-flux of PEMA110 caused the filled microlayers to shrink and concentrated the nanoclay within these microlayers. Optical micrographs in Figure 42, show representative images of the microlayered systems (PEMA110-nanocomposite/LDPE) after confinement in the melt at

200°C for various periods of time. For the purposes of this chapter, we assume that the diffusion occurs solely from the LLDPE-g-MA layer into the LDPE layer. When one considers that the LDPE has a highly branched backbone structure, and LLDPE-g-MA is linearly composed, it is reasonable that due to structural constraints, the most mobile polymer will be that which is more linear: the PEMA110.

Table 8

Optical microscopy Analysis Data for Multilayered Films Annealed at 200°C

Anneal Time (min)	Average nanocomposite layer width (μm)	Average LDPE layer width (μm)	Volume fraction of nanocomposite microlayers ($\varphi_{NanoLayer}$)	Concentration factor (*CF*)	Volume fraction of PEMA110 in LDPE microlayers
0	5.25 ± 1.42	5.03 ± 1.50	0.51	1.00	0
5	3.00 ± 0.66	6.91 ± 1.01	0.30	1.75	0.3
15	2.49 ± 0.60	8.06 ± 1.70	0.24	2.11	0.36
17	2.14 ± 0.55	8.08 ± 1.92	0.21	2.45	0.38
25	1.27 ± 0.19	8.49 ± 1.70	0.13	4.13	0.44

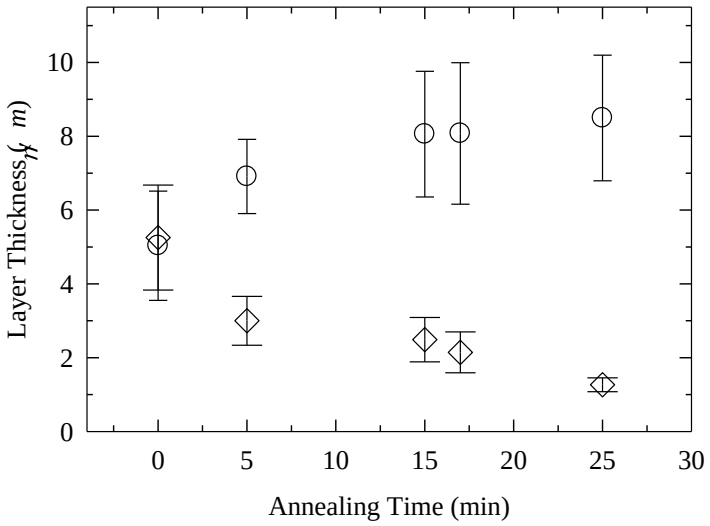

Figure 43. Changes in the average layer thickness of the multilayered films with annealing time at 200°C. (◇) PEMA110 nanocomposite layers. (○) LDPE layers.

Table 8 shows the changes in layer thickness for the multilayers with annealing at 200°C. Image analysis of the average layer thicknesses with time are plotted along with their standard deviations in Figure 43. The volume fractions of the nanocomposite layers in the total film ($\varphi_{NanoLayer}$) were determined from the average layer thicknesses. From the bulk volume fractions of the PEMA110 microlayers ($\varphi_{NanoLayer}$), one can calculate the fraction of PEMA110 that has migrated into the LDPE layers ($\varphi_{PEMA110}$). Since the clay remains within the PEMA110 layers, its concentration will directly correlate with the shrinkage of these layers. We represent this concentration by the concentration factor (*CF*), which represents the initial nanocomposite layer thickness divided by the annealed thickness. From this analysis, the clay concentrated in the PEMA110 layers by a maximum CF of 4.13 at 25 minutes. At longer annealing times the films visibly degraded and were not further explored.

Clay Concentration Measured by TEM in Nanocomposite Systems

Particle analysis was used to confirm and quantify clay layer concentration in TEM micrographs. Representative TEM micrographs of the multilayered nanocomposite films are ordered in terms of annealing time (Figure 44) to demonstrate the changes in layer thickness as observed by TEM. It must be noted that the clay particles remained within the PEMA110 matrix upon annealing and subsequent layer shrinkage.

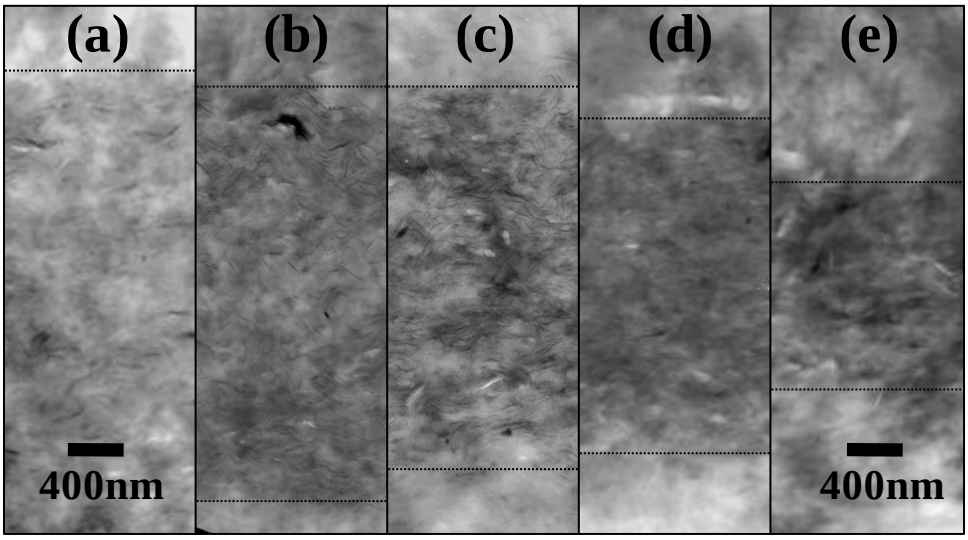

Figure 44. TEM micrographs of PEMA110 microlayers containing MMT. Designated by annealing times at 200°C. Dotted lines are to aid viewer in distinguishing layer boundaries: (a) 0 min-layer extends beyond figure, (b) 5 min, (c) 15 min, (d) 17 min, (e) 25 min; 400 nm scale bars apply to entire figure.

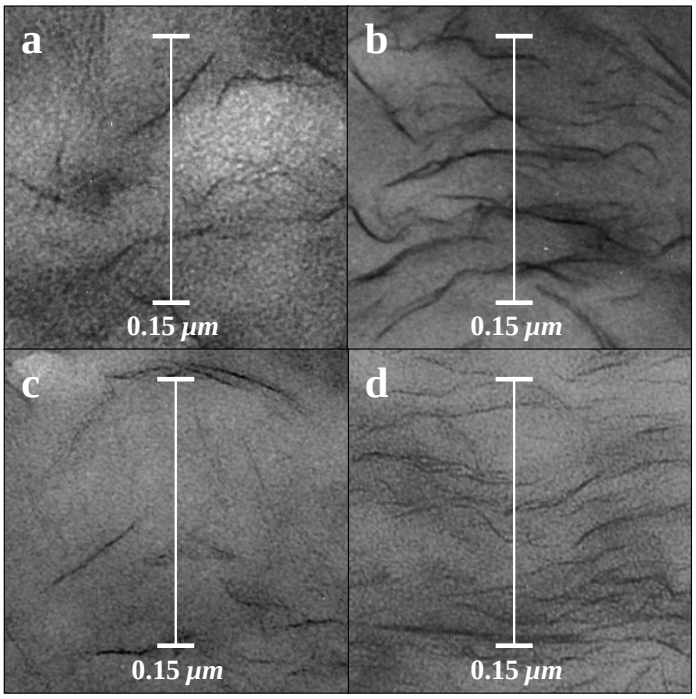

Figure 45. High magnification images of MMT layers in nanocomposites. (a) As received nanocomposite PEMA110 microlayer (1.03% vol/vol MMT). (b) Nanocomposite PEMA110 in microlayer after 25 min anneal at 200°C (*CF* of 4.13, 4.26% vol/vol MMT). (c) Bulk PEMA528 nanocomposite (1.02 % vol/vol MMT). (d) Bulk PEMA 528 nanocomposite (4.35 % vol/vol MMT).

High magnification images of both the bulk PEMA528 nanocomposite controls and the multilayered films are shown in Figure 45 to demonstrate clay concentration changes. Linear particle densities in terms of MMT sheets/micron (*S/μm*) were determined as previously described. Results for the microlayered PEMA110-nanocomposite/LDPE films are shown in Table 9, and the results for the PEMA528 bulk nanocomposites are shown in Table 10. The linear particle densities vs. volume fraction MMT for both systems are depicted in Figure 46, and a linear trend is observed. Volume fraction of MMT for the microlayers was determined by multiplying the concentration factor (*CF*) by the initial MMT concentration of 0.0103 (φ_{MMT}). As can be seen in Figure 46, there is good correlation between *S/μm* and φ_{MMT} for both the multilayered nanocomposite microlayers and the bulk control nanocomposites.

Table 9

Multilayered Composites TEM Image Analysis Data

Annealing time at 200ºC (min)	Total number of discrete clay layers intersected	Total line distance tracked (*μm*)	Linear particle density (*S*/*μm*)	Anticipated (*S*/*μm*) based upon concentration factor (*CF*) estimate
0	990	50.71	19.5 ± 3.2	19.5
5	870	27.69	31.5 ± 1.9	34.2
15	1004	24.31	41.3 ± 4.7	41.2
17	1150	23.45	49.0 ± 6.2	47.8
25	1176	14.07	83.6 ± 8.8	81.0

Linear Particle Density (S/*μm*).

Table 10

PEMA528 Nanocomposites TEM Image Analysis Data

MMT volume fraction in bulk nanocomposite	Total number of discrete clay layers intersected	Total line distance tracked (μm)	Linear particle density ($S/\mu m$)	Anticipated ($S/\mu m$) based upon MMT concentration
0.0102	323	17.76	18.2 ± 3.6	18.2
0.0208	557	15.96	34.9 ± 5.2	37.2
0.0319	598	11.91	50.2 ± 4.8	57.0
0.0435	798	11.01	72.5 ± 6.2	77.8

Linear Particle Density (S/*μm)*.

The PEMA528 nanocomposite controls were utilized to confirm the validity of the technique, as they possessed clearly defined MMT concentrations. For these the observed *S/μm* trends are close to those anticipated from the known changes in MMT content relative to the observed *S/μm* at 1.02% vol/vol MMT, as seen in Table 10.

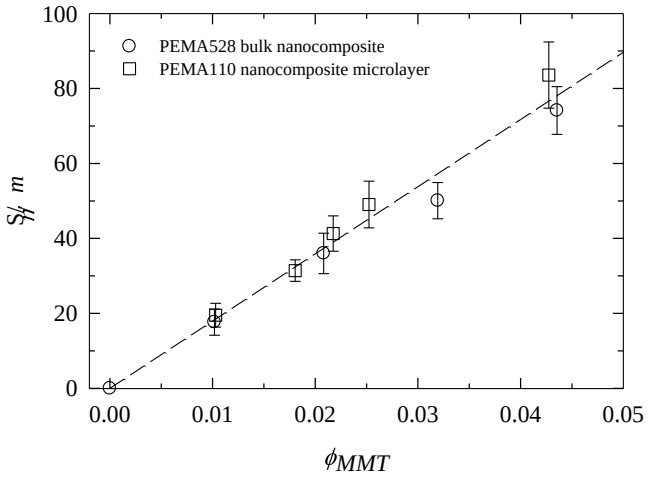

Figure 46. MMT sheets observed per micrometer (*S/μm*) in nanocomposite films plotted as a function of volume fraction MMT. φ_{MMT} for multilayered films determined from concentration factor (*CF*) multiplied by the initial PEMA110 microlayer MMT concentration of 0.0103.

This analysis demonstrated that the clay layers had, indeed, concentrated in the nanocomposite layers of the annealed multilayered films. Quantifying in this manner allowed for certainty that the layer shrinkage did not occur due to the layer *leaking* out of the film while it was being annealed. However, this analysis does raise an interesting point, especially when one looks more closely at the $S/\mu m$. For the PEMA110/MMT nanocomposite at time zero, $L/\mu m$ = 19.5, corresponding to 19.5 clay layers per micron (1000nm). Since each discrete MMT sheet is ~1nm thick, this translates to 19.5 nm/1000nm and corresponds to a volume fraction of 0.019. The same behavior is observed with the PEMA528/MMT nanocomposite, where 18.2 $L/\mu m$ corresponds to 18.2 nm/1000nm or a volume fraction of 0.018. In both of these systems, the linear particle density overestimates the clay concentration almost by a factor of two. This could be an indication that the dimensions of the clay particles were smaller than the 90 nm sectioned, which would have allowed a larger sampling of clay sheets to be imaged at different depths within the microtomed sections. Indeed, for the previous TEM image analysis of the PEMA528 nanocomposites, it was observed that a significant population of the clay particles has dimensions for 2R smaller than 90 nm (Figure 38).

Microlayered PEMA110 Nanocomposite Morphology

Representative TEM micrographs of the PEMA110 nanocomposite microlayers in the multilayered films (at various annealing times) are shown in Figure 47. Observation of these microlayers showed well dispersed and delaminated clay (at each annealing time) throughout the nanocomposite layers. A series of histograms (Figure 47) was generated from the particle analysis data for the annealed multilayered films containing the PEMA110 nanocomposite. As can be seen from these graphs, the average individual

½ particle length, R_i, increased with annealing time and the distribution of the lengths significantly broadened. The particle thicknesses, a_i, increased only modestly, which resulted in a net increase in the individual aspect ratio, α_i, of the clay particles with annealing time. The distribution of the individual aspect ratios also broadened with annealing time.

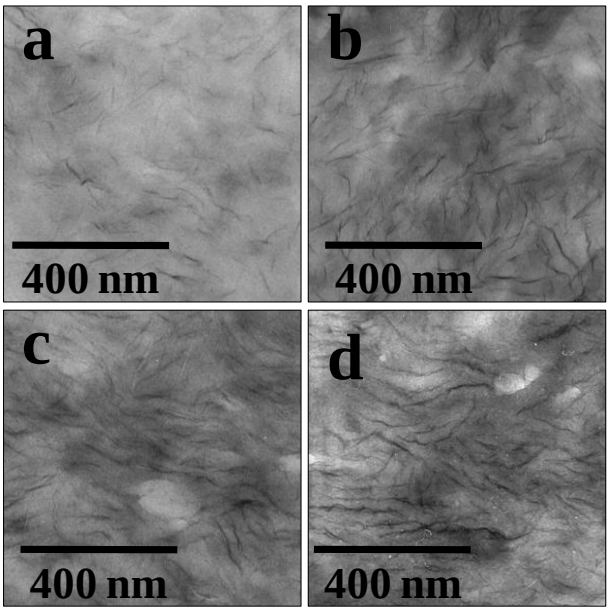

Figure 47. Representative TEM micrographs of clay morphologies in multilayered nanocomposite films at annealing times of (a) 0 min, (b) 5 min, (c) 15 min, (d) 25 min.

The results from the analysis of the particle lengths and thicknesses are shown in Table 11. Volume fractions of MMT are reported based upon the concentration factor (*CF*) observed by layer shrinkage measurements (OM) and confirmed by *S/μm* measurements (TEM), so that the volume fraction of MMT equals the *CF* multiplied by 0.0103 (the initial volume fraction of MMT in the nanocomposite microlayers before annealing). Average half particle lengths, *R*, were observed to increase with annealing, as did the average aspect ratios, α, and are reported along with their standard deviations.

Due to the increase in the distribution of the ½ particle lengths, R_i, the standard deviations for R increased with annealing time.

Table 11

Multilayered Nanocomposites TEM Image Analysis Data

Annealing time at 200ºC (min)	Total number of particles measured	φ_{MMT} in nanolaye (vol/vol)	Average ½ particle length (R, nm)	Average particle thickness (a, nm)	Average aspect ratio (α)
0	470	0.0103	35.9 ± 17.0	1.3 ± 0.5	29.9 ± 15.7
5	907	0.0180	46.7 ± 23.5	1.5 ± 0.5	36.6 ± 24.8
15	725	0.0217	68.2 ± 41.3	1.5 ± 0.5	46.6 ± 28.4
17	829	0.0253	72.7 ± 46.7	1.5 ± 0.5	52.9 ± 34.0
25	471	0.0426	86.9 ± 47.3	1.7 ± 0.5	54.5 ± 30.0

This behavior is in stark contrast to that seen with the PEMA528 nanocomposite controls prepared by twin-screw extrusion. In the bulk nanocomposites, particle lengths, and aspect ratios were seen to decrease with increasing volume fraction of MMT, attributed to increased shear forces during processing. However, in the multilayered nanocomposite systems, MMT concentration was achieved by a very different route. In these systems, annealing lead to the interdiffusion of the PEMA110 into the adjacent LDPE layers, which resulted in the shrinking of the nanocomposite layers and subsequently caused the clay particle concentration. Unlike with the direct twin-screw processing of the PEMA528 nanocomposites, when the multilayers were annealed, both particle lengths and aspect ratios increased. Since the concentration of the nanocomposite microlayers was not achieved by a high shear process, the clay layers did not experience

the shear forces which would prevent face-to-face interactions. The clay simply concentrated as the LLDPE-g-MA chains gently diffused out of the layers.

Concentration brought the clay particles closer together as the polymer around them vacated the microlayer. Under these conditions, the randomly distributed clay particles could impinge upon one another, as they were concentrated and approached one another from their randomly distributed positions. Thus, incidental impingement resulted in the formation and elongation of skewed aggregates (Scheme 3). Indeed, this was very apparent with the elongated clay particulates. They were composed of numerous clay sheets that had overlapped at the edges, such that they became longer than the individual sheet lengths. Clay sheets that were completely exfoliated and not part of a skewed aggregate structure, generally possessed lengths ($2R$) under 50 nm in length, as supported by the histograms for both nanocomposite systems and the high magnification TEM images provided. This observation correlated with the linear particle density results obtained in the previous section. Many of the clay layers possessed dimensions smaller than the thickness of the microtomed section, which explained why the $S/\mu m$ results were higher than expected. Since the microtomed sections were ~90nm thick, and the dimensions of a large portion of the clay particles were smaller than 50 nm in total length, the number of observed clay layers by TEM were naturally higher than expected based upon the volume concentration of clay, since the clay sheets were consistently oversampled.

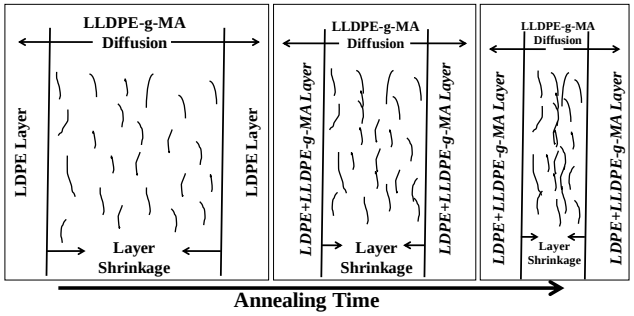

Scheme 3. Representation of proposed method of clay aggregate growth from incidental contact of clay layers as concentration increased during nanocomposite microlayer shrinkage.

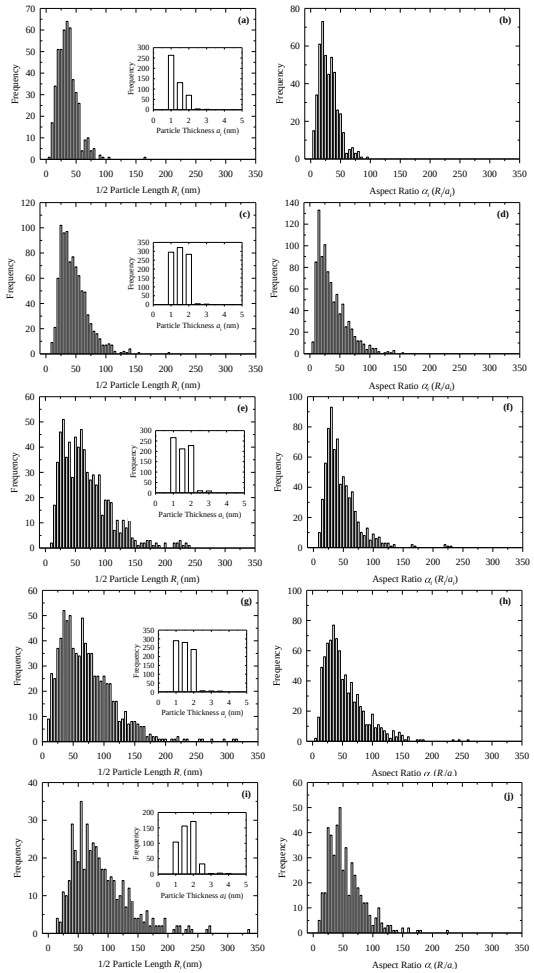

Figure 48. Histograms from TEM analysis of individual MMT particles in multilayered films with annealing time. Frequency plots represent ½ particle length, R_i, and particle thickness, a_i, and the individual particle aspect ratios, α_i. Plots are arranged as follows: (a,b) 0 min, (c,d) 5 min, (e,f) 15 min, (g,h) 17 min, (i,j) 25min.

It should also be noted that although the PEMA110 nanocomposite had a MFR of 4.9 g/10min at 200°C, this was due to an increase in melt flow viscosity from the virgin PEMA110 (MFR of 16.8 g/10 min at 200°C). Under the conditions of annealing utilized here, the nanocomposite layers were not exposed to viscosity increases from creep or flow induced shear, which are induced by the frictional interactions between silicate sheets [27]. Therefore, it is expected that the only impediment the nanoclay would have provided to interdiffusion would be from physical tethering or obstruction. Tethering could potentially occur from enthalpic interactions between the clay surfaces or surfactant with the polar functionally of the nearby LLPDE-g-MA chains. The clay would also be expected to obstruct transport of the polymer chains during interdiffusion by increasing the length of the diffusion path to the adjacent LDPE layer, an effect that would be expected to increase with clay particle concentration and increased aspect ratios. However, these effects were clearly unable to prevent the process of interdiffusion from occurring within the multilayered systems over the timescales studied.

X-ray diffraction was employed to confirm the TEM observations. WAXD scans of the multilayered nanocomposite systems are shown in Figure 49. For comparative purposes virgin PEMA110, dry $M_2(HT)_2$, and a 50/50 blend of PEMA110 with LDPE are included in the figure. Both the PEMA110 nanocomposite and the multilayered films generated from it lacked any clear d_{001} peak, indicating a high degree of exfoliation. There were no observable changes in clay morphology by XRD from the annealing process, indicating that the clay layers did not reagreggate into tactoid structures. This was expected based upon observations by TEM, for even as skewed aggregates formed,

they did not possess the long range stacking order necessary for coherent basal reflections to arise.

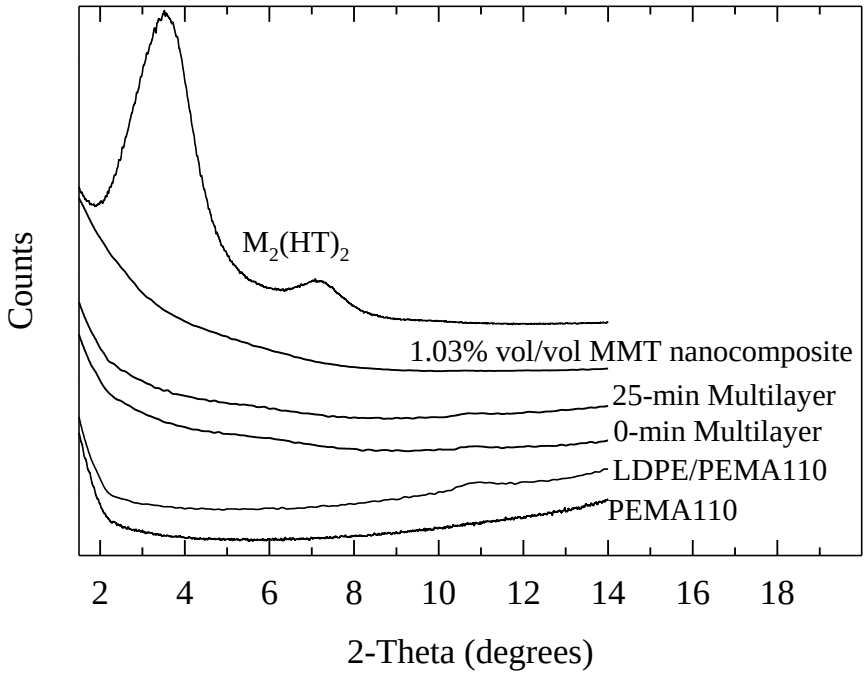

Figure 49. WAXD scans of multilayered nanocomposite films generated with $M_2(HT)_2$ in PEMA110 and their polymer components. Curves vertically offset for clarity.

Oxygen Permeabilities for the Nanocomposite Systems.

Figure 50 shows the oxygen permeabilities, P, of the PEMA528 nanocomposite control films with % volume fraction MMT. The PEMA528 control films showed a decrease in permeability with increasing clay content from an initial value of 16.59 cc(@STP)cm/(m^2dayatm) for the pure PEMA528 to 4.98 cc(@STP)cm/(m^2dayatm) at the maximum MMT loading of 4.35 % vol/vol. This corresponds to a relative permeabilty, P/P_0, of 0.30 at this clay loading.

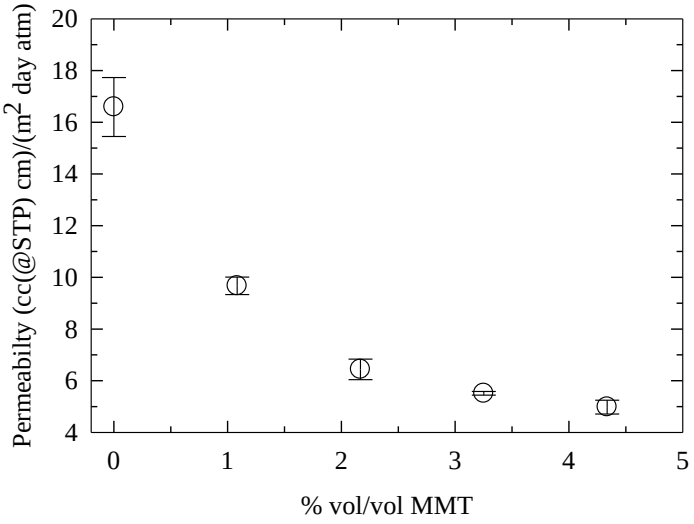

Figure 50. Permeability of bulk PEMA528 nanocomposite films with MMT content.

Figure 51 shows the oxygen permeabilities, *P*, of the multilayered PEMA110 nanocomposite/LDPE films with annealing time at 200°C. These films showed a decrease in oxygen permeability with annealing time from the initial value of 8.13 cc(@STP)cm/(m^2dayatm) for the as received mutlilayered films to 4.89 cc(@STP)cm/(m^2dayatm) for the multialyered films after 25 minutes of annealing. This corresponds to a 40% decrease in permeabilty, relative to the as received films.

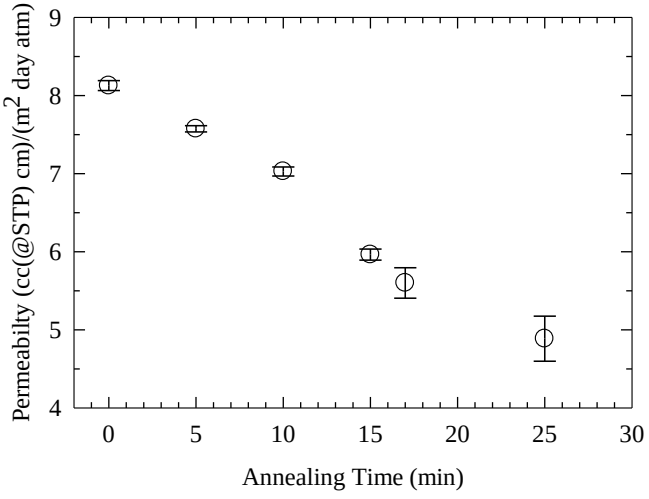

Figure 51. Permeability of multilayered films with annealing time at 200°C.

For the multilayered systems, the oxygen permeability decreased with annealing time as the PEMA110 nanocomposite layers became thinner from the interdiffusion effect. The gas permeability of a layered assembly can be calculated from the series model as

$P_{//}$ ——— ——— (1)

where $P_{//}$ is the experimentally determined permeability of the multilayered film, $\varphi_{nanolayer}$ is the volume fraction of the PEMA110 nanocomposite layer, and $P_{nanolayer}$ and $P_{LDPElayer}$ are the permeabilities of the PEMA110 nancomposite layers and LDPE layers, respectively. To account for the changes in the permeability of the LDPE layers as they absorbed the PEMA110 polymer through interdiffusion, a series of blends of these two polymers were prepared, and used to generate a trendline to determine $P_{LDPElayer}$ (Figure 52). This plot of permeability with volume fraction of PEMA110 in LDPE is linear, which is behavior typical of miscible polymer blends. Permeabilities of the microlayer components, the PEMA110/LDPE blends, and the bulk nanocomposites are shown in Table 12.

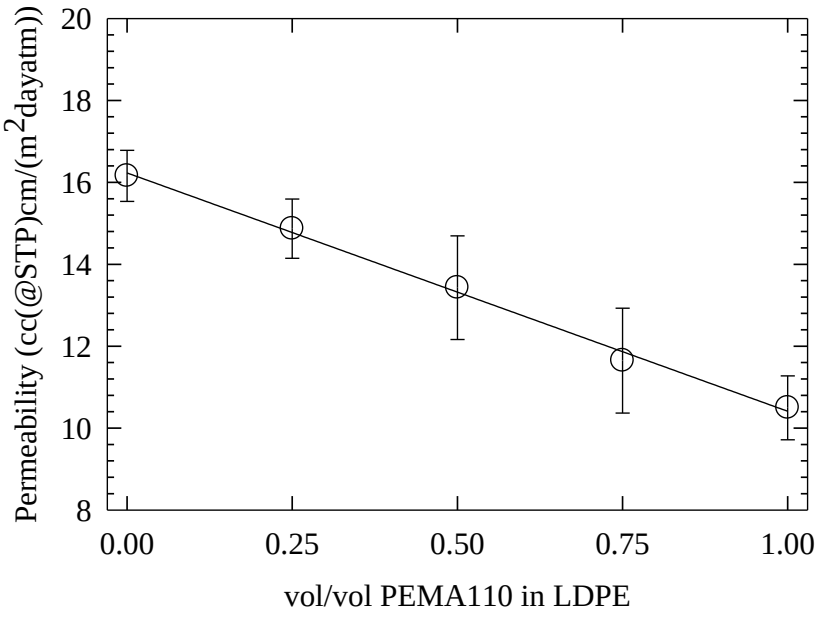

Figure 52. Permeability of blends of PEMA110 with LDPE prepared by twin screw extrusion.

Table 12

Material Designations, Composition, and Oxygen Permeabilities

Material	Composition	Permeability ± std deviation (cc(@STP)cm/(m^{2}dayatm))
Polymer		
LDPE	100% LDPE	16.16 ± 0.62
PEMA110 (LLDPE-g-MA)	100% PEMA110	10.50 ± 0.78
PEMA528 (LLDPE-g-MA)	100% PEMA528	16.59 ± 1.14
Polymer blends		
25/75 PEMA110 in LDPE	25% vol/vol PEMA110 in LDPE	14.87 ± 0.72
50/50 PEMA110 in LDPE	50% vol/vol PEMA110 in LDPE	13.43 ± 1.26
75/25 PEMA110 in LDPE	75% vol/vol PEMA110 in LDPE	11.65 ± 1.28
Nanocomposite (bulk)		
PEMA110 nanocomposite	1.03% vol/vol MMT in PEMA110	5.40 ± 0.19
PEMA528 nanocomposite 1%	1.02% vol/vol MMT in PEMA528	9.67 ± 0.62
PEMA528 nanocomposite 2%	2.08% vol/vol MMT in PEMA528	6.44 ± 0.34
PEMA528 nanocomposite 3%	3.19% vol/vol MMT in PEMA528	5.51 ± 0.40
PEMA528 nanocomposite 4%	4.35% vol/vol MMT in PEMA528	4.98 ± 0.27

Using the experimentally determined permeability values for the multilayered films at varying annealed states, the permeability of the PEMA110 nanocomposite layer,

$P_{nanolayer}$, was calculated by the series model (Table 13). For the pre-annealed film, $P_{nanolayer}$ was found to have a value of 5.50 cc(@STP)cm/(m^2dayatm), which closely corresponded to the measured permeability of the bulk PEMA110 nanocomposite (5.40 cc(@STP)cm/(m^2dayatm)) used to create the multilayered films. In order to compare the observed changes in multilayered film permeability to the equivalent PEMA110/LDPE unfilled polymer multilayered systems ($P_{//NoClay}$), we utilized the series model to calculate changes in permeability for these systems, which accounted for the same degree of layer shrinkage due to interdiffusion of the PEMA110 into the adjacent LDPE layers (Table 13). As discussed previously, the virgin PEMA110 could not be multilayered with the LDPE due to the large melt viscosity mismatch, so modeling this system through the series model was necessary.

Table 13

Series Model Predictions of Layer Permeability in Multilayered Films

Anneal time at 200°C (min)	MMT volume fraction from *CF* (φ_{MMT})	Volume fraction of PEMA110 nanocomposite microlayers ($\varphi_{nanolayer}$)	LDPE microlayer permeability (P_{LDPE})	Experimentally measured multilayered film permeability ($P_{//}$)	Permeability of nanolayers from series model ($P_{nanolayer}$)	Predicted multilayer permeability from series model ($P_{//NoClay}$)
0	0.0103	0.51	16.23	8.13	5.50	12.69
5	0.0180	0.30	14.49	7.57	3.61	13.00
15	0.0217	0.24	14.14	5.96	2.08	13.07
17	0.0253	0.21	14.01	5.60	1.72	13.09
25	0.0426	0.13	13.68	4.89	0.92	13.16

Permeability units are in cc(@STP)cm/(m^2dayatm).

As can be seen in Table 13, $P_{nanolayer}$ decreased with annealing time (@200°C) to a final value of 0.92 cc(@STP)cm/(m^2dayatm) at 25 minutes. Since the nanocomposite

microlayers occupy only 13% of the total film volume, it is clear that in order to contribute to the observed decrease in the barrier of the entire multilayered film ($P_{//}$), the nanocomposite layers must have a reduced permeability. Indeed, when compared to the bulk PEMA528 nanocomposite at similar MMT concentration (4.26% vol/vol MMT in PEMA110 vs. 4.35% vol/vol MMT in PEMA528) we can see that the relative oxygen barrier of the concentrated nanocomposite layers ($P_{nanolayer}/P_{PEMA110} = 0.09$) is three times better than the PEMA528 nanocomposite control ($P/P_{PEMA528} = 0.30$) at nearly identical clay content. It is clear that the differences in clay morphology between the multilayered PEMA110 nanocomposite layers and the PEMA528 control nanocomposites had a profound influence on the gas barrier properties.

Correlation of Clay Morphology with Permeability Using Diffusion Models

In order to better understand the relationship between the observed clay morphologies and the gas barrier data, diffusion models were applied, using the observed clay morphologies. In Table 14, diffusion models were applied to predict the permeability of the nanocomposites utilizing the experimentally determined number average particle aspect ratio, α, and φ_{MMT}. These diffusion models are outlined in Table 15. For the multilayered systems the volume fraction of MMT is based upon the *CF* from the OM image analysis, and the permeability predictions relate only to the PEMA110 nanocomposite layers. Each of these models predicted permeabilities for the nanocomposite systems that were higher than those observed, although the Cussler random array model most closely approached the observed nancomposite permeability values.

Table 14

Permeabilities Calculated from Barrier Models Utilizing Volume Fractions MMT (Φ_{mmt}) and the Observed Average Aspect Ratio (α)

MMT volume fraction (φ_{MMT})	Number average aspect ratio (α)	Experimentally determined permeability (P)	(P) predicted from Nielsen model	(P) predicted from Cussler *regular array* model	(P) predicted from Cussler *random array* model	(P) predicted from Gusev-Lusti model
PEMA 110 nanocomposite Layer						
0.0103	29.9 ± 15.7	5.50	*7.94*	*9.48*	*7.16*	*7.75*
0.0180	36.6 ± 24.8	3.61	*6.21*	*7.14*	*4.97*	*6.23*
0.0217	46.6 ± 28.4	2.08	*5.10*	*5.01*	*3.66*	*5.19*
0.0253	52.9 ± 34.0	1.72	*4.38*	*3.61*	*2.86*	*4.46*
0.0426	54.5 ± 30.0	0.92	*3.03*	*1.52*	*1.55*	*2.94*
PEMA528 Bulk Nanocomposite						
0.0102	28.5 ± 15.7	9.67	*12.73*	*15.14*	*11.53*	*12.40*
0.0208	24.0 ± 13.7	6.44	*10.83*	*12.94*	*9.14*	*10.75*
0.0319	20.6 ± 13.4	5.51	*9.68*	*11.09*	*7.75*	*9.71*
0.0435	13.5 ± 7.3	4.98	*9.98*	*11.64*	*8.18*	*9.97*

Permeability units in cc(@STP)cm/(m^2dayatm).

Table 15

Models for Predicting Barrier properties of Platelet Filled Nanocomposites

Model	Filler Type	Formula*	Reference
Nielsen	Ribbon[a]	$(P_0/P)(1-\varphi) = (1+\alpha\varphi)$	[3]
Cussler (*regular array*)	Ribbon[a]	$(P_0/P) = 1+ (\alpha^2\varphi^2)/(1-\varphi)$	[4]
Cussler (*random array*)	Ribbon[a]	$(P_0/P)(1-\varphi) = (1+2\alpha\varphi/3)^2$	[5]
Gusev and Lusti	Disk[b]	$(P_0/P)(1-\varphi) = \exp[(2\alpha\varphi/3.47)^{0.71}]$	[30]
Cussler (polydisperse flakes) (*discrete distribution*)	Ribbon[a]	$(P_0/P)(1-\varphi) = [1+(2\varphi\Sigma_i n_i R_i^2)/(3a\Sigma_i n_i R_i)]^2$ where n_i = number of flakes of size category i R_i = ½ particle width a = particle thickness	[5]
Cussler (polydisperse flakes) (*continuous distribution*)	Ribbon[a]	$(P_0/P)(1-\varphi) = [1+2\varphi(R^2+\sigma^2)/(3aR)]^2$ where R = number average ½ particle width σ = standard deviation of ½ particle width a = particle thickness	[5]

[a] For ribbons, length is infinite, ½ particle width is R, thickness is a, aspect ratio is $\alpha = R/a$.

[b] For disks, ½ diameter r and thickness t, aspect ratio is $\alpha = r/t$.

[*] φ is volume fraction of filler, P is permeability of composite, P_0 is permeability of pure polymer

From the particle analysis data, it was observed that the particle lengths and aspect ratio distributions had considerable breadth in both systems, which was not accurately taken into account by the use of a numerical average aspect ratio utilizing the models employed in Table 15. Indeed, none of the diffusion models employed in Table 15 addressed the significant particle polydispersity distributions observed in the nanocomposite systems studied. To address the significance of polydispersity in disc

sizes, Fredrickson Bicerano and suggested the addition of a factor for the normalized size distribution function (integrated over all the disk radii) to the diffusion equation [2]. Cussler et al. incorporated this polydispersity concept into their random array diffusion model (Table 15). The polydisperse flakes discrete distribution model addresses the path length increase by a summation of the number of flakes hit times the distance traveled per flake, and the continuous distribution model describes path length in an analogous way utilizing an integral that assumes a Gaussian distribution of flake sizes. Both models are expansions to the Cussler random array model, which describes a system of flakes that are arranged without long range ordering, i.e., not in a well defined lattice. The discrete distribution model utilizes the following terms: ½ individual particle length, R_i, the volume fraction of flakes, φ_{MMT}, and a constant flake thickness, a. The continuous distribution model uses the same constant flake thickness, a, and volume fraction of flakes, φ_{MMT}, with the number average ½ particle length ,R, and the standard deviation of R. While the nanocomposite systems studied herein do not truly possess constant particle thicknesses, they are possessed of a very small range of thicknesses as can be seen in Tables 7 an 11, and we consider this assumption a reasonable simplification. The experimental variables utilized and permeabilities predicted from these models are shown in Table 16. The permeabilities predicted by these models based upon the empirical measurements of the particle dimensions give values that come much closer to those observed experimentally.

Table 16

Permeabilities Derived from Cussler Models for Polydisperse Flake Distributions

MMT volume fraction (φ_{MMT})	Average ½ particle length R (nm)	Standard deviation of R (σ, nm)	Average particle thickness (a)	Experimentally determined permeability P	Sum n_iR_i	Sum $n_iR_i^2$	(P) Cussler polydisperse *discrete random distribution*	(P) Cussler polydisperse *continuous random distribution*
PEMA110 Nanocomposite Layer								
0.0103	35.9	17.0	1.3	5.50	16881	741874	*6.890*	*6.889*
0.0180	46.7	23.5	1.5	3.61	42377	2478589	*4.782*	*4.781*
0.0217	68.2	41.3	1.5	2.08	49452	4608051	*2.883*	*2.882*
0.0253	72.7	46.7	1.5	1.72	60276	6187289	*2.152*	*2.151*
0.0426	86.9	47.3	1.7	0.92	40941	4610157	*1.185*	*1.184*
PEMA528 Bulk Nanocomposite								
0.0102	45.7	29.8	1.7	9.67	31362	2044191	*10.252*	*10.250*
0.0208	33.5	21.8	1.4	6.44	15960	761356	*7.585*	*7.582*
0.0319	37.0	26.8	1.8	5.51	36078	2036314	*5.876*	*5.874*
0.0435	24.3	15.9	1.7	4.98	22046	765060	*6.391*	*6.389*

Permeability Units in cc(@STP)cm/(m^2dayatm).

The relative permeabilities, P/P_0, for the bulk PEMA528 nanocomposites predicted by the diffusion models were plotted with the experimentally observed P/P_0 in Figure 53. The Cussler polydisperse continuous random distribution model was observed to give the closest correlation to the experimentally observed relative permeabilities. In Figure 54 the relative permeabilities (P/P_0) for the multilayered PEMA110 nanocomposite systems predicted by the diffusion models were plotted as a function of annealing time. For this figure, P_0 was taken as the predicted multilayer permeability from the series model for an unfilled multilayered system of PEMA110 and LDPE (Table

13). Again, the Cussler polydisperse continuous random distribution model was observed to give the closest correlation to the experimentally observed relative permeabilities.

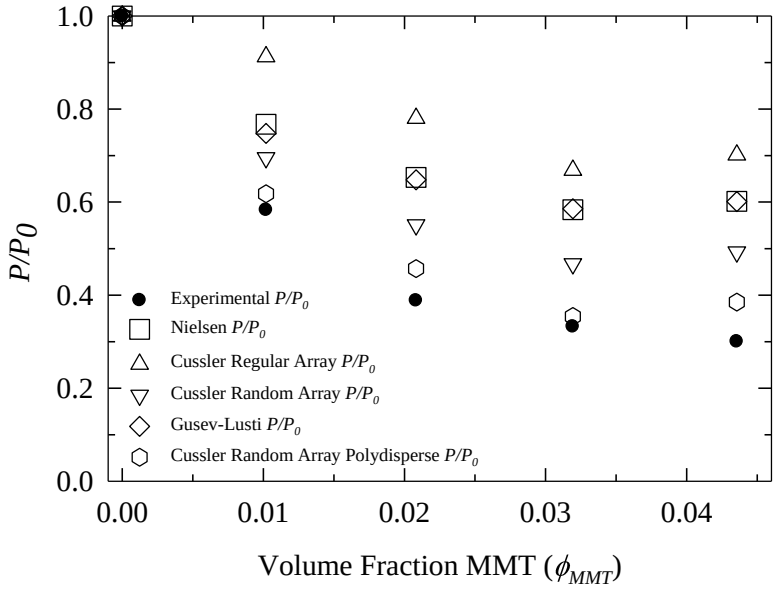

Figure 53. Relative permeabilities (P/P_0) predicted for bulk nanocomposite PEMA528 nanocomposite controls utilizing barrier model predictions.

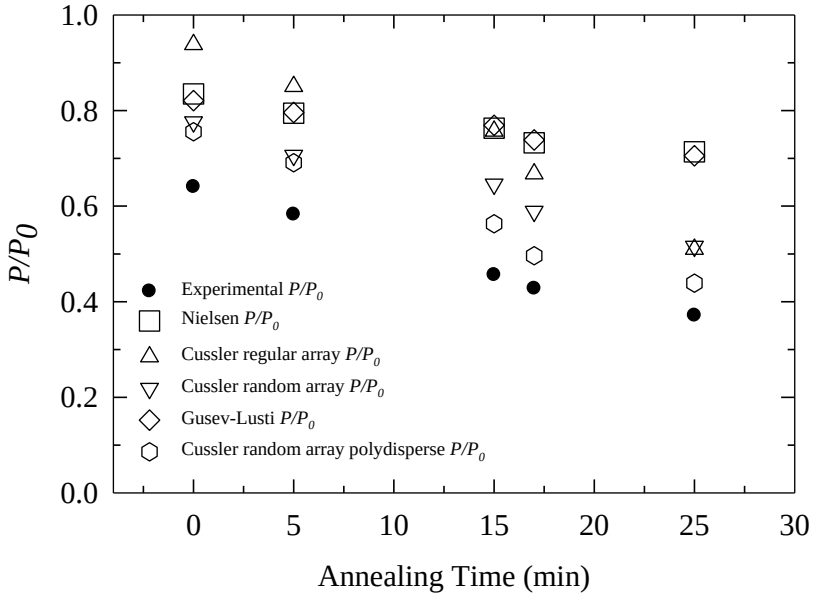

Figure 54. Relative permeabilities (P/P_0) predicted for multilayered films with layer interdiffusion utilizing barrier model predictions.

It should be noted that none of the barrier models employed in this paper give an exact correlation with experimental results. This is not particularly surprising since these models are based upon idealized particle shape assumptions. While the thickness of indivual montmorillonite platelets is an extremely well defined crystallographic dimension, the lateral shape and dimensions are not well defined. Indeed, the shape distributions of MMT clays are far more randomized than any well defined disc or ribbon shape [31,32]. Based upon this reality, the authors own TEM analysis suffers from the assumption that an edgewise view of a clay layer or a skewed aggregate of clay layers is representative of that clay particle in three dimensions. In addition, the analysis and subsequent correlation with the barrier models also assumes that the clay aggregation state is that of discrete sheet-like particles. One need only look at Figure 43 to see that it was not uncommon for clay layers to be seen to cross paths. With only a two dimensional image, we cannot definitively say that these layers are discrete from one another; indeed, they may overlap in the third dimension. This concern becomes more relevant when we look at the larger skewed aggregates that crossed paths. If we assume that the dimensions seen in two dimensions translate to the third, then this is no longer a simple morphology of discrete sheets that can be accurately correlated with these barrier models. As the clay concentrated in the multilayered systems, this crossing effect became more prominent, to where the clay may actually have formed regions of percolated clay structures that extend in many directions, following multiple complicated paths. However, this would have made for an incredibly confusing analyis and prevented comparisions to established barrier models, so our analysis assumed that the

nanocomposites were composed of sheet-like structures with a measurable length and thickness, with a third dimension equal to the observed particle length.

It should also be noted that polymer trapped between MMT layers will have a bulk diffusivity that is infinitesimally small, and as such it will increase the effective volume fraction contribution of the clay particle aggregates [33]. Considering the complicated morphologies observed, especially in the annealed multilayered films, this possibility cannot be discounted, although its effect is not easily quantified in this instance.

A final concern must also be addressed. While great care was taken to measure the dimensions of the clay particles by TEM, the dimensions observed are from a random cut through irregular platelets and only rarely will the maximum dimension be seen [34]. When the clay particles were large relative to the sectioned thickness, this effect became more significant and the observed size distributions contained populations that were smaller than the actual particle diameters. This effect would have lead to an observation of particle lengths that were smaller than truly existed, and thus have caused an underestimation of the barrier properties via the diffusion models.

In summary, a comparison of the microlayered nanocomposite layer to the bulk controls showed that the barrier increases observed with the multulayered films were influenced by the increase in clay particle lengths, which was a direct result of the low shear clay concentration caused by interdiffusion in the multilayered films. In contrast, the bulk nanocomposites generated by twin screw extrusion exhibited a decrease in particle lengths with increasng clay concentration, caused by increases in viscosity with clay content. At the final MMT concentration of 4.3% vol/vol, the nanocomposite

microlayers exhibited relative permeabilities three times better than those of the bulk nanocomposite generated by twin screw extrusion, which can only be attributed to the growth of the skewed clay aggregates that occurred during the melt induced concentration of the nanocomposite layer.

Conclusions

Layer multilplying coextrusion used forced assembly to create films consisting of a layered assembly of alternating layers of LDPE and a PEMA110 (LLDPE-g-MA) nancomposite containing organically modified montmorillonite clay. The MMT concentration within the nanocomposite layers was increased through annealing of the multilayered films. This process took advantage of the mismatch in diffusion coefficients between the microlayers, allowing the PEMA110 polymer to diffuse into the adjacent LDPE layers under negligible shear conditions.

Morphological differences between the multilayered nanocomposite films under various extents of layer shrinkage and a set of nanocomposite control films prepared by twin screw extrusion, showed that the clay morphology behaved differently with increasing clay content. The multilayered system showed an unexpected increase in clay particle length and aspect ratio with annealing time, which was attributed to the growth of skewed aggregates within the nanocomposite layers as they were concentrated by the preferential interdiffusion of the PEMA110 polymer into the adjacent LDPE layers. The MMT morphology was quite different for the bulk PEMA528 nanocomposite prepared by twin screw extrusion, where particle lengths and aspect ratios decreased with increasing MMT content, which was attributed to the high shear processing conditions that reduced the length of the clay particles. The lack of shear during the concentration

of the PEMA110 nanocomposite layers (from interdiffusion) was attributed to the observed increases in clay particle dimensions, which allowed for the growth of skewed aggregates, as the clay layers impinged upon one another during microlayer concentration.

The annealed multilayered nanocomposite films showed decreasing relative permeabilites (P/P_0) with annealing. This was attributed to the decreased oxygen permeability of the nanocomposite microlayers as they were concentrated. Indeed, when one considers that bulk multilayered film concentration was only 0.51% vol/vol MMT, the bulk nanocomposites reached much higher concentrations (at least by a factor of four) to achieve only slightly better oygen barrier. This decrease in multilayer film permeability was caused by the increased oxygen barrier of the annealed nanocomposite microlayer, which changed with layer shrinkage from an initial value of 5.50 cc(@STP)cm/(m^2dayatm) to a final value of 0.92 cc(@STP)cm/(m^2dayatm). This corresponded to a relative permeability, P/P_0,of 0.09 for the concentrated nanocomposite layers, compared to the P/P_0 of 0.30 for the bulk nanocomposite film at similar clay content.

This increase in the nanocomposite microlayer barrier was attributed to the increases in particle lengths and aspect ratios that occurred during microlayer concentration and also from the increased clay partcle size dispersity. For both systems, a diffusion model that accounted for the dispersity in particle size distributions (Cussler polydisperse random) gave the most accurate representation of the oxygen barrier behavior, indicating that particle size distribution of flakes in composite systems may have a significant impact on the final barrier properties.

While the increases in barrier properties observed by this methodology are in themselves novel and interesting, it is clear from an understanding of the mathematical models provided that increasing the initial aspect ratios, and the initial concetration of filler in these multilayered systems will lead to even more impressive barrier results. Indeed, with higher aspect ratio fillers, these results may prove phenomenal, especially if the same trends of particle length growth are observed with miscible multilayered systems that preferentially interdiffuse. To this end, work is currently in progress on systems containing high aspect ratio fillers that have a less significant impact on processing viscosity, allowing higher filler loadings and aspect ratios.

References

[1] Paul DR, Robeson LM. Polymer nanotechnology: nanocomposites. Polymer 2008; 49: 3187-3204.

[2] Fredrickson GH, Bicerano J. Barrier properties of oriented disk composites. J Chem Phys 1999; 110(4): 2181-2188.

[3] Nielsen LE. Models for the permeability of filled polymer systems. Macromol Sci (Chem) 1967; A1 :929–42.

[4] Cussler EL, Hughes SE, Ward WJ III, Aris R. Barrier membranes. J Membrane Sci 1988; 38: 161-174.

[5] Lape NK, Nuxoll EE, Cussler EL. Polydisperse flakes in barrier films. J Membr Sci 2004; 236: 29–37.

[6] Ray SS, Okamoto M. Polymer/layered silicate nanocomposites: a review from preparation to processing. Prog Polym Sci 2003; 28: 1539-1641.

[7] Lee H-S, Fasulo PD, Rodgers WR, Paul DR. TPO based nanocomposites. Part 1. Morphology and mechanical properties. Polymer 2005; 46: 11673-11689.

[8] Fornes TD, Yoon PJ, Keskkula H, Paul DR. Nylon 6 nanocomposites: the effect of matrix molecular weight. Polymer 2001; 42(25): 9929-9940.

[9] Mueller C, Nazarenko S, Ebeling T, Schuman TL, Hiltner A, Baer E. Novel structures by microlayer eoextrusion-talc-filled PP, PC/SAN, and HDPE/LLDPE, Poly Eng Sci 1997; 37: 355-362.

[10] Nazarenko S, Hiltner A, Baer E. Microlayer Structures with Anisotropic Conductivity. Journal of Material Science 1999; 34: 1461 – 1470.

[11] Keskkula H, Paul DR. Diffusion of miscible polymers in multilayer films. Appl Polym Sci 1987; 34: 1861-1877.

[12] Pollock G, Nazarenko S,Hiltner A, Baer E. Interdiffusion in microlayered polymer composites of polycarbonate and a copolyester, App Polym Sci 1994; 52: 163-176.

[13] Schuman T, Stepanov EV, Nazarenko S, Capaccio G, Hiltner A, Baer E. Interdiffusion of linear and branched polyethylene in microlayers studied via melting behavior. Macromolecules 1998; 31: 4551-4561.

[14] Schuman T, Nazarenko S, Stepanov EV, Magonov S,Hiltner A, Baer E. Solid state structure and melting behavior of interdiffused polyethylenes in microlayers, Polymer 1999; 40: 7373–7385.

[15] Kramer E J, Green P, Palmstrøm CJ. Interdiffusion and marker movements in concentrated polymer-polymer diffusion couples. Polymer 1984; 25: 473-480.

[16] Green PF, Palmstrøm CJ, Mayer JW, Kramer EJ. Marker displacement measurements of polymer-polymer interdiffusion. Macromolecules 1985; 18: 501-507.

[17] Nazarenko S, Dennison M, Schuman T, Stepanov EV, Hiltner A, Baer E. Creating layers of concentrated inorganic particles by interdiffusion of polyethylenes in microlayers. J Appl Polym Sci 1999; 73: 2877-2885.

[18] Zhang M, Uttandaraman S. Thermal, rheological, and mechanical behaviors of LLDPE/PEMA/clay nanocomposites: effect of interaction between polymer, compatibilizer, and nanofiller. Macromol Mater Eng 2006; 291: 697-706.

[19] Hotta S, Paul DR. Nanocomposites formed from linear low density polyethylene and organoclays. Polymer 2004; 45(22): 7639–7654.

[20] Cui L, Ma X, Paul DR. Morphology and properties of nanocomposites formed from ethylene-vinyl acetate copolymers and organoclays. Polymer 2007; 48(21): 6325-6339.

[21] Mueller CD, Nazarenko S, Ebeling T, Schuman TL, Hiltner A, Baer E. Microlayer coextrusion: processing and applications. Polym Eng Sci 1997;37: 355-362.

[22] Mueller CD, Kerns J, Ebeling T, Nazarenko S, Hiltner A, Baer E. Polymer process engineering 1997; Coates PD, Editor; The Institute of Materials: London, 1997: 137-157

[23] Sekelik DJ, Stepanov EV, Nazarenko S, Schiraldi D, Hiltner A, Baer E. Oxygen barrier properties of crystallized and talc-filled poly(ethylene terephthalate). Polym Sci Part B Polym Phys 1999; 37: 847-857.

[24] Decker JJ, Chvalun SN, Nazarenko S. Intercalation behavior of hydroxylated dendritic polyesters in polymer clay nanocomposites prepared from aqueous solution. Polymer 2011; 52: 3943-3955.

[25] Lee H-S, Fasulo PD, Rodgers WR, Paul DR. TPO based nanocomposites. Part 2. Thermal expansion behavior. Polymer 2006; 47(10): 3528-3539.

[26] Nam PH, Maiti P, Okamoto M, Kotaka T, Hasegawa N, Usuki A. A hierarchical structure and properties of intercalated polypropylene/clay nanocomposites. Polymer 2001; 42(23): 9633-9640.

[27] Galgali G, Ramesh C, Lele A. A rheological study on the kinetics of hybrid formation in polypropylene nanocomposites. Macromolecules 2001; 34(4): 852-858.

[28] Fornes TD, Paul DR. Modeling properties of nylon 6/clay nanocomposites using composite theories. Polymer 2003; 44: 4993-5013.

[29] Van Damme H, Levitz P, Fripiat JJ, Alcover JF, Gatineau L, Bergaya F. Physics of finely divided matter. In: Proceeding of the winter schools, Les Houches, France, Ed. N. Boccara and M. Daoud, Springer Verlag, 1985, 24-30.

[30] Gusev AA, Lusti HR. Rational design of nanocomposites for barrier applications. Adv Mater 2001; 13(21): 1641-1643.

[31] Cao T, Fasulo PD, Rodgers WR. Investigation of the shear stress effect on montmorillonite platelet aspect ratio by atomic force microscopy. App Clay Sci 2010; 49: 21-28.

[32] Ploehn HJ, Liu C. Quantitative analysis of montmorillonite platelet size by atomic force microscopy. Ind Eng Chem Res 2006; 45: 7025-7034.

[33] Nazarenko S, Meneghetti P, Julmon P, Olson BG, Qutubuddin S. Gas barrier of polystyrene montmorillonite clay nanocomposites: effect of mineral layer aggregation. J Polymer Sci Part B Polym Phys 2007; 45: 1733-1753.

[34] Corté L, Leibler L. Analysis of polymer blend morphologies from transmission electron micrographs. Polymer 2005; 46: 6360-6368.